Graduate School of the
SOUTHAMPTON OCEANOGRAPHY CENTRE

This PhD dissertation by

Kevin Grant

has been produced under the supervision of the following persons

Supervisor/s

Dr. S. Roberts

Chair of Advisory Panel

Prof. J. Murray

Member/s of Advisory Panel

Mr. T. Clayton

The Application of Micro-Infrared Spectroscopy and Cathodoluminescence to the study of Natural Quartz

Kevin Grant

Doctor of Philosophy

SCHOOL OF OCEAN AND EARTH SCIENCE

FACULTY OF SCIENCE

UNIVERSITY OF SOUTHAMPTON

DECLARATION

This thesis describes my own original work except where an acknowledgement is made in the text. To the best of my knowledge the work presented here is not substantially the same as any work that has been, or is being submitted to any other university for any other degree or diploma

Kevin Grant - (May 2002)

UNIVERSITY OF SOUTHAMPTON

ABSTRACT

FACULTY OF SCIENCE

SCHOOL OF OCEAN AND EARTH SCIENCE

Doctor of Philosophy

The Application of Micro-Infrared Spectroscopy and Cathodoluminescence to the study of Natural Quartz

By Kevin Grant

Determination of the hydrogen species in hydrogen in vein quartz using infrared spectroscopy shows that samples containing a significant fluid inclusion population also yield a 'normal' hydrogen isotope signature (-39‰). Samples generating an anomalous δD signature (-103‰) contain a significant quantity of structurally incorporated defect hydrogen species. Additional experiments different hydrogen reservoirs are liberated from quartz at temperatures that correlate with those described previously as generating anomalous hydrogen isotope signatures during stepped heating isotopic experiments. The findings suggest that hydrogen isotope signatures decoupled from that suggested by accompanying oxygen isotopes may be attributable to a significant defect hydrogen reservoir in the sample.

Using mid-infrared spectroscopy, the frequencies of the fundamental molecular vibrations obtained using standard and field-based sample preparation techniques are the same. Bands generated using infrared absorbance and reflectance spectroscopic techniques are also in good agreement. Micro-infrared spectroscopy was used to characterise the products of hydrothermally altered plagioclase phenocrysts from the Chelopech Au deposit, Bulgaria. Samples from inside and outside the main silicified zone are dominated by kaolinite and beidellite respectively. Mineral characterisation was confirmed using XRD analysis.

Cathodoluminescence images of quartz phenocrysts from a porphyry copper related intrusion elucidate numerous growth zones. Dendritic morphologies, indicative of periods of rapid growth, are found in the inner regions of individual zones. These regions also display a bright luminescence response. Outer regions of an individual zone may display morphologies indicative of euhedral growth and are of lower luminescence response. The observed growth patterns record numerous periods of cyclic growth, which are interpreted to be associated with periodic phases of magmatic volatile exsolution.

Concentrations of H-OH groups, measured using micro-infrared spectroscopy during a traverse of a magmatic quartz crystal, show significant spatial variability. This is attributed to irregular incorporation of these species during crystal growth. Regions recording high H-OH contents also correlate with those displaying bright luminescence response and quartz habits indicative of rapid growth. The results of this study suggest that SEM-CL images may provide a rapid technique for interpreting the relative rates of quartz growth in a crystal.

Apatite and biotite crystals are found as inclusions in quartz phenocrysts. Calculations using the elemental composition of these phases enables log fugacity ratios $\log(f_{H2O})/(f_{HCl})$, $\log(f_{H2O})/(f_{HF})$, and $\log(f_{HF})/f_{HCl})$ to be calculated for the precipitating medium. A comparison between log fugacity ratios of the studied intrusion, with those from other porphyry copper settings, shows halogen bearing minerals in many porphyry systems have crystallised under a similar fugacity regime.

Contents

List of Figures

CHAPTER 5

CHAPTER 6

CHAPTER 7

CHAPTER 8

List of Tables

CHAPTER 4

CHAPTER 8

Acknowledgements

I would like to express my gratitude to Dr. S. Roberts for his invaluable encouragement, assistance and constructive criticism during the completion of this thesis.

The samples studied in Chapter 3 were generously donated by Dr. S. Gleeson, who is also thanked for comments and discussion on the results.. Samples described in Chapters 6, 7 and 8 were kindly donated by Dr. R. Armstrong, who was also a source of great inspiration during the 'early years' in Southampton.

Several Chapters benefited greatly from advice and discussion from Drs. M. Dove, I. Farnan, S. Kohn R. Brooker, S. Mackwell, J. Ingrin and Prof. O. Jaoul. Special thanks are also extended to S. Salvi for the use of his computer.

For help and guidance during my time in Southampton thanks are forwarded to Bob and John, Ellis, Wayne and whoever else I've forgotten an the SOC. Thanks also to Phil, Steve and the rest of the gang. I would also like to express my gratitude to Adam, Ciarran (and of course who could forget Charlie) and the rest of the posse for some memorable nights out (and night in.....)

Last, but not least, I would like to thank my wonderful girlfriend, Nicola for putting up with me and my parents for everything....

Chapter 1

INTRODUCTION

1 Introduction

1.1 Overview

Hydrogen is one of the most pervasive elements in the crust and upper mantle of the Earth. It is a mobile, reactive component, which can cause major changes in the chemical, physical, rheological, and electronic properties of the host phase. From the development of hydrothermal ore deposits through to the crystallisation of specific crystal morphologies, hydrogen-related fluids play a significant role in many geological processes. In the lithosphere they serve as an essential solvent and transport medium for many of the elements, modify the physical properties of rocks, and lubricate tectonic processes. This thesis presents several chapters highlighting the significance of fluids in a number of diverse geological environments. This Chapter provides a short abstract detailing the work carried out, and the results obtained, for each chapter. Chapter 2 provides a short note on the technique of infrared spectroscopy. The geological background of the Morenci Porphyry Copper deposit, Arizona is presented on Chapter 5. Each of the remaining chapters represent a discrete research project which focuses on individual aspects of the effect of fluids in several geological processes.

1.2 Thesis Papers

Chapter 3

The determination of hydrogen isotope ratios is a fundamental geochemical analytical procedure that has contributed significantly to our understanding of the nature of numerous processes involved in the earth sciences. In particular, coupled hydrogen and oxygen isotope ratios allow the isotopic composition and origin of the volatile phase involved in most igneous, metamorphic and hydrothermal processes to be characterised (Sheppard, 1986). Indirect measurement of the isotopic composition of hydrothermal fluids is obtained by calculating the isotopic composition of the fluid in equilibrium with the isotopically and chemically analysed mineral. To accomplish

this, fundamental constraints upon the variation of the mineral-H_2O (or brine) fractionation factor as a function of temperature must be made (O'Neil, 1986).

A recent investigation into the isotopic signature of fluid inclusions incorporated into hydrothermal vein quartz revealed significant discrepancies between the nature of the fluid elucidated using oxygen and hydrogen isotopes (Gleeson *et al.,* 1999). Chapter 3 presents the results of an infrared spectroscopic investigation into the nature of the hydrogen species in the quartz samples which yield these anomalous isotopic signatures. In this study a correlation is noted between samples containing a significant fluid inclusion population with those yielding a hydrogen isotope signature of a fluid is in accordance with that inferred by the $\delta^{18}O$ value. In samples generating an anomalous δD signature, structurally incorporated defect hydrogen contributes a significant component.

It is well known that during oxygen incorporation into the quartz crystal structure, significant isotopic fractionation takes place (O'Neil, 1986). However, despite the fact that it is also well known that hydrogen may be easily incorporated into quartz, the likelihood of hydrogen fractionation into defect sites in quartz has not been addressed by any previous investigations. The findings described in Chapter 3 imply that hydrogen incorporation into defect sites in the quartz structure may indeed be subject to significant fractionation. Accordingly, the overall hydrogen budget of the sample, recorded by bulk extraction techniques employed during the sample analysis process, may record the isotopic composition of both the original precipitating fluid and any fractionated hydrogen. This may generate results that lead to misunderstanding of the geological processes involved. Additional experiments detail the liberation of different hydrogen reservoirs with increased temperature. These experiments show that discrete hydrous species are released at temperatures which correlate with those described as generating anomalous hydrogen isotope signatures obtained during stepped heating isotopic experiments (Ishayama *et al.,* 1999). A version of this chapter has been submitted as a manuscript for consideration of publication to *American Mineralogist.* The submitted manuscript, co-authored by S. Gleeson (Leeds) and S. Roberts (Southampton), was written by K. Grant.

Chapter 4

In the hydrothermal environment, mineral assemblages indicate the physical and chemical conditions experienced by the system and their rapid and correct identification is important to understanding hydrothermal ore deposits. Field portable short-wave infrared spectrometers help identify fine-grained minerals and define compositional variations between phases that may be missed by conventional mapping (Thompson *et al.,* 1999). Unfortunately, the analytical aperture of such instruments is commonly 10cm in diameter, and, accordingly may miss fine scale mineral zonation patterns.

Mid-infrared spectroscopy has frequently been applied to the study and identification of clay minerals (Farmer, 1974a; Marel and Beutelspacher, 1976; Russell and Fraser, 1994), and the recent advent of the infrared microscope has added the possibility of increased resolution. Chapter 3 describes the results of several studies detailing the suitability of mid-infrared spectroscopy in determining clay mineral composition. Analysis of an XRD kaolinite standard sample, shows that, although band intensities obtained on samples crudely prepared, do not correlate with those obtained using standard sample preparation techniques, vibrational frequencies, which are critical in identifying the minerals species present, obtained using the two techniques are the same. Bands generated using both infrared absorbance and reflectance spectroscopy are also in good agreement.

Laboratory-based infrared absorbance spectroscopy was then used to characterise the composition of hydrothermally altered feldspar phenocrysts. Samples were obtained during a traverse of the Chelopech Au deposit, Bulgaria. Spectral analysis indicates the locations of alteration and mineralisation zones at Chelopech, as confirmed by XRD analysis. The results suggest that samples primarily composed of minerals containing fundamental bands in discrete parts of the infrared spectrum may be readily identified using infrared spectroscopy. Problems may arise where a sample is composed of several minerals generating absorptions in the same spectral region. Attempting to differentiate between minerals which, due to similar structural and chemical characteristics, show characteristic absorptions in the same regions of the infrared spectrum may require more complex, laboratory-based analysis. A major

limitation of infrared spectroscopy is that interstratified minerals may not be distinguished from a mineral mixture.

Chapter 5

Chapters 6, 7 and 8 detail the results of analyses performed on quartz phenocrysts, and phases found within them, from an intrusion associated with the Morenci Porphyry copper deposit, Arizona. The phenocrysts were donated by Robin Armstrong (Natural History museum, London). Chapter 5 provides a geological background to the region and petrography of the samples analysed in the chapters which follow.

Chapter 6

Cathodoluminescence, the emission of light following electron radiation, greatly facilitates the study of any internal fabric present in quartz. The technique has been previously applied with great success to the identification of growth zones within otherwise homogeneous quartz crystals (Demars *et al.*, 1996; Müller *et al.,* 2000; Pennison-Dorland, 2001; Watt *et al.,* 1997), permitting a detailed crystallisation history to be established. Chapter 6 describes scanning SEM-cathodoluminescence images of quartz phenocrysts from a granodiorite intrusion associated with the Morenci Porphyry Copper Deposit, Arizona. Images collected in the study elucidate a wealth of textural information, which can be directly related to the growth of the crystal. The Chapter describes both oscillatory and concentric zoning, relict cores, truncated growth zones, embayments, wavy growth zones, dendrites and euhedral overgrowths. Comparison of the observed textures with those previously described in other minerals, coupled with knowledge of crystallisation kinetics, permits a crystallisation history to be established. Individual oscillatory growth zones record a crystallisation sequence from a brightly luminescent interior, gradually decreasing in intensity towards a poorly luminescent exterior. Bright response is prevalent in regions of dendritic morphologies, attributable to rapid crystallisation under high ΔT conditions. A cathodoluminescence response of reduced intensity is indicative of progressively euhedral forms, which crystallise at lower ΔT conditions. The brightness of luminescence response also correlates with quartz morphology and, accordingly, degree of undercooling (ΔT) of the system. Growth patterns suggest that quartz zonation records numerous periods of cyclic growth, perhaps associated with

periodic phases of magmatic volatile exsolution. The chapter was written by K. Grant and reviewed and edited by S. Roberts (Southampton) whose comments contributed to the final version of the Chapter.

Chapter 7

Despite the powerful nature of cathodoluminescence in determining internal heterogeneities in quartz, the cause of its variable luminescence remains poorly understood (Ramseyer *et al.*, 1988; Ramseyer and Mullis, 1990; Stevens Kalkeff *et al.*, 1997). Previous studies undertaken to determine the cause of variable luminescence in quartz have suggested that aluminium may be responsible, yet the results have proved inconclusive (Graupner *et al.*, 2000; Guzzo *et al.*, 1997; Halliburton *et al.*, 1981; Itoh *et al.*, 1990; Müller *et al.*, 2000; Perny *et al., 1992*; Ramseyer *et al.*, 1988; Ramseyer and Mullis, 1990; Stevens Kalkeff and Phillips, 1995; Stevens Kalkeff *et al.*, 1997; Watt *et al.*, 1997). In this study, determination of trace element contents my electron microprobe, which records the absolute concentration of aluminium species in the crystal, show no correlation with cathodoluminescence response. Conventional infrared studies have shown that many of the impurities in quartz are hydrogen-bearing species that form point defects in the crystal lattice (Aines and Rossman, 1984; Kats, 1962; Kronenberg, 1994). Individual impurity cations bond to the oxygen atom of the hydroxyl group with variable strength, and the OH stretching vibration absorbs energy at wavelengths characteristic of that species. Chapter 7 uses high resolution, micro infrared spectroscopy to investigate the concentration of Al-OH, Li-dependent OH and H-OH species in quartz. The data show a relationship between the intensity of cathodoluminescence response and concentration H-OH species in quartz. Regions of bright luminescence response correlate with high levels of H-OH species. It the light of this study it is suggested that further investigation into the causes of cathodoluminescence response in quartz need be correlated with the concentration of specific defect sites. Helpful comments on the work included in this chapter by S. Roberts (Southampton), M. Dove (Cambridge), I. Farnan (Cambridge) and S. Kohn (Bristol) are gratefully acknowledged during preparation of this chapter, which was written entirely by K. Grant.

Chapter 8

Volatile constituents (H_2O, CO_2, S, Cl, F) and metal chloride species are important components of magmatic and hydrothermal ore forming processes. Apatite may crystallise with variable halogen ratios, and is recognised as potential indicators of the relative activities of HF and HCl in hydrothermal fluids and in Cu- and Mo- porphyry systems (Korzhinskii, 1981; Loferski and Ayuso, 1995; Munoz and Swenson, 1981; Selby and Nesbitt, 2000; Yardley, 1984). They may also provide a temporal record of sulphur evolution in magmas associated with porphyry systems (Streck and Dilles, 1998).

Chapter 8 documents the chemical composition of quartz-included apatite from the Younger Granodiorite Porphyry, an intrusion associated with the Morenci Porphyry Copper deposit, Arizona. Microprobe analyses show apatite halogen contents to be significantly enriched compared to apatites from other porphyry copper settings. Apatite halogen data were also used to calculate the fugacity ratios $\log\{(f_{H2O})/(f_{HF})\}$, $\{(f_{H2O})/(_{HCl})\}$, and $\{(f_{HCl})/(f_{HF})\}$ ratios of the precipitating medium (Korzhinskii, 1981).

Biotite data from the same sample (Armstrong, Unpub. PhD Thesis, University of Southampton, 1999) were also used to provide an alternative method of calculating $\log\{(f_{H2O})/(f_{HF})\}$, $\{(f_{H2O})/(_{HCl})\}$, and $\{(f_{HCl})/(f_{HF})\}$ ratios. Fugacity ratios obtained using apatite and biotite data are in good agreement with each other. In accordance with previous authors the $\log\{(f_{H2O})/(f_{HF})\}$ and $\log\{(f_{H2O})/(f_{HCl})\}$ ratios determined for the precipitating medium at Morenci are similar to those from other porphyry copper deposits, while the $\log\{(f_{HCl})/(f_{HF})\}$ ratio varies significantly (Selby and Nesbitt, 2000). The significant variation in $\log\{(f_{HCl})/(f_{HF})\}$ ratio recorded here further strengthens the hypothesis that these values may be related to the source of the magma and/or magmatic processes associated with the melt on its ascent through the crust prior to the exsolution of the magmatic fluids responsible for porphyry minerallisation (Selby and Nesbitt, 2000).

Chapter 2

AN OVERVIEW OF INFRARED SPECTRSCOPY

2 Infrared Spectroscopy

2.1 INTRODUCTION

Although traditional methods of diffraction and elemental analysis remain of considerable importance to workers in the earth sciences, numerous problems posed in mineralogy and petrology remain unresolved using such techniques. In addition the field of interest investigated by modern workers has broadened significantly to include crystalline and amorphous phases, glasses, melts and fluids along with the numerous processes involved at the interfaces between each of the above (Calas and Hawthorn, 1988). It is here in these regions that the numerous types of spectroscopy have been employed where there have emerged as important tools in characterising both the static and dynamic properties of many geologic materials.

		Molecular rotations	Molecular vibrations	Change in valency electrons	Core electron transitions	Nuclear Transitions	
n.m.r	e.s.r.	Microwave	Infrared	visible and ultra-violet	X-ray	γ-ray	
	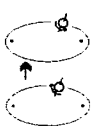	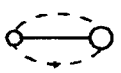	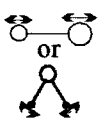			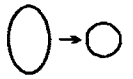	
wavenumber	1	100	10^4	10^6	10^8		cm^{-1}
wavelength	1cm	1mm	10μm	10nm	100pm		
frequency	$3x10^{10}$	$3x10^{12}$	$3x10^{14}$	$3x10^{16}$	$3x10^{18}$		Hz
energy	10	10^3	10^5	10^7	10^9		joules/mol

FIGURE 2.1. Regions of the electromagnetic spectrum. Raman spectroscopy takes place in the microwave region of the spectrum where rotational movements between molecules induce the absorption of radiation. Molecular vibrations induce the absorptions detected by infrared spectroscopy, whereas in visible, ultraviolet, x-ray and g-ray spectroscopies, changes in the electron distribution or configuration excite the molecules. Nuclear Magnetic Resonance (n.m.r.) and Electron Spin Resonance (e.s.r.) are not descriptions of wavelengths but instead measure the reversal of the spin of a nucleus or electron.

2.2 THE ELECTROMAGNETIC SPECTRUM

The electromagnetic spectrum represents the ordered arrangement of radiation energy according to wavelength, frequency or proton energy. Because no single source or detection mechanism is effective over the entire electromagnetic spectrum and because molecules behave differently following interaction with energy of different energies, the electromagnetic spectrum has been subdivided according to the various means of generating, isolating and detecting the radiation involved (Fig. 2.1).

2.2.1 The absorption of radiation

During an infrared experiment, radiation may be reflected off the sample (reflection spectroscopy), or it may pass through the sample, where some of the radiation may be absorbed by the sample and some of it transmitted (Fig. 2.2).

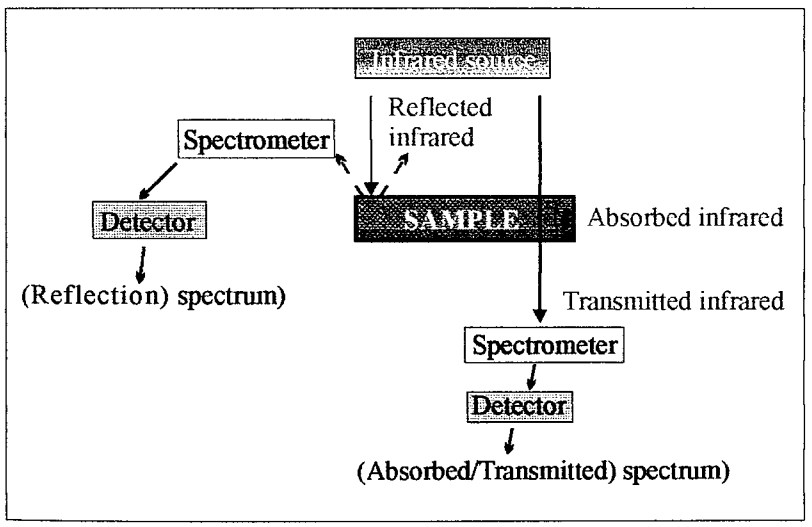

FIGURE 2.2. Schematic representation of the three possible methods of measuring the interaction of infrared light with a sample. Infrared light is passed onto the sample where it may be reflected, absorbed or transmitted through the sample where certain bonds, if they are infrared active, absorb radiation.

2.2.2 The infrared spectrum

Infrared spectroscopy involves the use of radiation to probe the vibrational behaviour of molecular systems. The infrared spectrum obtained during an experiment will show certain bands (characteristic vibrations), typical of particular groups of atoms, which are defined by

2.2 THE ELECTROMAGNETIC SPECTRUM

The electromagnetic spectrum represents the ordered arrangement of radiation energy according to wavelength, frequency or proton energy. Because no single source or detection mechanism is effective over the entire electromagnetic spectrum and because molecules behave differently following interaction with energy of different energies, the electromagnetic spectrum has been subdivided according to the various means of generating, isolating and detecting the radiation involved (Fig. 2.1).

2.2.1 The absorption of radiation

During an infrared experiment, radiation may be reflected off the sample (reflection spectroscopy), or it may pass through the sample, where some of the radiation may be absorbed by the sample and some of it transmitted (Fig. 2.2).

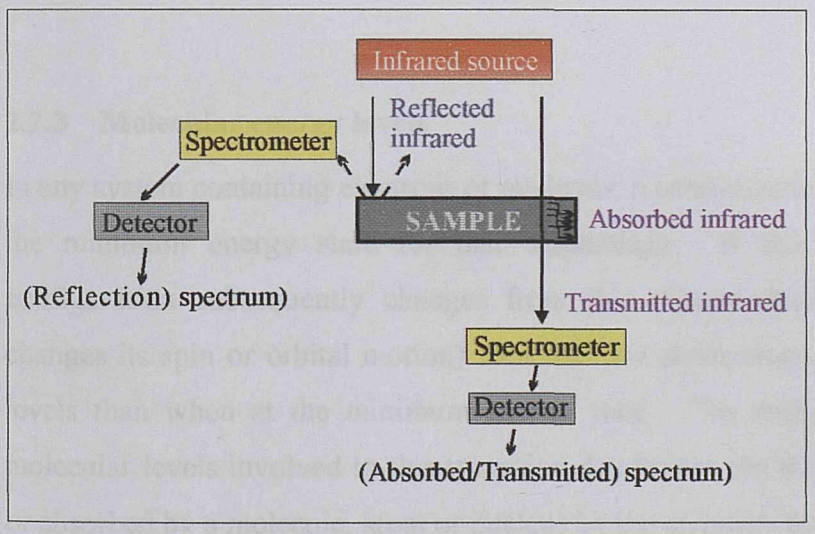

FIGURE 2.2. Schematic representation of the three possible methods of measuring the interaction of infrared light with a sample. Infrared light is passed onto the sample where it may be reflected, absorbed or transmitted through the sample where certain bonds, if they are infrared active, absorb radiation.

2.2.2 The infrared spectrum

Infrared spectroscopy involves the use of radiation to probe the vibrational behaviour of molecular systems. The infrared spectrum obtained during an experiment will show certain bands (characteristic vibrations), typical of particular groups of atoms, which are defined by

definite ranges, frequencies and intensities. Since chemical functional groups are known to absorb radiation at specific frequencies, substances may be readily identified using the resulting vibrational spectrum. The spectral range frequently used in an infrared experiment lies between 4000 and 400 cm^{-1}, and because it contains the fundamental Si-O-Si vibrational modes, proves a useful tool in identifying mineral species, determining mineral chemistry and resolving crystal structure.

Following spectrometer calibration, the intensity of an absorbing species may be used to accurately calculate the concentration of the absorbing species. The intensity of an absorption band is proportional to the concentration of the vibrating component present in the sample via an adaptation of the Beers Law calibration (Aines and Rossman, 1984):

$$A = \varepsilon \cdot \rho \cdot c$$

Where, ε represents the molar absorbtivity of the species being analysed (a constant for each system of interest), ρ is the thickness of the sample, and c is the concentration of the absorbing species.

2.2.3 Molecular energy levels

In any system containing electrons or nucleons, a certain molecular configuration will possess the minimum energy state for that assemblage. If the molecular, atomic or nuclear configuration subsequently changes from this ground state (e.g. an electron or neutron changes its spin or orbital motion) then the new arrangement will experience higher energy levels than when at the minimum energy state. The energy difference between the two molecular levels involved in this transition determines the frequency of the radiation emitted or absorbed by a molecule, atom or nucleus by the quantum condition

$$\nu = E/h$$

Where ν = the frequency of the vibration (Hertz), E = the energy difference and h = Planck constant. Consequently, experimental methods involved to measure the difference between these levels consist, fundamentally, of the measure of frequency. However, for each species, different configurations of the electrons or nucleons result in numerous different excited

states. Spectral lines arising from these transitions, between each of those states, may lie in quite different parts of the electromagnetic spectrum. Due to variations in the specific energy value of each of the individual energy levels, every spectral line has a finite width. Thermal vibrations, collisions with other molecules, or interactions with the electromagnetic or electric fields of other surrounding atoms or nuclei may cause this.

Individual energy levels are not variable or continuous but form discrete energy levels. For a simple harmonic oscillating molecule only two transitions between two adjacent energy levels are permitted. The energy levels generated may be expressed by:

$$E = (u + 0.5)hv$$

Where u = vibrational quantum number (0, 1, 2, 3...). When $u = 0$, the oscillator is at that point of minimum energy which is termed the zero point energy an when $u = 1$ the resulting vibrational band appears at a frequency which represents the fundamental vibrations for that system. The frequencies of the absorption bands v_s are proportional to the energy difference between the vibrational ground state and excited states.

2.2.4 Describing molecular vibrations

It requires three coordinates to describe the position of each atom in space, thus each atom has three degrees of freedom. Accordingly, if a non-linear molecule, e.g. H_2O, has n atoms, there are $3n$ degrees of freedom. Of these, three involve movement of all of the atoms to move simultaneously in the same direction, i.e. translations of the entire system, while another three correspond to molecular rotations. The remaining $3n$-6 degrees, motions which describe changes of the inter-atomic distances, represent the vibrational normal modes fro the system. These vibrations are called the fundamental or normal vibrations of the molecule (Fig. 2.3).

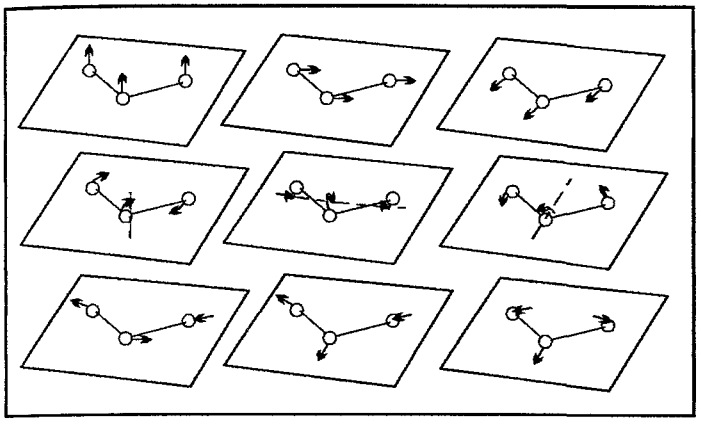

FIGURE 2.3. The motional degrees of freedom of the water molecule, T_i are translations. R_i are rotations of the whole molecule, $i = x, y, z$. ν_s is the symmetric and ν_a the antisymmetric stretching vibrations and δ the deformation (bending) vibration.

However, not every normal vibration is recorded during an infrared experiment. For a molecule to absorb radiation in the infrared there must be a change in the diapole moment (polarity) of the molecule during the absorption process. Accordingly, if we use the water molecule as an example, the only infrared active vibrations are ν_s, the symmetric stretching vibrations, ν_a, the antisymmetric stretching vibrations, and, δ the deformation (bending) vibrations (Fig. 2.4).

Because a molecule must have a permanent dipole (polar covalent bond in which a pair of electrons are shared unequally) to absorb IR radiation, the vibrations of diatomic molecules (e.g. N_2, H_2 etc...) are infrared-inactive.

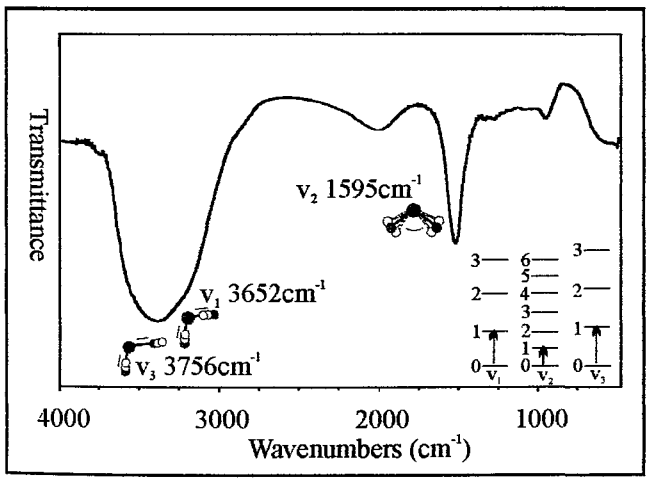

FIGURE 2.4. Infrared spectrum showing the infrared active fundamental vibrations of liquid water.

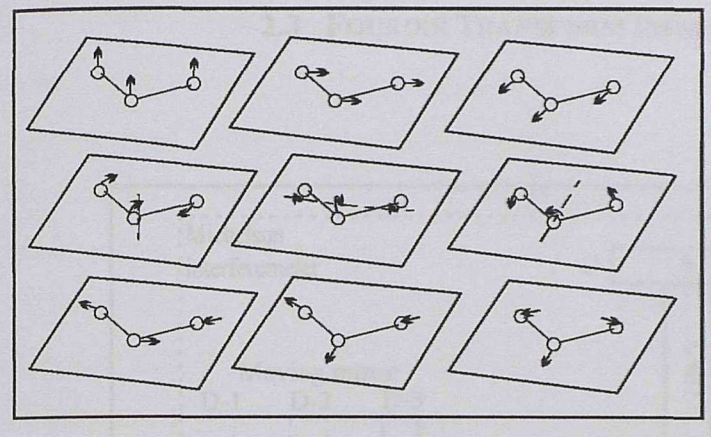

FIGURE 2.3. The motional degrees of freedom of the water molecule, T_i are translations. R_i are rotations of the whole molecule, $i = x, y, z$. ν_s is the symmetric and ν_a the antisymmetric stretching vibrations and δ the deformation (bending) vibration.

However, not every normal vibration is recorded during an infrared experiment. For a molecule to absorb radiation in the infrared there must be a change in the diapole moment (polarity) of the molecule during the absorption process. Accordingly, if we use the water molecule as an example, the only infrared active vibrations are ν_s, the symmetric stretching vibrations, ν_a, the antisymmetric stretching vibrations, and, δ the deformation (bending) vibrations (Fig. 2.4).

Because a molecule must have a permanent dipole (polar covalent bond in which a pair of electrons are shared unequally) to absorb IR radiation, the vibrations of diatomic molecules (e.g. N_2, H_2 etc...) are infrared-inactive.

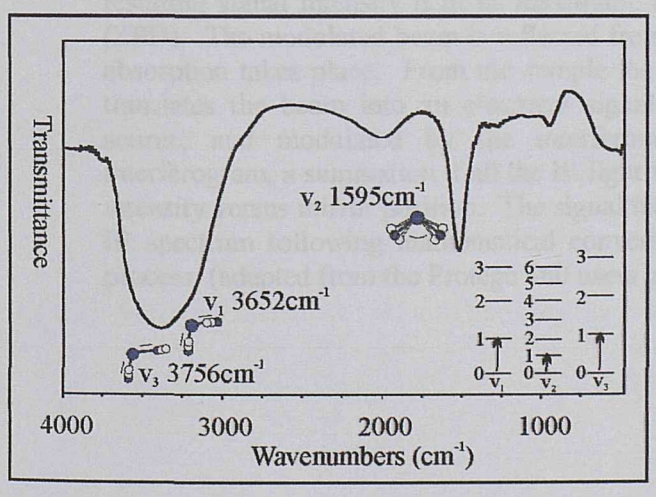

FIGURE 2.4. Infrared spectrum showing the infrared active fundamental vibrations of liquid water.

2.3 FOURIER TRANSFORM INFRARED SPECTROSCOPY

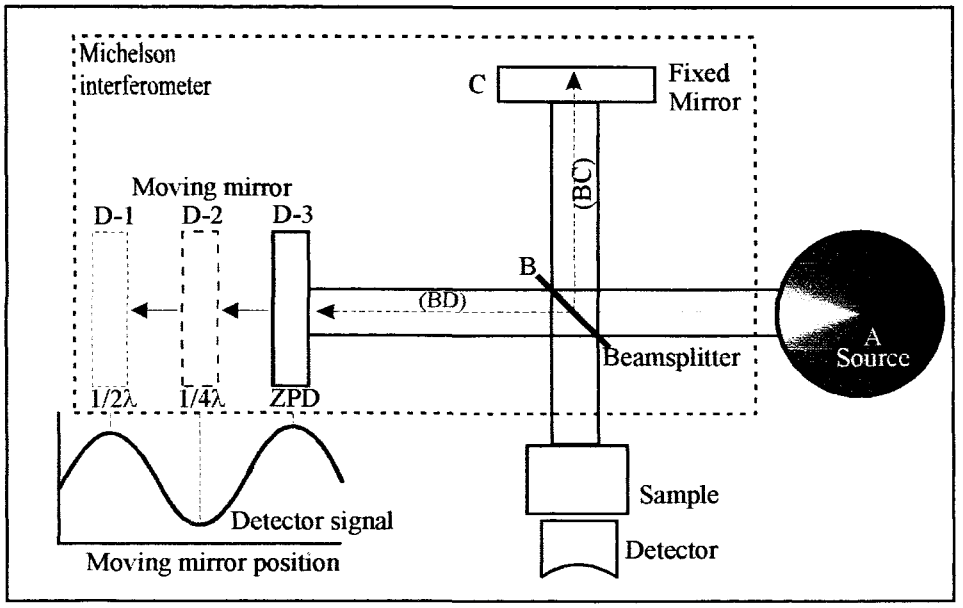

FIGURE 2.5. Schematic representation of the Michelson interferometer. IR light from the source is directed into the Michelson interferometer, the key component of FTIR spectrometry, which modulates each wavelength of IR light to a different frequency. In the interferometer the light beam strikes the beamsplitter. Half of the light is reflected from the beamsplitter and is directed onto the fixed mirror while the remainder is transmitted through the beamsplitter onto the moving mirror. When the beams recombine, constructive or destructive interference occurs depending on the position of the moving mirror relative to the fixed mirror. When both mirrors are the same distance from the beamsplitter, the two reflected beams pass through exactly the same pathlength and, consequently, are totally in phase (distance BC = BD). The resulting signal intensity is at its maximum, a point called the Zero Path Difference (ZPD). The modulated beam is reflected from mirrors to the sample, where selective absorption takes place. From the sample the beam travels on to the detector, which translates the beam into an electrical signal. The cosine waves produced by the source, and modulated by the interferometer, appear to the detector as an interferogram, a summation if all the IR light frequencies represented as a signature of intensity versus mirror position. The signal from the detector is then converted into an IR spectrum following mathematical conversion through a Fourier Transform (FT) process. (adapted from the Protégé 460 users guide)

2.3 FOURIER TRANSFORM INFRARED SPECTROSCOPY

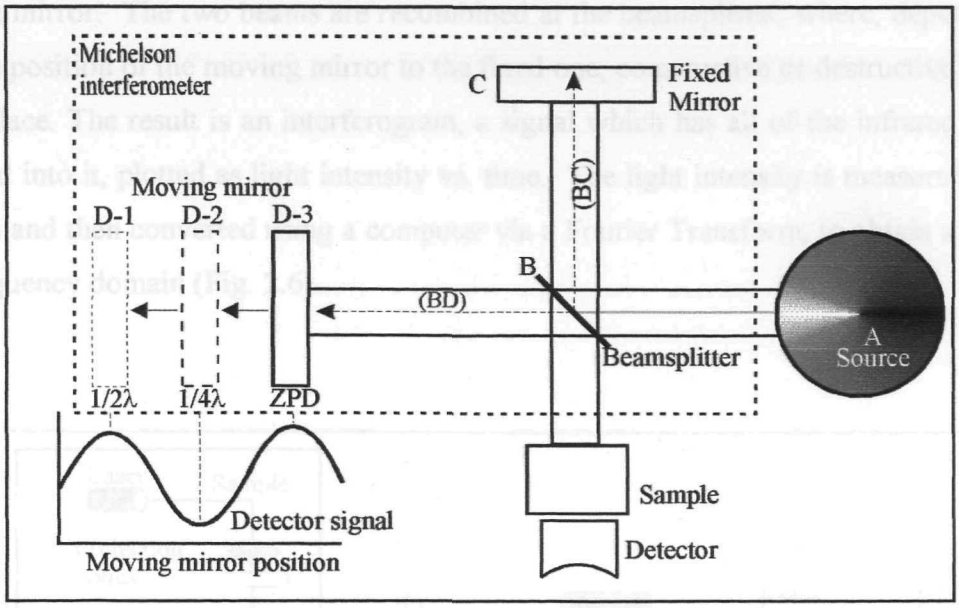

FIGURE 2.5. Schematic representation of the Michelson interferometer. IR light from the source is directed into the Michelson interferometer, the key component of FTIR spectrometry, which modulates each wavelength of IR light to a different frequency. In the interferometer the light beam strikes the beamsplitter. Half of the light is reflected from the beamsplitter and is directed onto the fixed mirror while the remainder is transmitted through the beamsplitter onto the moving mirror. When the beams recombine, constructive or destructive interference occurs depending on the position of the moving mirror relative to the fixed mirror. When both mirrors are the same distance from the beamsplitter, the two reflected beams pass through exactly the same pathlength and, consequently, are totally in phase (distance BC = BD). The resulting signal intensity is at its maximum, a point called the Zero Path Difference (ZPD). The modulated beam is reflected from mirrors to the sample, where selective absorption takes place. From the sample the beam travels on to the detector, which translates the beam into an electrical signal. The cosine waves produced by the source, and modulated by the interferometer, appear to the detector as an interferogram, a summation if all the IR light frequencies represented as a signature of intensity versus mirror position. The signal from the detector is then converted into an IR spectrum following mathematical conversion through a Fourier Transform (FT) process. (adapted from the Protégé 460 users guide)

Fourier Transform infrared spectroscopy is based on the Michelson inteferometer (Fig. 2.5). The interferometer contains a beamsplitter, which splits the light from the source into two beams. Half of the light is directed onto a fixed mirror while the other is reflected onto a moving mirror. The two beams are recombined at the beamsplitter, where, depending on the relative position of the moving mirror to the fixed one, constructive or destructive interference takes place. The result is an interferogram, a signal which has all of the infrared frequencies encoded into it, plotted as light intensity vs. time. The light intensity is measured in the time domain and then converted using a computer via a Fourier Transform, to obtain a spectrum in the frequency domain (Fig. 2.6).

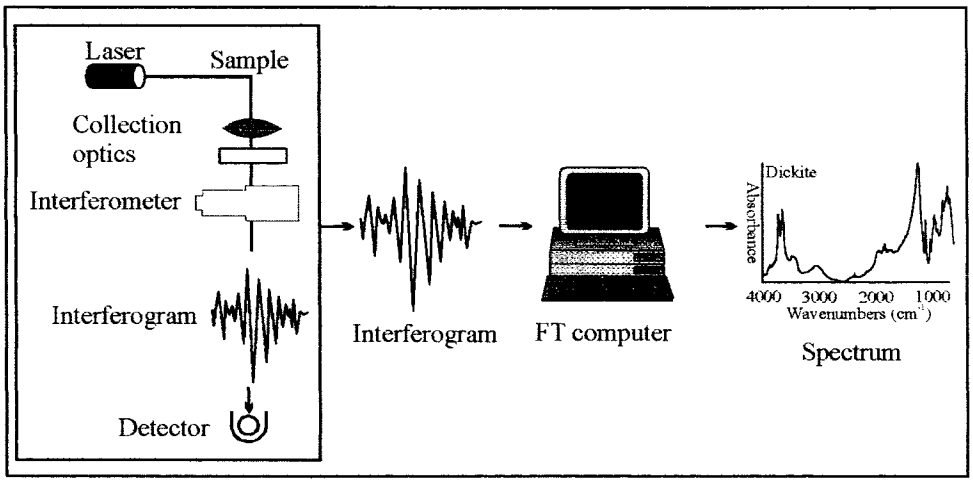

FIGURE 2.6. Schematic representation of the FTIR analysis process. The main units involved in the normal instrumental process are: a) The Source where infrared energy is emitted from a glowing black body source. This then passes through an aperture controlling the amount of energy presented to the sample (and, ultimately to the detector), b) The Interferometer where the beam enters the interferometer and where the specific frequencies or "special encoding" takes place. The resulting interferogram then exits the interferometer and on to, c) The Sample. The beam exits the sample after it has been transmitted through or is reflected off the specimen held in the holder. The type of experiment conducted is dependent on the sample morphology and type of analysis that is being undertaken, d) The beam passes onto the detector for the final measurement. Here the samples unique interferogram signal is measured, e) The Computer where the measured signal is digitised and sent to the computer where the Fourier Transformation takes place. The final FTIR spectrum is then presented to the user for interpretation and further manipulation.

Fourier Transform infrared spectroscopy is based on the Michelson inteferometer (Fig. 2.5). The interferometer contains a beamsplitter, which splits the light from the source into two beams. Half of the light is directed onto a fixed mirror while the other is reflected onto a moving mirror. The two beams are recombined at the beamsplitter, where, depending on the relative position of the moving mirror to the fixed one, constructive or destructive interference takes place. The result is an interferogram, a signal which has all of the infrared frequencies encoded into it, plotted as light intensity vs. time. The light intensity is measured in the time domain and then converted using a computer via a Fourier Transform, to obtain a spectrum in the frequency domain (Fig. 2.6).

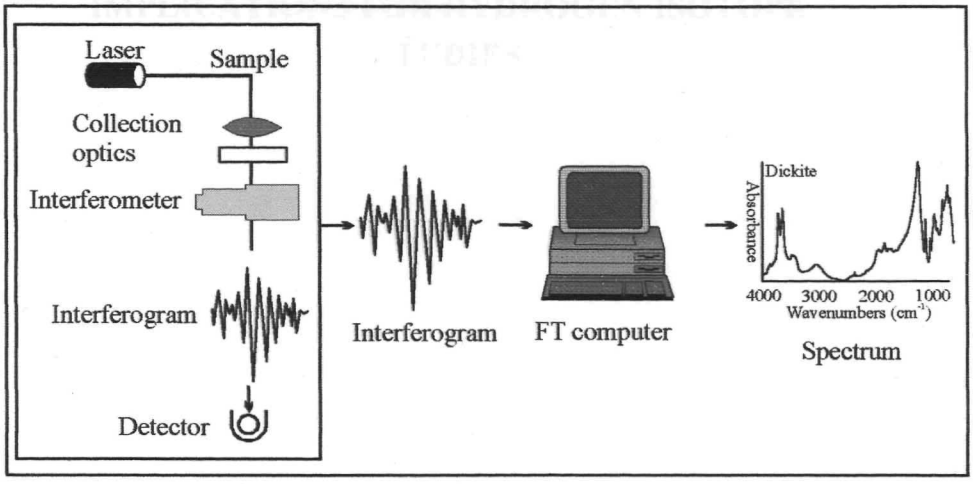

FIGURE 2.6. Schematic representation of the FTIR analysis process. The main units involved in the normal instrumental process are: a) The Source where infrared energy is emitted from a glowing black body source. This then passes through an aperture controlling the amount of energy presented to the sample (and, ultimately to the detector), b) The Interferometer where the beam enters the interferometer and where the specific frequencies or "special encoding" takes place. The resulting interferogram then exits the interferometer and on to, c) The Sample. The beam exits the sample after it has been transmitted through or is reflected off the specimen held in the holder. The type of experiment conducted is dependent on the sample morphology and type of analysis that is being undertaken, d) The beam passes onto the detector for the final measurement. Here the samples unique interferogram signal is measured, e) The Computer where the measured signal is digitised and sent to the computer where the Fourier Transformation takes place. The final FTIR spectrum is then presented to the user for interpretation and further manipulation.

Chapter 3

THE HIGH TEMPERATURE BEHAVIOUR OF HYDROGEN SPECIES IN QUARTZ: IMPLICATIONS FOR HYDROGEN ISOTOPE STUDIES

3 The high temperature behavior of defect hydrogen species in quartz: Implications for hydrogen isotope studies

3.1 INTRODUCTION

Rock forming minerals may be crudely classified into two groups; a) hydrous minerals in which, intrinsic to the mineral structure, hydrogen appears explicitly in the chemical formula, and b) anhydrous minerals containing no essential hydrogen in their chemical makeup (Aines and Rossman, 1984b). However, previous studies have revealed the widespread existence of diverse water species, including molecular water (H_2O), hydroxyl groups (OH^-) and structurally incorporated hydrous complexes (e.g. Si-OH or Al-OH), in minerals considered stoichiometrically anhydrous (Aines and Rossman, 1984b; Rossman, 1988). Indeed, experimental work has shown that substitutional hydroxyl in nominally anhydrous minerals may contribute significantly to the mode of water incorporation in the upper mantle (Aines and Rossman, 1984a; Martin and Donnay, 1972; Smyth et al., 1991).

Due to its sensitivity to the O-H bond, the infrared spectrum between 3200-3600 cm^{-1} provides an extremely sensitive means for detecting minute concentrations of water in minerals (Aines and Rossman, 1984b). Trace 'water' is well know to occur in natural quartz, where Al^{3+} easily substitutes for Si^{4+} in the SiO tetrahedra and additional monovalent cations such as H^+ are incorporated to act as charge compensator ions situated in channels parallel to the c-axis. Hydrogen may also be incorporated into quartz as neutrally charged molecules (Ihinger and Zink, 2000). Because these hydrogen-bearing defects in silica strongly influence the quality of crystals used for the electronics industry (Dodd and Fraser, 1967) the defect chemistry of silica has been examined extensively. Additionally, hydrous defects in quartz cause dramatic weakening of quartz crystals both in both deformation experiments and in nature (Griggs and Blacic, 1965; Kronenberg, 1994; Kronenberg et al., 1986; Post and Tullis, 1998). Hydroxyl groups can be readily distinguished from water molecules following infrared spectroscopic analysis at low temperatures (Kronenberg, 1994).

Stable isotope ratios of oxygen ($\delta^{18}O$) and hydrogen (δD) are extremely important geochemical tracers used to determine the origin of aqueous fluids in geological environments (Sheppard, 1986). Oxygen isotope fractionation between fluids and minerals is widely

documented in the literature (O'Neil, 1986). However, because hydrogen fractionation between anhydrous minerals and water is assumed negligible, experimental determination of equilibrium fluid-mineral hydrogen fractionation factors have been determined solely for hydrous (stoichiometric 'water' bearing) minerals.

The acquisition of δD signatures from fluid inclusions, samples of geological fluids mechanically trapped during crystallisation, provides an invaluable insight into the isotopic composition of ancient fluids. Owing to their microscopic dimensions (typically <20 μm) direct δD determination of individual inclusions is extremely difficult and isotopic analyses are commonly restricted to whole crystals that are crushed (Horita and Matsuo, 1986; Kazahaya and Matsuo, 1985; Kita, 1981; Roedder, 1958) or, more typically, thermally decrepitated (O'Neil, 1986). Interpretation of δD signatures obtained from stoichiometric anhydrous minerals commonly assumes that the hydrogen measured comes uniquely from decrepitated fluid inclusions and the resulting δD signature is attributed solely to this reservoir. Hydrogen bearing species released following mineral decrepitation are assumed to be similar in composition to that of the medium from which the crystal grows (Ihinger and Zink, 2000).

Previous studies have postulated that non-fluid inclusion hydrogen reservoirs may contribute significantly to the δD signature of quartz (Ishayama et al., 1999; Knauth and Eipstein, 1975; Simon, 1997; Simon, 2001). Ishiyama et al. (1999) suggested that hydrogen released following decrepitation at temperatures between 300 and 500°C yield accurate isotopic compositions of the precipitating fluid. However, stepped heating experiments above 500°C yielded increasingly anomalous δD signatures (Ishayama et al., 1999). This study reports on the results of an infrared spectroscopic investigation of hydrothermal vein quartz, known to have anomalous δD compositions, from southern Cornwall, U.K. Infrared spectra collected at increasing temperatures provide a mechanism for observing the liberation of different hydrous species from quartz and provide an opportunity to examine the potential cause of anomalous δD signatures described previously.

3.2 GEOLOGICAL SETTING AND PREVIOUS WORK

The quartz examined in this study was recovered from a series of low temperature, base metal mineralised veins, hosted by Lower Palaeozoic rocks from Porthleven, Cornwall, S. W. England. Detailed description of the geologic setting, petrography, vein composition and isotopic analysis of the vein system analysed are given elsewhere (Gleeson et al., 1999). Quartz in the sample has two distinct morphologies a) fine-grained, cloudy quartz, where individual grains measure several microns in diameter (Q1), and b) coarse-grained, clear prismatic crystals measuring 5mm to 1cm in diameter (Q3) (Gleeson et al., 1999) (Fig. 3.1).

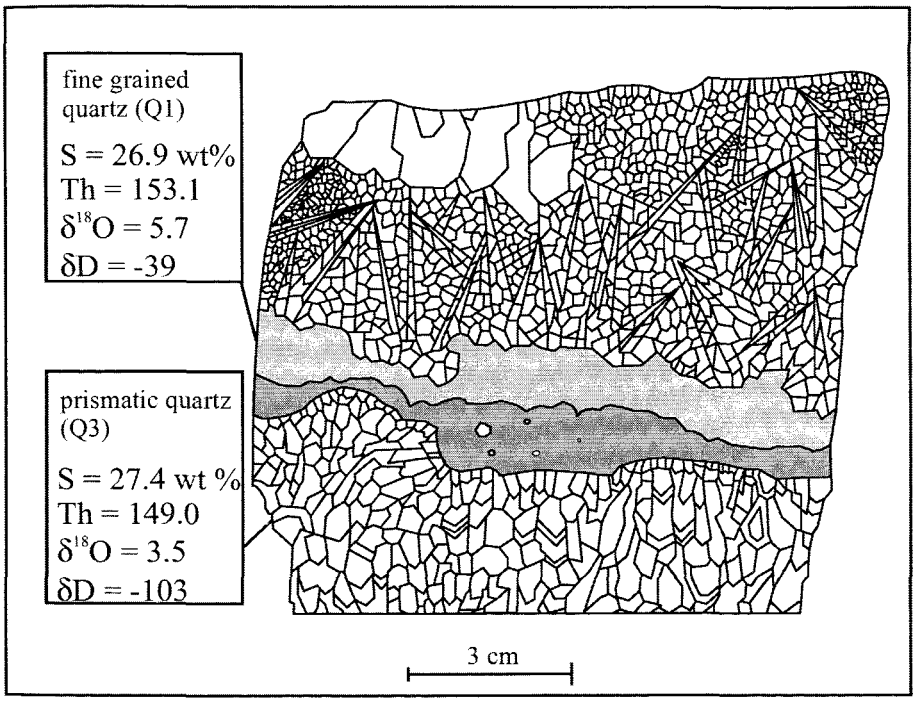

FIGURE 3.1. Sketch of quartz vein SP92018 illustrating quartz morphologies Q1, and Q3, accompanied by the corresponding $\delta^{18}O$ and δD signatures and the homogenisation temperatures of each morphology (Adapted from Gleeson et al. 1999). The diameters of individual quartz grains in samples Q1 and Q3 measure in the range of several microns and 0.5-10mm respectively.

Fluid inclusion data from each morphology are almost identical (Fig. 3.1) suggesting that the mineralising fluids were highly saline (27 wt% NaCl + $CaCl_2$ equiv.), low temperature (130°C) brines, similar in composition to fracture fills found in Permo-Triassic basins to the south of the Cornubian Peninsula (Gleeson et al., 1999).

Oxygen isotope analyses completed on samples Q1 and Q2, using conventional fluorination techniques (Clayton and Mayeda, 1963), revealed vein fluid $\delta^{18}O_{H2O}$ values of between +3.5 and +5.7 ‰ (Gleeson et al., 1999). δD values, obtained by thermal decrepitation (at approx. 1100°C), which expels all hydrogen from the sample regardless of the position and type within the quartz (Simon, 2001), vary significantly between -39 and –103 ‰ (e.g. Fig. 3.1). Such anomalous δD values, accompanied by relatively constant $\delta^{18}O$ signatures, have been reported from moderate to highly saline inclusion fluids, with a range of homogenisation temperatures (<100 to 270°C) in a number of different geological environments (Charef and Sheppard, 1987; Foxford, 1992; Kelly and Rye, 1979; Munoz et al., 1997; Munoz et al., 1994; Wilkinson et al., 1995) leading to significant controversy regarding the origin of fluids in these systems. Several factors have been proposed to account for these irregular δD signatures (Charef and Sheppard, 1987; Hall et al., 1991; Marvrogenes and Bodnar, 1994; Munoz et al., 1994; Polya et al., 2000; Sheppard, 1986; Sheppard and Charef, 1986; Simon, 1997). Post-entrapment changes by hydrogen diffusion through quartz (Hall et al., 1991; Marvrogenes and Bodnar, 1994; Post and Tullis, 1998) seems unlikely as no relationship between the relative age of the vein and the δD signature has been identified (Gleeson et al., 1999). Fluid from high latitude and high altitude fluid sources (Sheppard, 1986; Winograd et al., 1985), are inconsistent with paleoaltitude and paleolatitude estimates for the region at the time of vein formation (Briden et al., 1974). Mass balance calculations suggest that K-mica contamination of the samples would contribute insufficient water to the total water budget to generate sufficiently low values (Gleeson et al., 1999). The geological environment of vein crystallisation suggests the formation of organic waters, which have compositions in the range –90 to –250 ‰, by the modification of organic compounds is unlikely (Gleeson et al., 1999). The present study addresses the results of several recent reports: 1) suggesting that different reservoirs in quartz may lead to the release of fluids with variable δD signatures (Simon, 1997; Simon, 2001) and; 2) detailing the results of a stepped heating isotopic study which describes the release of anomalous δD signatures at increasing temperatures (Ishayama et al., 1999).

3.3 ANALYTICAL TECHNIQUES

Determination of hydrous species in each sample was performed on 200 μm thick, double polished fluid inclusion wafers of whole sections of vein. The thickness of each wafer was checked with a micrometer. Due to the nature of the sample material, spectroscopic analysis of accurately orientated crystals was not possible. Specimens of each sample measuring several millimeters in length were prepared. Prior to spectroscopic analysis, individual samples were first inspected under an optical microscope and regions free of fluid inclusions selected for further analysis. While the coarse grain-size and large dimensions of the fluid inclusions in the coarse-grained sample (Q3) made identification of suitable regions for spectroscopic investigation easy, the fine grained nature of Q1 made similar distinction between suitable and unsuitable regions for study more difficult.

To quantify the liberation of hydrous species at increased temperatures, in-situ, high temperature infrared analyses were carried out on a Linkam™ THM600 heating/freezing stage placed on the sample stage of an infrared microscope. Stage temperature was regulated using a Linkam TMS92 control unit which controls the temperature with an accuracy of ± 0.5°C. The temperature of the sample compartment was increased at a heating rate of 20°C/min up to the desired value. To remove any possible contamination by adsorbed water, and in an attempt to replicate the initial isotopic analytical procedure (Gleeson et al., 1999), samples were first heated to 100°C prior to infrared analysis.

Low temperature analyses were performed on the same Linkam™ TH600 stage as described for the heating experiments. The enclosed sample compartment was cooled at a rate of 20°C/min to -150°C by the flow of liquid nitrogen through heat exchange tubing surrounding the sample stage. To prevent freezing of atmospheric water on the specimens the sample stage was purged with N_2 gas. N_2 gas was also blown onto the double window of the sample compartment to prevent the extensive build-up of frost on the glass at low temperatures.

Infrared spectra were obtained using a Nicolet Protégé 460 Fourier Transform infrared spectrometer coupled with a Nicolet infrared microscope. The IR beam is reflected via a KBr beamsplitter and focused through the sample onto a liquid nitrogen cooled mercury-cadmium-

telluride (MCT) detector. A programmed aperture of 100 μm x100 μm was used to the collect spectra for each sample.

Peak positions were determined by measuring the position of local maximum absorbance on the spectrum. Following each analysis the resulting spectrum was fitted to a background and the respective intensity of each peak associated with individual defects recorded.

According to the Beer-Lambert law, the intensity of the infrared absorbance band generated, A, is proportional to the concentration of the absorbing species, C, [mol/l] and the sample thickness, d [cm] by way of the molar absorption coefficient, ε [l mol^{-1} cm^{-1}]:

$$A = \varepsilon \cdot C \cdot d$$

In-situ infrared measurements were obtained using the transmission technique. Samples were placed directly onto the heating stage of the apparatus and infrared spectra were collected, initially at 25°C, and then at 100°C increments between 100°C and 600°C. Owing to difficulties in obtaining reasonable spectra at high temperature, a background reference spectrum was collected at 25°C and stored on the computer. This was then subtracted automatically from the spectra resulting from the in situ, high-temperature analyses. Because the intensity of the absorption is reduced at high temperatures, difficulties in accurately determining the presence of hydrous species at high temperatures were encountered. To overcome these problems, at each high temperature increment, following collection of the high temperature spectrum, the sample was cooled to 25°C using the heating/freezing stage and additional spectra were obtained. This technique permitted the resolution of individual hydrous species remaining after each successive heating increment.

3.4 RESULTS

3.4.1 Characterisation of hydrous species

Individual samples analysed in this study were first inspected under an optical microscope and fluid inclusion free regions selected under the microscope field of view for micro-infrared analysis. In the infrared spectrum of fine-grained quartz sample (Q1) obtained at 25°C (Fig. 3.2), the dominant broad absorbance (X on Fig. 3.2) centred at 3440 cm^{-1} closely resembles that of liquid water (Aines and Rossman, 1984b). Analysis at -150°C displaces the absorbance band to 3200 cm^{-1} due to the freezing of molecular water (Fig. 3.2). The dominant hydrous species in fine-grained sample Q1 is molecular water.

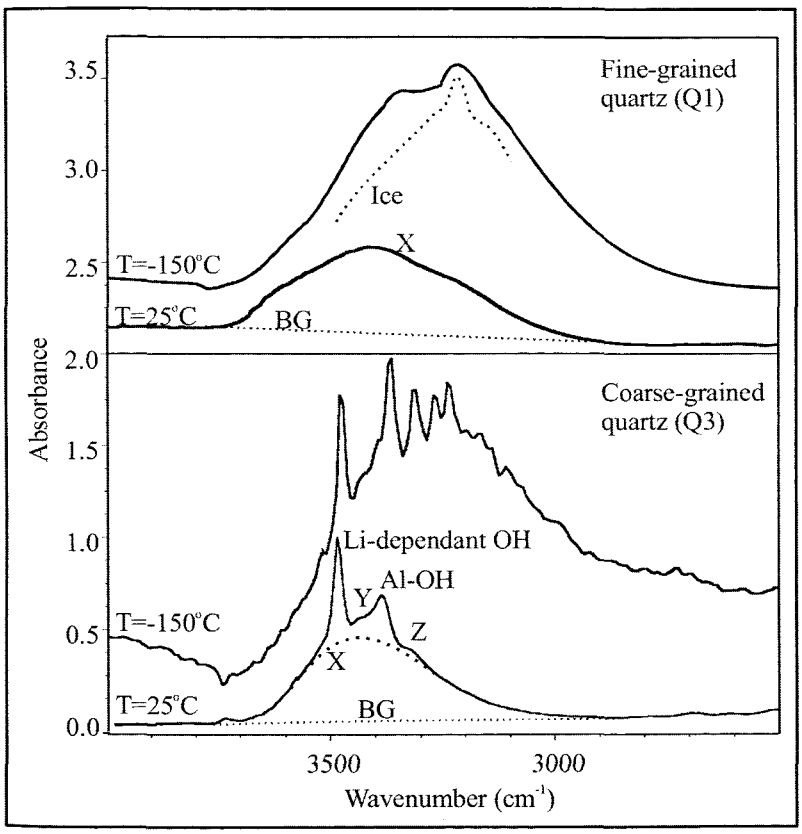

FIGURE 3.2. Unpolarised infrared absorption spectra of fluid inclusion free vein quartz sample SP92018 at 25 and 150°C. Spectra were obtained on 200 μm thick, randomly orientated double polished, fluid inclusion wafers of each sample type. Infrared spectra of sample Q1 obtained at 25°C exhibit a dominant strong absorbance centered at ~3440 cm^{-1} which closely resembles that of molecular water (Aines and Rossman, 1984b). At -150°C the spectrum generated by sample Q1 is dominated by a broad absorption band at 3200 cm^{-1} due to the freezing of molecular water to ice (broken line) (Aines and Rossman, 1984b), and a peak at approximately 3385 cm^{-1} associated with Al-OH defects. Analysis of sample Q3 at25°C between 3200 and 3600 cm^{-1} generates two intense absorptions at 3485 and 3385 cm^{-1} accompanied by additional smaller peaks at 3577, 3484 and 3321 cm^{-1} attributed to various OH species. Sharp bands on the spectra of sample Q3 measured at -150°C are superimposed on a broad absorption, again centered at 3200 cm^{-1}, probably due to frost on the sample.

In the spectrum obtained at 25°C following analysis of coarse-grained sample Q3, two, dominant sharp absorption bands at 3485 and 3385 cm^{-1} are accompanied by several less intense shoulders at 3438 and 3321cm^{-1} (bands Y and Z respectively, Fig. 3.2). Bands at 3385 and 3321 cm^{-1} are assigned to OH stretching vibrations involving oxygen and interstitial hydrogen impurities, incorporated following the substitution of Si^{4+} by Al^{3+} (Aines and Rossman, 1984b; Niimi et al., 1999) while those at 3485, and 3438 cm^{-1} are associated with Li-dependant hydrogen defects (Kronenberg, 1994). The exact speciation of these Li-dependant OH centres remains unclear (Paterson, 1989). At -150°C sharp absorptions attributed to OH vibrations near to Al^{3+} and Li^{+} impurity cation defects, which are superimposed upon an asymmetric broad band absorption due to frost on the sample, become sharper and more intense and (Fig. 3.2).

3.4.2 Concentration of hydrous species

As stated above, if sample thickness remains the same, the intensity of the band generated by an absorbing species is intimately linked to the absolute concentration of that species. If we assume that the absorbencies generated at 3385 and 3485 cm^{-1} associated with Al-OH and Li-dependant OH centres respectively are superimposed upon a broad band absorption generated by molecular water, the intensity of the underlying water peak can be inferred (Fig. 3.2). Using the spectra presented on Figure 3.2, bands measuring 1 and 0.8 absorbency units are generated by molecular water in samples Q1 and Q3 respectively. Accordingly, our spectroscopic investigation into the hydrous species in the samples suggests that both quartz types contain comparable quantities of hydrogen in the form of molecular water. Additionally, Figure 3.2 shows significant variation between the absorption intensities of bands associated with the defect species in each sample.

3.4.3 IR bands at high temperatures

The infrared spectra of sample Q1, recorded between 2500 and 4000 cm^{-1}, during an in situ heating experiment from 25° to 600°C are shown on Figure 3.3. At 25°C the spectrum is dominated by a single broad absorbance, centred at ~3440 cm^{-1}, associated with the vibrations of molecular water. At 100°C, a shoulder at 3577 cm^{-1}, is apparent at a frequency resembling that previously described and attributed to a hydrogen defect associated with Al (Niimi et al., 1999). As temperature is increased, the intensity of the 3440 cm^{-1} band decreases and the band at 3577cm^{-1} becomes more pronounced. The two peaks show similar intensities on the spectra at 300 and 400°C. Between 400 and 500°C a significant reduction in the intensity of the broad band absorption at 3440 cm^{-1}, from 0.55 to 0.33 absorbency units, is observed. The peak at 3577 cm^{-1} dominates the spectra recorded at 500 and 600°C. At these temperatures, the 3440 cm^{-1} band is almost undetectable.

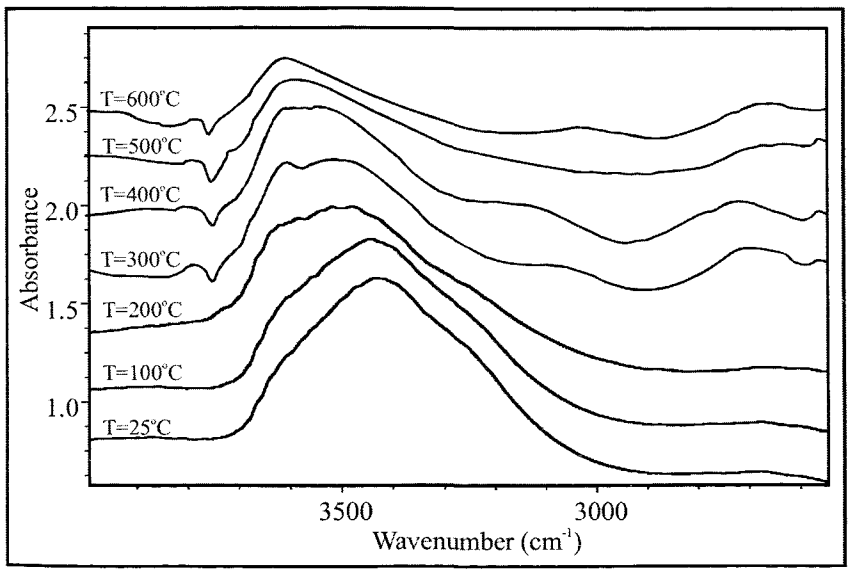

FIGURE 3.3. High temperature, infrared absorption spectra of quartz sample Q1 measured between 25 and 600°C. The spectra show the reduction of the broad band absorption centered at 3440 cm^{-1}, attributed to molecular water in the sample, with increasing temperature. Numbers inset indicate the temperature at which the spectra were obtained. The background was used to ratio each of the analyses was collected at 25°C.

The high temperature behaviour of defect hydrous species in coarse-grained sample Q3 was also examined between 25 and 600°C (Fig. 3.4). From 25 to 200°C the number of visually identifiable peaks decreases from five to two. At 200°C, the peak at 3321 cm^{-1}, associated with Al-OH, along with that at 3438 cm^{-1} and an additional shoulder at 3510 cm^{-1}, both associated with Li-dependant OH vibrations, are no longer evident on the spectrum. At higher temperatures, significant broadening of the bands at 3485 and 3385 cm^{-1}, coupled with a general reduction in the intensity of the absorbance associated with each band is observed. At 600°C the appearance of a band at 3569 cm^{-1}, similar to that described at high temperatures in sample Q1 is noted.

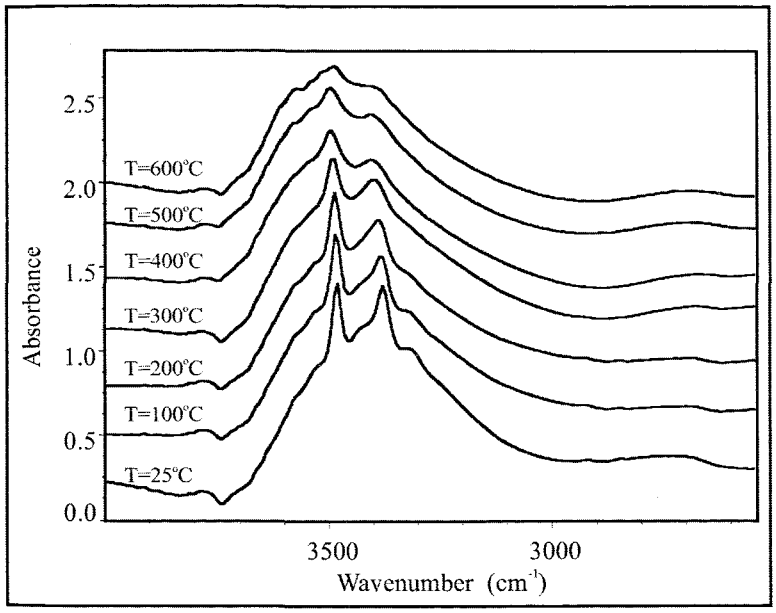

FIGURE 3.4. Infrared absorption spectra of coarse-grained quartz sample Q3 at increasing temperatures from 25 to 600°C. Numbers inset indicate the temperature at which individual spectra were taken. At 25° several less intense peaks at 3318, 3436 and 3580 cm^{-1} accompany two intense peaks at 3380 and 3480cm^{-1}. At higher temperatures, both the number of peaks visible on the spectra and the intensity of these peaks decrease. These features may be attributed to a) the removal of the absorbing species, or b) decreased molar absorptivity with increased temperature. A broadening of the bands is also observed at high temperatures.

3.4.4 Stepped heating experiments

In order to establish whether the observed spectral changes are associated with variation in the absolute concentration of absorbing species of a sample, stepped heating experiments, followed by subsequent infrared analysis at 25°C were performed. Such analyses provide an accurate measure of the concentration of absorbing species remaining in the sample following each heating increment, without contamination of the vibrational characteristics of the sample due to changes in the crystal structure caused by the molecular response to increased temperature.

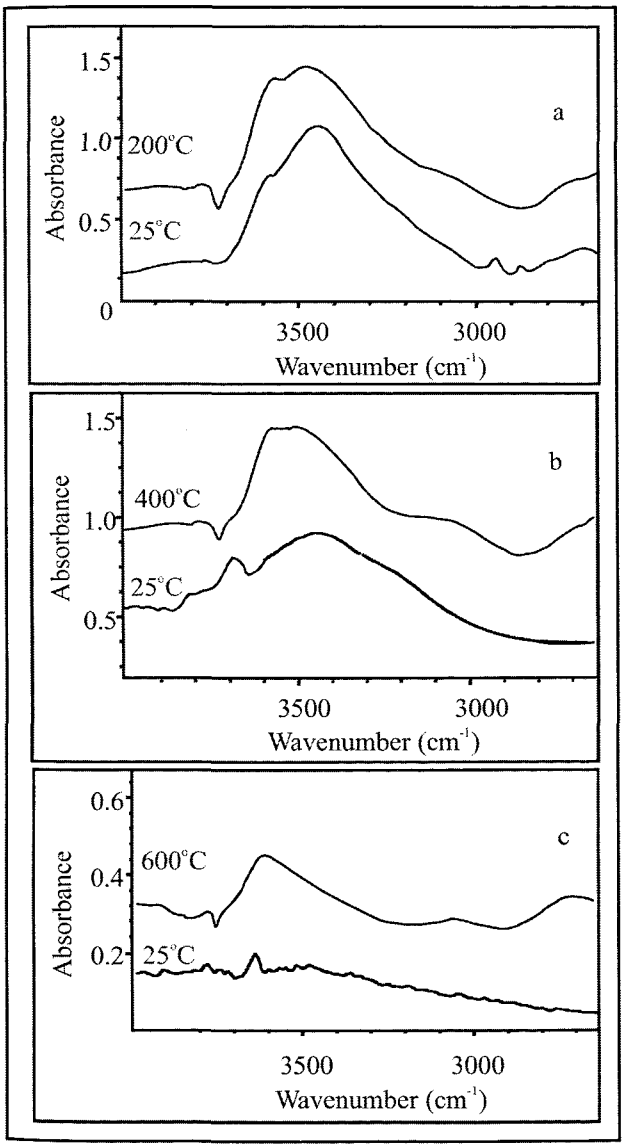

FIGURE 3.5. Infrared absorbance spectra of fine-grained sample Q1 measured in situ at a) 200, b) 400 and c) 600°C. Also shown on each diagram are the spectra obtained at 25°C of the sample cooled from the corresponding temperature increment.

Figure 3.5 displays the results of stepped heating analyses of Q1 measured at 200, 400 and 600°C along with the spectra recorded at 25°C, after cooling the sample from each corresponding temperature. On the spectrum recorded at 25°C following heating to 200°C, the intensity of the band centred at 3440 cm^{-1}, associated with molecular water in the sample, remains similar to that recorded before any heating experiments. On the spectrum recorded at 25°C following heating to 400°C the intensity of this band has been reduced from 0.7 to less than 0.5 absorbancy units (Fig. 3.5.b). An additional band at 3740 cm^{-1} also becomes evident on this spectrum. This band becomes increasingly clear in the spectrum recorded at 25°C following heating to 600°C (Fig. 3.5.c). This spectrum also shows the band associated with molecular water in the sample centred at 3440 cm^{-1} has been completely removed following heating to 600°C.

Figure 3.6 shows the results of stepped heating experiments performed on sample Q3. The analytical procedures employed were the same as those outlined for sample Q1 and displayed on Figure 3.5. Comparison between the infrared spectra of sample Q3 initially collected at 25°C, then heated to 200 and cooled to 25° demonstrate that, although not apparent on the spectrum obtained in situ at 200°C, peaks at 3321, 3438 and 3510 cm^{-1} are readily identifiable on the spectrum obtained upon cooling to 25°C (Fig. 3.6a). Additionally, comparison between the intensities of the three infrared bands recorded at 25°C, prior to the heating experiment, with those evident on the spectra obtained at 25°C on samples cooled from 200°C, show no significant reduction of the bands. Because the absolute concentration of the absorbing species is intimately linked to the intensity of the absorbance by the Beer-Lambert equation, it is suggested that no significant loss of the species has occurred. As a result, the apparent removal of bands at 3321, 3438 and 3510 cm^{-1} from spectra obtained at temperatures above 200°C is interpreted to be to be associated with decreased molar absorptivity of the absorbing species at high temperatures, rather than actual physical loss of the species.

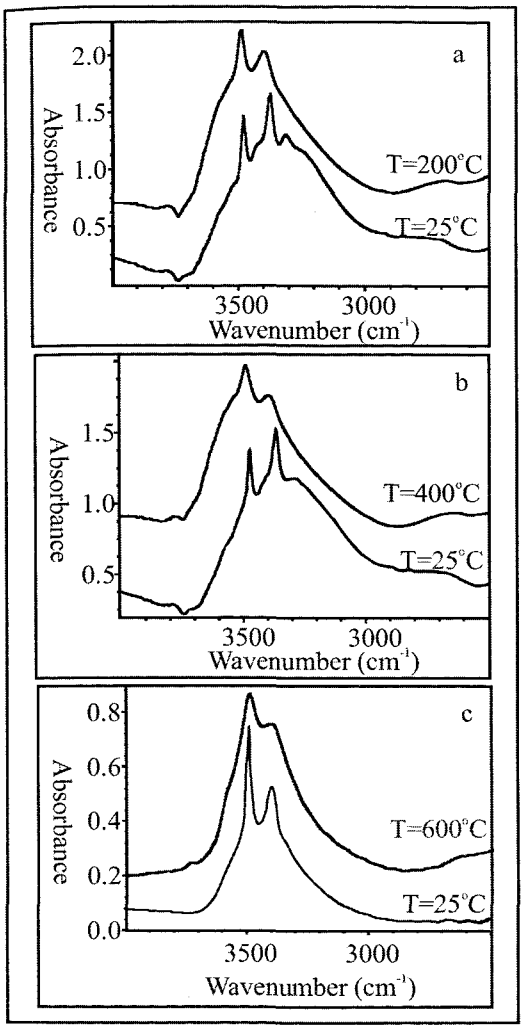

Figure 3.6. a) Infrared absorbance spectra of sample Q3 measured in situ at 200°C, then subsequently cooled to 25°C and re-analyzed. Although at 200°C the number of bands is reduced from those initially present (Fig. 3.2) cooling of the sample and re-analysis at 25°C shows the spectrum is identical to that prior to heating. Accordingly, the reduced number of bands on the spectrum obtained in-situ at 200°C is attributed to a reduction in the molecular absorptivity, rather than physical loss, of the absorbing species. b) Infrared absorbance spectra of sample Q3 measured in situ at 400°C, then subsequently cooled to 25°C and re-analyzed. The spectrum recorded at 25°C shows no significant reduction in the intensity of the sharp bands at 3380 and 3480 cm^{-1} suggesting that, up to 400°C, no significant loss of Al-OH and Li-dependant OH species has taken place. c) Infrared absorbance spectra of sample Q3 performed in situ at 600°C and then subsequently cooled to 25°C. The intensities of the Al-OH and Li-dependant OH bands remain similar to those recorded at 25°C prior to heating. Accordingly, these results show that A-OH and Li-dependant species are stable at temperatures up to 600°C.

In contrast to the original spectrum recorded at 25°C, the spectra of coarse-grained sample Q3 measured in situ at temperatures of 200 and 400°C show only two pronounced peaks at 3485 and 3385 cm^{-1} (Fig. 3.4). In situ analysis of sample Q3, heated to 400°C then cooled to 25°C, reveals the bands at 3438 and 3510 cm^{-1} associated with Li-dependant OH species, to be no longer evident on the spectrum. Accordingly, it is suggested that heating quartz to 400°C effectively liberate these OH-related species from the sample (Fig. 3.6b). Peak intensities of the bands associated with Al-OH defects at 3385 cm^{-1} and Li-dependant OH centres at 3485 cm^{-1} are identical to their original values prior to any heating of the sample which, according to the Beer-Lambert relationship, suggests that the absolute concentration of these species remains unaffected by heating of the sample to these temperatures.

At temperatures exceeding 400°C two prominent bands at 3385 cm^{-1} and 3485 cm^{-1} continue to be recognised, although at higher temperatures these bands become progressively broader and reduced in intensity (Fig. 3.4). A shift in the vibrational frequency of both centres to progressively higher wavenumbers at elevated temperatures is associated with the thermal expansion of the crystal (Suzuki and Nakashima, 1999). Analysis of the sample cooled to 25°C from 600°C shows that although bands at 3321, 3438 and 3510 cm^{-1} are no longer evident on the spectrum, the intensity of the absorptions at 3385 and 3485 cm^{-1} remain unaltered from the values recorded prior to any heating experiments (Fig. 3.6c). Accordingly, our experiments suggest that heating quartz up to 600°C is insufficient to liberate these defect species from the sample.

3.5 DISCUSSION

3.5.1 Hydrous species in the samples

Although optical microscopy suggests that fine-grained sample Q1 contains significantly fewer fluid inclusions than coarse-grained Q3, the dominant broad band absorption centred at 3440 cm^{-1} demonstrates that, in both samples, submicroscopic aggregates of molecular water are the volumetrically significant hydrous species. The presence of submicroscopic aggregates of liquid water in Q1 is further elucidated following infrared analysis at –150°C (Fig. 3.2). In sample Q3 sharp, narrow Al-OH and Li-dependant OH vibrations at 3385 and 3485 cm^{-1}, are superimposed upon the vibrations caused by these submicroscopic water domains. Although the absolute concentration of molecular water present in the two samples may be similar, i.e. the broad band absorption centred at 3440 cm^{-1} is of similar intensity in both quartz types, the hydrogen defect population in the coarse-grained samples is sufficiently large to generate absorption bands with significant peak absorbancies which exceed the peak absorbance of the broad band due to molecular water. This indicates that, although a molecular water component probably dominates, interstitially incorporated defect species may represent an additional hydrogen reservoir. This is not the case in fine-grained quartz Q1, where the maximum intensity of absorption bands due to Al-OH and Li-dependant OH defects were not detected above the level of the broad band molecular OH absorption (Fig. 3.2). Considering this, the maximum intensity of the band associated with Li-dependant OH defects must measure less than 0.6 absorbency units. This compares to the measured 1.4-absorbency units in sample Q3 (Fig. 3.2). Based on our ability to detect sharp absorption bands due to hydrogen defects, the coarse-grained quartz must contain, at a minimum, twice the concentration of those in the fine grained samples. Further inspection of the spectra recorded at 25°C following heating to 600°C (Fig. 3.5), reveals that the resulting dehydrated spectrum in fact shows no peak associated with defects in the sample. Stepped heating experiments of defect-rich sample Q3 shows that heating to 600°C does not remove defect species associated with the peaks at 3484 and 3384 cm^{-1}. Accordingly, hydrogen defects in sample Q1 (Fig. 3.5c) contain do not represent a significant fraction of the total hydrogen in the sample. Absolute concentrations of defect species continue to be volumetrically small in Q3 but a larger contribution to the overall hydrogen budget may be expected. Hydrogen defects may

thus explain the correlation between the broad and sharp infrared absorption bands and the 'normal' δD signature (Gleeson et al., 1999).

3.5.2 Cause of anomalous δD signatures

Variations in temperature, incongruous isotopic composition of the parent fluid, disequilibrium effects and isotopic fractionation into a mineral may all contribute to variations in isotopic signature (O'Neil, 1986). In the samples examined in the present study, fluid inclusion data negates large variations in temperature (Gleeson et al., 1999). The contemporaneous incorporation of both fluid inclusions and trace elements (Sisson et al., 1993) suggests crystallisation from distinct parent media is improbable and parent fluids with sufficiently depleted signatures contradict the accepted model proposed for regional vein formation (Gleeson et al., 1999). Because coarse-grained sample Q3, which generates an anomalous δD signature, contains, in addition to a molecular water component, a potentially significant defect hydrogen reservoir, it is suggested that relationship between the two provides an possible explanation for the observed anomalous signature. Fractionation of hydrogen species adsorbed onto quartz has been previously reported (Simon, 2001). Following inspection of the spectroscopic data obtained in this study, it is suggested that liberation of fractionated hydrogen from defect sites in the mineral structure of sample Q3 presents a plausible explanation for the observed isotopic signatures.

The sign and magnitude of isotopic fractionation into a mineral may be influenced by temperature, pressure, chemical characteristics and the crystal structure (O'Neil, 1986). It is well documented that structurally incorporated Al-OH centres form following the substitution of an Si^{4+} with an Al^{3+}. In order to retain charge neutrality, this process needs to be charge compensated with the additional incorporation of a monovalent cation (Aines and Rossman, 1984b; Kronenberg, 1994; Paterson, 1989). This may result in the replacement of an oxygen atom with an OH molecule (Paterson, 1989). In quartz, OH-Al forms a hydrogen bond with another adjacent oxygen and bond lengths of between 2.7 Å (Nakamoto et al., 1955) and 3.329 Å (Suzuki and Nakashima, 1999) have been proposed. A relationship between short hydrogen bond length and deuterium content in minerals has been previously reported (Graham et al., 1980). Pectolite uniformly produces the lowest δD values (-429 to -281‰) of any terrestrial mineral (O'Neil, 1986) but also displays possibly the strongest hydrogen bond

found in any mineral (Hammer et al., 1998). Even the most generous bond length estimates described for quartz (Suzuki and Nakashima, 1999) suggest a significant degree of hydrogen fractionation into the Al-OH defects sites may be anticipated during quartz crystallisation. Bifurcating OH(Al) hydrogen bonds strongly influenced by several adjacent oxygens (Suzuki and Nakashima, 1999) may further complicate the fractionation process. Isotopic fractionation depends not only on absolute vibrational frequency but also the frequency shift upon substitution. Because water and hydroxyl have a tendency to incorporate the light isotope until high temperatures are reached, isotopic fractionation is greatest at low temperatures. Accordingly, the incidence of anomalous δD ratios reported from (relatively) low temperature geological environments is probably not fortuitous.

3.5.3 Significance of High Temperature Analysis

Although the defect structure of Al-OH species is well constrained, the exact speciation of the Li-OH defect remains uncertain. Li-dependant OH species may be incorporated as neutrally charged molecules (Ihinger and Zink, 2000) or form following the substitution of Si^{4+} with Li + 3H (Paterson, 1989). H-OH species are incorporated as neutrally charged molecules (Ihinger and Zink, 2000). As these species are bound within the quartz lattice by quite different mechanisms, one might reasonably expect to respond differently to increasing temperature. Preferential liberation of any species within a temperature range would influence the isotopic signature obtained within that temperature interval.

Previous studies have shown that in quartz samples heated to 1000°C, dehydration of the crystal effectively removes all Li-dependant OH and aggregates of molecular water species from the crystal. However, even after heating to 1000°C for one hour, structurally bound Al-OH defects remain (Suzuki and Nakashima, 1999). In the present study, stepped heating experiments between 25 and 600°C were carried out in an attempt to correlate spectral changes associated with the dehydration of the crystal, caused by the specific removal of aggregates of molecular water and Li-dependant OH species, with increased in anomalous δD signatures previously recorded in hydrothermal quartz (Ishayama et al., 1999).

Previous workers have noted significant variance in the isotopic signature of hydrogen liberated from quartz at different temperatures (Ishayama et al., 1999; Knauth and Eipstein,

1975). Ishiyama et al. (1999) noted that the hydrogen released from quartz at temperatures up to 500°C was similar in composition to that of the local meteoric waters whereas water released at elevated temperatures was significantly lighter in composition. They suggested that hydrogen liberated at less than 500°C was meteoric in origin and attributed hydrogen released at greater than 500°C to a different, unknown source. High temperature infrared analysis performed in this study suggests that, at temperatures up to 500°C, H-OH species along with certain Li-dependant OH are significantly liberated. Our findings indicate that these centres, which are incorporated into the crystal structure as neutrally charged molecules (Ihinger and Zink, 2000), are more readily liberated at temperatures <500°C than structurally incorporated hydrous (Al-OH) species. It is suggested that, without any structural controls placed on the incorporation of these neutrally charged hydrogen species by the crystal structure, isotopic fractionation into each of the molecules is minimal and, in accordance with Ishiyama et al. (1999), conclude that these reservoirs accurately record the isotopic signature of the precipitating fluid. High temperature infrared analysis suggests that certain Li-dependant OH species begin to be liberated at temperatures above 600°C and are significantly depleted at 1000°C (Suzuki and Nakashima, 1999). These workers found that Al-OH centres remain stable even following heating to 1000°C for one hour. Accordingly, it is suggested that rather than recording the isotopic composition of a discrete water source, hydrogen released at temperatures exceeding 500°C divulges the isotopic composition of hydrogen which has been fractionated into structurally incorporated Al-OH and Li dependant OH defect sites during crystal growth.

3.5.4 Implications for Hydrogen Isotope Studies

Fluid inclusion capture occurs at (1) kinks in crystal growth steps or (2) atomistic hollows or cracks on the crystal surface that are subsequently covered by successive growth steps (Sisson et al., 1993). Following adsorption at crystal surfaces, impurities (trace elements) are enclosed within successive growth steps and incorporated into the crystal structure. Fluid inclusions and trace elements represent samples of the same crystallising medium sampled adjacent to the crystallisation front during crystal growth. Contemporaneous incorporation implies that each of the two reservoirs should yield identical δD signatures. This is clearly not the case.

If we assume, 1) the δD signature released by fluid-inclusion rich samples following decrepitation at temperatures up to 500°C records the true δD signature of the original precipitating fluid (Ishayama et al., 1999) and, 2) the δD signature released by defect-rich samples represents a composite signature of the original fluid composition and the hydrogen fractionated into defect sites of quartz structure, simple mass balance can assess the concentrations of each reservoir needed to generate the observed δD signatures. The δD composition of the original precipitating fluid is taken to be -40‰ (Wilkinson et al., 1995), while the δD signature of the defect hydrogen is taken as -200‰ (Gleeson and Roberts: In prep). Mass balance calculations suggest that 50% of the total hydrogen budget needs to be contributed by defect hydrogen to attain the δD signature observed for sample Q3. Indeed, our previous observation, describing the intensity of the absorbencies generated by the samples Q1 and Q3, suggests this to be a reasonable assumption.

Chapter 4

IDENTIFICATION OF HYDROTHERMA ALTERATION MINERALS: A CASE STUDY FROM THE CHELOPETCH AU-CU DEPOSIT, BULGARIA

4 Identification of hydrothermal alteration minerals: A micro-FTIR study of clays from the Chelopech Au-Cu deposit, Bulgaria

4.1 INTRODUCTION

A zone of intense alteration is a diagnostic feature surrounding hydrothermal mineral deposits. Commonly providing an exploration target considerably larger than the orebody itself, hydrothermal mineral zones not only indicate the physical and chemical conditions experienced by the system, but also to some degree, the nature of the geothermal fluid responsible (Beane and Bodnar, 1995; Beane and Titley, 1981). In the mineral exploration environment, prompt and precise identification of alteration mineral assemblage zones significantly enhances efficiency in describing and characterising new hydrothermal systems (Reyes, 1990). Additionally, increased understanding of the crystallisation of alteration minerals may provide key insights into the ore-forming mechanisms involved (Finch et al., 1995; Munoz, 1984; Munoz, 1992; Munoz and Swenson, 1981; Nash, 1976; Selby and Nesbitt, 2000). Due to the fine-grained nature of many alteration minerals and their lack of diagnostic features, alteration mineral assemblages are frequently difficult to assess in the field. Traditional methods of characterisation use time consuming and costly laboratory-based analytical techniques, such as X-ray diffractometry and both optical and electron microscopy.

Recently, the Portable Infrared Mineral Analyser (PIMA), a small, short-wave infrared spectrometer (SWIR), has been employed to rapidly provide field geologists with mineralogical information on rocks, minerals and soils (Thompson et al., 1999). SWIR spectrometers detect reflected molecular vibrational energy and have been increasingly applied to mineral exploration (Huston et al., 1999; Kruse and Hauff, 1991; Shen et al., 1999; Stewart and Kamprad, 1997; Sun et al., 2001; Thompson et al., 1999; Yang et al., 2001; Yang et al., 1998; Zhang et al., 1998). SWIR spectroscopy provides a quick and reliable technique for the detection of phylosilicates, clays, carbonates and selected sulphates and is sensitive to the vibrations of individual mineral species (Pontual et al., 1995). Due to the nature of the instrument, which records infrared radiation reflected off the sample surface, PIMA uses near infrared radiation, in the 1.3 μm to 2.5 μm range of the electromagnetic spectrum. Fundamental constrains upon the analytical aperture placed on spectroscopic techniques lies not with the physical process of restricting the diameter of the radiation used to analyse the

sample, but with problems associated with diffraction of that radiation by a small aperture. The resulting analytical aperture of the PIMA is around 1cm. Due to the minute size of alteration minerals compared to this aperture, the resulting spectra represents a complex mixture of many individual mineral spectra and may miss significant, small scale mineral zonation.

Mid-infrared spectroscopy measures the interaction of radiation with the molecules of the sample of interest between 650 and 4000 cm^{-1} (25 and 2.5 μm). Accordingly, a technique employing a mid-infrared source is going to be inherently better for analysing smaller sample sizes. In addition, many of the fundamental vibrations of the molecular constituents of minerals lie in the mid-infrared. FTIR spectrometers have now been commercially available for over 25 years, and recently, with the significantly enhanced spatial resolution of the FTIR microscope, have found numerous academic and industrial applications. In an infrared microscope, the incident beam is focused on the sample using a parabolic mirror, and the transmitted light collected using a reflecting optics (Cassegrain) objective. This set-up produces a system with an effective analytical aperture of 10μm. Prior to the development of FTIR, infrared analysis was predominantly carried out in the transmittance mode. However, the increased speed and sensitivity of FTIR has revolutionised spectroscopy and enabled the development of numerous techniques such as Attenuated Total Reflectance (ATR), diffuse reflectance, photoacoustic spectrometry, infrared microscopy, long path spectroscopy and remote fibre optic spectroscopy (Rintoul et al., 1998).

The development of new spectroscopic techniques has also significantly widened the nature of the sample analysed. Whereas prior to the development of FTIR, infrared spectroscopy was primarily used in the identification and analysis of organic compounds, it currently is used in the study of diverse samples from minerals, living cells, thin films and biological tissues (Rintoul et al., 1998). The advent of the FTIR microscope presents the opportunity to analyse hydrothermal minerals on a micron scale, and the added possibility of analysing samples remotely using fibre optic technology presents workers in the exploration industry with an exciting new analytical technique. Clearly this will enable workers to analyse alteration mineralogy on a scale not previously realised, a resolution which may generate new insights into the nature of the hydrothermal processes involved. This chapter reports on the application of various micro-FTIR spectroscopic techniques and sample preparation methods

in characterising minerals. Significant difficulties in accurately determining the spatial extent of the economic orebody underground are frequently encountered in the Chelopech Au-Cu deposit, Bulgaria. The lack of dependable mineral identification commonly leads to continued extraction of rock beyond the economically viable orebody, into the hydrothermally altered, although less mineralised country rocks. A primary objective of this study was to use micro-FTIR to establish alteration mineral zones within the orebody. As a comparison with infrared spectral method, mineral species were also determined by XRD analysis. The data obtained by both approaches are in good agreement and show similar changes along the analytical traverse. The results of this study indicate the potential of micro-FTIR as a complimentary technique to those currently employed for targeting potential mineralisation.

4.2 INFRARED SPECTROSCOPY AS A TOOL FOR CLAY IDENTIFICATION

4.2.1 Techniques and instrumentation

Infrared spectra were obtained at room temperature using a Nicolet Protégé 460 Fourier Transform infrared spectrometer coupled with a Nicolet infrared microscope. The infrared beam is passed via a KBr beamsplitter and focused through the sample onto a liquid nitrogen cooled mercury-cadmium-telluride (MCT) detector. 128 scans were collected for each analysis and ratioed against a background programmed into the computer. This enabled the collection of a sample spectrum in around 30 seconds. Spectra were recorded in the 650-4000 cm^{-1} range.

4.2.2 The identification of minerals using infrared spectroscopy

During an infrared experiment, the fundamental vibrations of a powdered material represent an intricate combination of the individual vibrations of each infrared active molecular system present in the sample. Accordingly, the complexity of the mineral suite present in the sample and the degree of overlap of the component spectra are critical factors in determining the efficiency of infrared spectroscopy as a tool for distinguishing component mixtures. The interpretation of an infrared spectrum of a complex sample mixture requires the positive identification of as many absorption bands of individual species as possible. The important molecular vibrations of any phyllosilicate create absorptions in the infrared which may be crudely classified into three groups (Fig. 4.1):

1) Vibrations associated with the fundamental stretching (between 3750 and 3400 cm^{-1}) and bending (Between 950 and 600 cm^{-1}) vibrations of structural OH groups.

2) Stretching vibrations associated with cation-oxygen lattice motions (generally at around 1000 (Si-O stretching) and 500 cm^{-1} (Si-O bending)).

3) Vibrational bands, which commonly overlap those attributable to lattice vibrations, attributable to absorbed species. For example, the OH stretching region of hydration water may obscure the 3640 and 3400 cm^{-1} spectral domain.

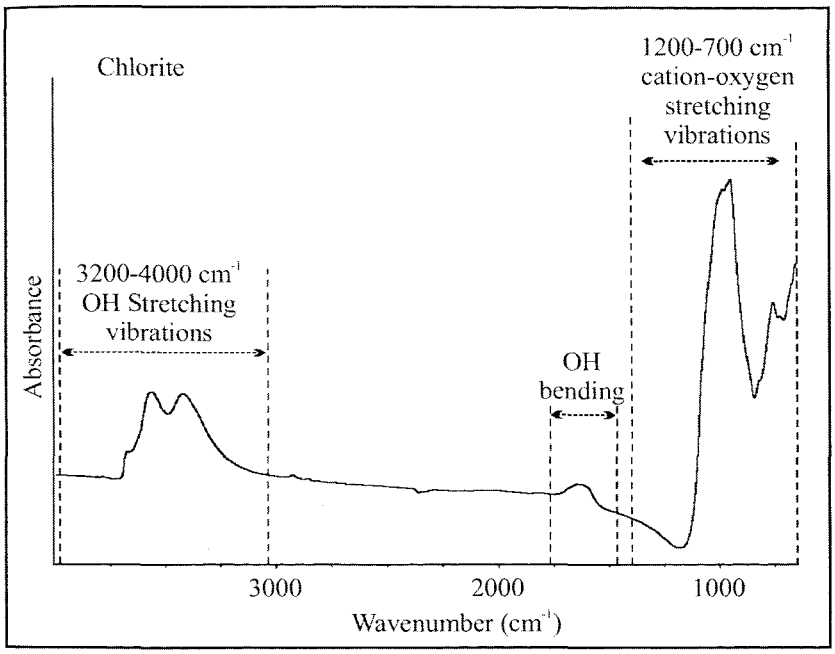

FIGURE 4.1. Infrared absorbance spectrum of chlorite displaying frequency range associated with the most important lattice vibrations in mineral identification.

Bands appearing at 2350 cm^{-1} on some mineral spectra are caused by the antisymmetric stretching mode of atmospheric CO_2. This band reflects conditions experienced by the system during the analytical process and not attributable to the sample.

The correct identification of clays from a mineral mixture relies heavily on the availability of well-characterised reference spectra. Numerous useful collections of mineral spectra have been published in the literature (Farmer, 1974a; Marel and Beutelspacher, 1976), are commercially available (e.g. via the USGS) and are now available via the Internet (e.g. www.galactic.com). In identifying clay minerals, although analysis of the full spectrum

provides the best possible interpretation, vibrations associated with OH stretching motions are probably the most effective region of the spectrum.

4.2.3 Advantages of infrared spectroscopy over XRD analysis

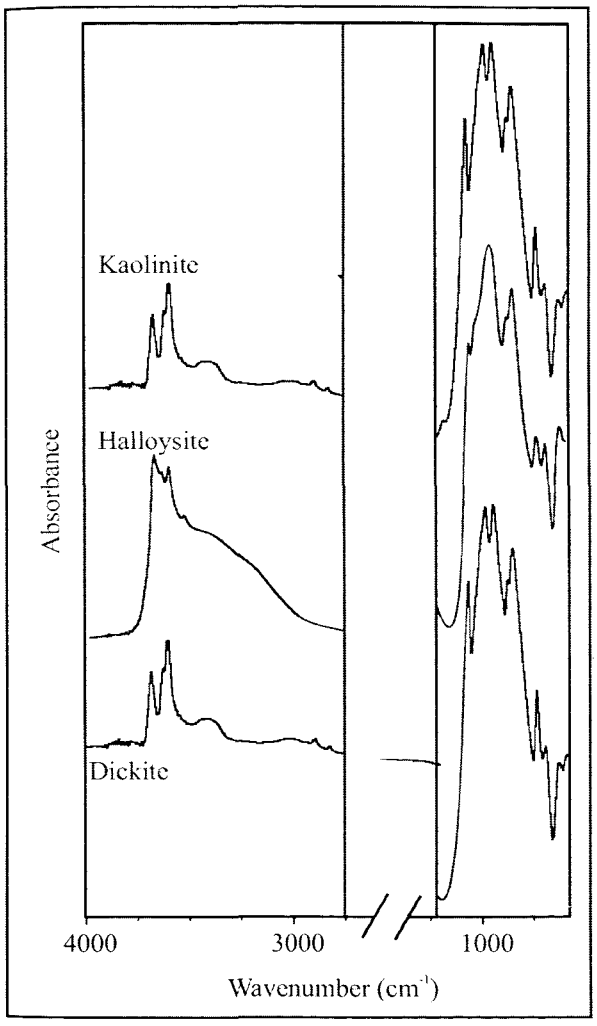

FIGURE 4.2. Infrared spectra of kaolin minerals: a) well-crystallised kaolinite, b) halloysite, c) dickite.

The absorption of infrared radiation by any material arises due to the fundamental molecular vibrations of its constituents. The frequencies of these vibrations are dependent upon the mass of the individual atoms, the restraining forces of the bonds and the geometry of the structure. The resulting infrared absorption spectrum is characteristic of the properties of the specimen analysed and may serve as a fingerprint for its identification. In addition, infrared spectroscopy can also give unique information on structural features of the mineral, including the nature of isomorphic substitution, the differentiation of the water molecule from constituent hydroxyl, and the degree of regularity of the structure (Farmer, 1986).

TABLE 4.1. Frequencies of the fundamental vibrations of the kaolin group of minerals

Kaolinite	3697	3669	3652	3620		1108	1036	1014	938	916	795	758	701
Dickite	3704	3681	3654	3621		1118	1033	1000	935	912	794	755	696
Halloysite	3695	3620	3602	3550		1090	1032	1013	911		790	752	690

Using conventional XRD analysis, although detection of kaolinite in the presence of chlorite is possible following heat treatment or dissolution of the sample in hydrochloric acid, significant analytical uncertainties exist (Hauff and Cocks, 1996; Kodama and Oinuma, 1963). On the other hand, discrimination between the most common kaolinite minerals, kaolinite (Fig 4.2a), halloysite (Fig. 4.2b), and dickite (Fig. 4.2c), is relatively easy using infrared spectroscopy (Table 4.1). The ability to see differences between the different kaolinite phases may prove significant in understanding a hydrothermal system because dickite can be indicative of higher temperatures and a slightly different pH than kaolinite (Deer et al., 1992).

4.2.4 The effect of sample preparation on sample spectrum

Samples were prepared by crushing the whole rock into a fine (<2μm) film from which the clay fraction was separated. Infrared spectra were collected on ground fractions of the sample using KBr disks. The sample was ground into a fine powder using an agate mortar and pestle and dispersed throughout spectroscopic quality KBr powder. The mixture was placed in a die and a hand held Spectra-Tech Handi-Press formed the transparent to semi-transparent pellets. A metal collar that fits into the KBr holder, coupled with cardboard dies generates pressed powder pellets with diameters of 1, 3 or 7 mm depending on the quantity of sample available for analysis. Using the smallest die set provided, between 0.005 and 0.003 mg of sample was required to generate a pellet. The prepared disk was then mounted over a hole in the sample stage and the spectrum for the sample recorded. Analysis of a sample-free disk was then performed to obtain a reference spectrum. The ratio of these two spectra gives an infrared transmission spectrum for the sample analysed.

TABLE 4.2. Frequencies of the absorptions generated following the analysis of an XRD standard kaolinite sample. a) Peaks generated following analysis of a KBr pressed powder disk of the sample, and b) spectrum generated following the analysis of a sample of kaolinite removed from the packaging and pressed roughly onto an infrared transparent NaCl window.

Kaolinite	Peaks												
KBr disk	3697	3669	3652	3620	1108	1036	1014	938	916	795	787	758	701
NaCl window	3697	3667	3649	3621	1104	1038	1015	939	916	798	790	756	703

Although the KBr pressed disk technique is the generally accepted as the standard sample preparation procedure for the analysis of minerals, the diameter of clay particles, are by definition are already of satisfactory size (<2mm). As field-based mineral identification requires the analysis of samples with the minimum of preparation, analyses were carried out on an XRD kaolinite standard which had been prepared both as conventional KBr disks and as an untreated sample roughly pressed onto the sample window (Fig 4.3). Table 4.2 shows that although the intensities of bands generated by the two techniques vary significantly, identification of the mineral species present is still possible using the quicker, sample preparation technique.

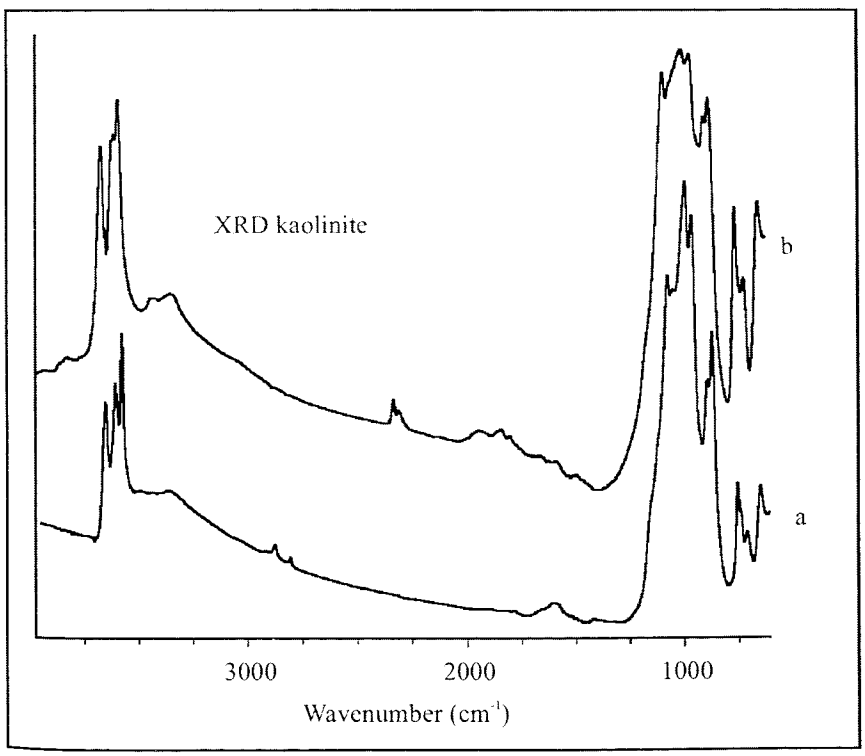

FIGURE 4.3. Infrared absorption spectra of an XRD standard sample of kaolinite. a) sample prepared as a standard pressed powder KBr disk, b) sample removed from the sample bag with no preparation and pressed firmly onto a infrared transparent NaCl window.

4.2.5 The effect of sample concentration on the resulting spectrum

Ideal sample preparation requires the preparation of pressed disks where sample concentrations measure between 0.2 to 1% of the quantity of KBr powder (Russell, 1974). The sample spectrum is significantly influenced by the quantity of sample present under the infrared beam. To assess the influence sample concentration:KBr ratio has on the resulting infrared spectrum, disks were prepared using various sample contents (Fig. 4.4). Results of an X-ray diffraction standard kaolinite sample, prepared and analysed correctly are shown on Figure 4.4b. Also shown for comparison are the spectra obtained following analysis of kaolinite disks containing low (Fig. 4.4a), and high (Fig. 4.4c) concentrations of sample to the same content of KBr. The analytical aperture of the infrared beam was controlled manually, dependent upon the size of the sample, using two knife blades located on the IR microscope. The resulting spectra are plotted on relative absorbance scales and have been arbitrarily shifted vertically for clarity. Examination of Figure 4.4c shows that if the sample concentration is too great, resolution of individual peaks is quickly lost. If the sample concentration is too small, much greater detail is observed in the strongest peaks on the spectrum (i.e. between 560 and 1100 cm^{-1}) but resolution is lost between the less intense peaks (between 3000 and 4000 cm^{-1}). Accordingly, it may be necessary to prepare several disks to obtain an accurate sample spectrum displaying the desired resolution between peaks at different frequencies.

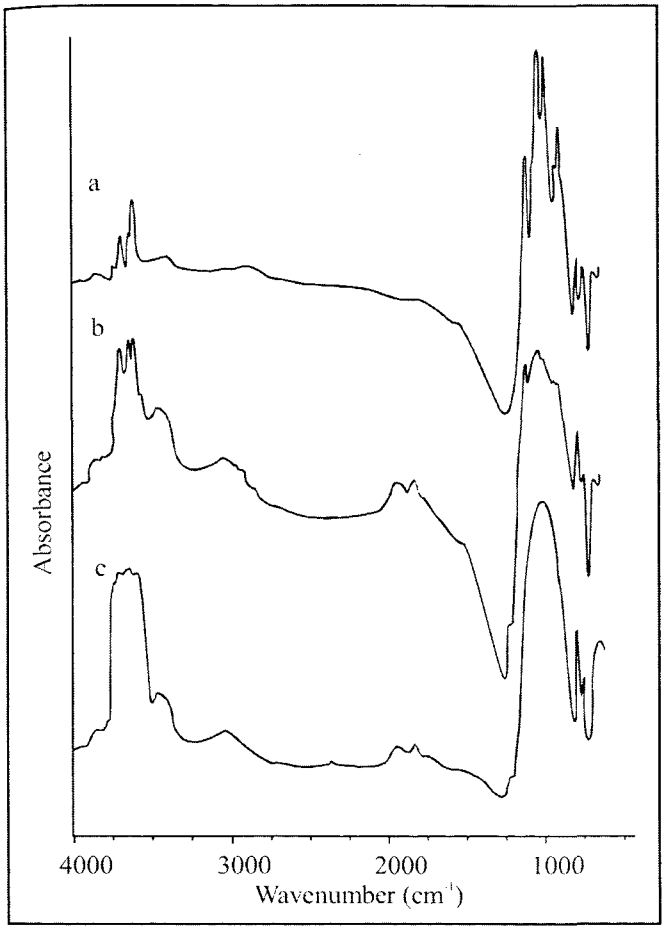

FIGURE 4.4. Infrared spectra of an XRD standard sample of kaolinite from Chihuagua, Mexico illustrating the significance of sample thickness during the analytical procedure. Disks are prepared with a) a minimal sample quantity, b) the correct amount of sample and, c) too much sample. The spectrum obtained with small sample concentration shows good resolution of the strong bands between 650 and 1100 cm^{-1} but band identification at higher wavenumbers is difficult. Identification of the OH stretching bands between 3000 and 400 cm^{-1} is easier in the correctly prepared disk, while absorptions generated by all molecular vibrations in the disk containing too much lack resolution.

4.2.6 Mineral identification using different spectroscopic methods

Prior to the advent of FTIR, infrared analysis was predominantly carried out on powdered samples using the transmission method (Chapter 2). As stated previously, the inherent efficiency and sensitivity of FTIR has enabled the development of several spectroscopic techniques which are based around the identification of vibrations using the reflection of infrared radiation off the sample. A potentially significant breakthrough in spectroscopic determination of mineral identity will be the employment of remote fibre spectroscopy, whereby the user will ultimately have a portable mid-infrared spectrometer with a fibre optic attachment, which is placed onto the sample point of interest to collect the sample spectrum. A critical difference between many of the published mineral spectra with those that would be obtained using such technology is that while most published spectra were collected using the transmittance technique, fibre optic technology would use the reflectance method.

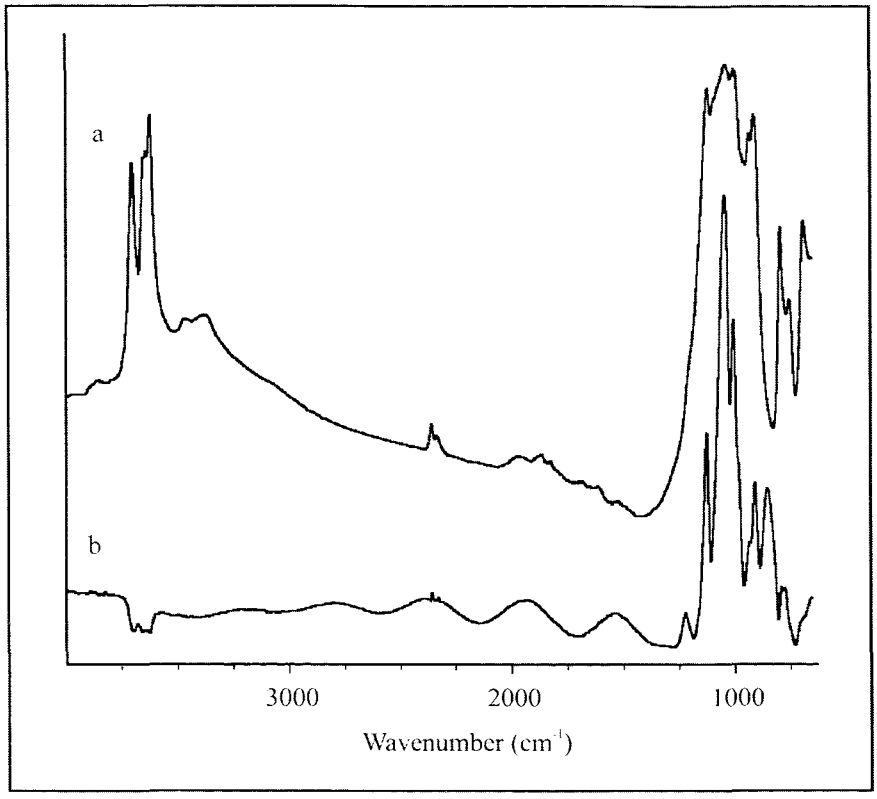

FIGURE 4.5. Infrared spectra obtained following analysis of an XRD kaolinite standard using a) infrared absorption and b) infrared reflection spectroscopy.

Diffuse reflectance spectroscopy measures the intensity of the reflectance of infrared radiation off a highly polished surface. The resulting spectra, although broadly similar to those generated using transmittance spectroscopy, may differ markedly in samples were the refractive index varies widely with wavelength (Russell, 1974). A critical problem encountered with earlier attempts to correlate transmittance and reflectance spectra was achieving sufficiently large signal to noise ratio (Aronson et al., 1966). Since the advent of FTIR spectroscopy, with its inherently increased signal output, little work has been undertaken to determine the relationship between mineral spectra obtained using transmittance and reflection techniques. Such evaluations are of great importance to workers investigating hydrothermal systems as they may ultimately enable rapid field-based determination of assemblages using field portable infrared spectrometers. The large variability that exists between the hydroxyl configurations of different clay species suggests that examination of the hydroxyl stretching region of the vibrational spectrum should provide an accurate identification of the sample. However, Nakashima et al (1995) suggested that reflectance spectroscopy did not provide sufficient resolution between individual hydroxyl vibrations to

enable accurate mineral identification. In an attempt to quantify the suitability of reflection spectroscopy in determining the composition of clays, an XRD standard kaolinite was analysed using transmittance and reflection spectroscopy (Fig. 4.5).

Attenuated Total Reflectance spectroscopy involves the measurement of the internal reflection of a sample through an internal reflection element mounted on the infrared microscope. A common sampling technique in many modern laboratories (Rintoul et al., 1998), the resulting spectrum obtained using an internal reflection element is, in many cases identical to that produced using transmission spectroscopy, enabling direct comparison between the sample spectrum with those published.

TABLE 4.3. Frequencies of the fundamental vibrations of a kaolinite XRD standard analysed using infrared reflectance and transmittance spectroscopy

Kaolinite	Peaks														
Reflectance	3694	3667	3662	3617	1122	1042	1006	987	936	912	855	790	776	706	660
Transmittance	3697	3669	3652	3620	1108	1036	1014		938	916		795	787	758	701

Table 4.3 contains the fundamental vibrations of an XRD kaolinite standard prepared as a pressed KBr disk recorded using diffuse infrared reflection and transmittance techniques. Transmittance spectra were obtained using the techniques outlined above. Reflectance spectra were collected through a 100×100μm aperture at the top of the microscope. A gold foil standard was used to collect the sample background and the two spectra ratioed against each other to obtain the sample spectrum as outlined for the transmittance technique. Table 4.3 contains data for log 1/R, which enables a direct comparison between the vibrational bands obtained using the two techniques to be obtained.

4.3 APPLICATION OF INFRARED SPECTROSCOPY TO THE IDENTIFICATION OF ALTERATION MINERALS FROM CHELOPECH

4.3.1 Geological Setting

The Chelopech Au-Cu deposit is situated 60km east of Sofia, Bulgaria (Fig. 4.6). Hosted in Upper Cretaceous andesitic to rhyodacitic pyroclastics and sub-volcanic intrusives, the deposit lies in the central part of the Srednogorie structural-metallogenic zone. A high-sulphidation gold-enargite epithermal system (Bonev et al., 1998), Chelopech is Europe's largest gold deposit. It contains in excess of 6 million ounces of gold, and with ore reserves and resources totalling 57Mt grading 1.24%Cu, 3.38g/t Au (Andrew, 1996).

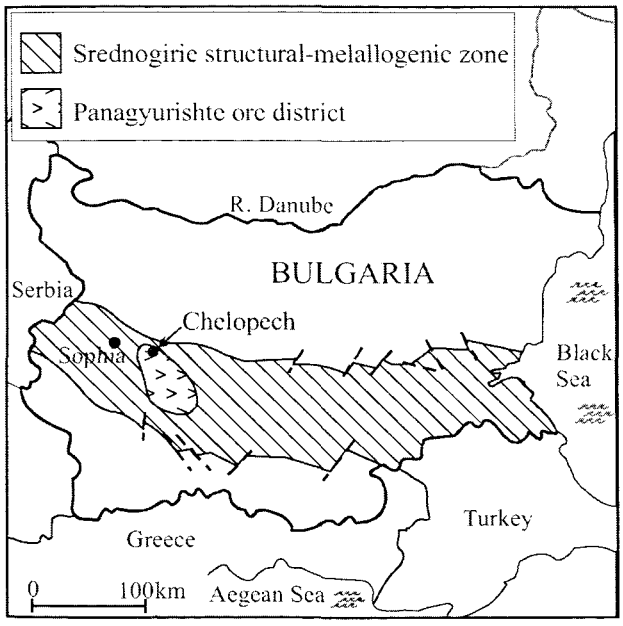

FIGURE 4.6. Location map of the Chelopech Au-Cu deposit.

4.3.1.1 Stratigraphy

Basement rocks in the region of the Chelopech deposit consist of granites, crystalline two mica schists, quartzites and amphibolites. These are unconformably overlain by the Coniacian-Santonian Lower Chelopech Formation, a basal sequence of siltstones and calcareous argillites, with subordinate terriginous sandstones and angular basal breccio-conglomerates, which predates mineralisation (Andrew, 1996). Upwards these sediments become intercalated and eventually superseded by andesitic agglomerates, andesitic lavas, lapilli, and psammitic tuffs. Subvolcanic bodies of mesocratic, porphyritic andesites containing sub-vertically-imbricated phenocrysts of feldspar, biotite, amphibole and, rarely, quartz intrude the entire sedimentary sequence.

Above the volcano-sedimentary sequence complex of the Upper Chelopech Formation lies a thin sequence of red to grey argillaceous limestones and grey to dark blue calcareous argillites. Minor interbeds of silty and sandy limestones also occur in the upper parts of the sequence, which contains microfaunal evidence of an Upper Turonian to Campanian age.

4.3.1.2 Mineralisation

Ore bodies at Chelopech are represented by irregular, sulphur-rich replacement of silica-sericite propylitic altered andesites, andesitic tuffs and breccias (Terziev, 1966). Lens-type orebodies, measuring between 150-300m in length and 30-120m thickness, comprise the bulk of the presently known ore-reserve (Andrew, 1996). Mineralisation is controlled by and predominantly located along, and proximal to, radial and concentric faults (Terziev, 1966). Central parts of each orebody are dominated by fine-grained massive sulphides (predominantly pyrite and chalcopyrite) (Terziev, 1971). The mineralogy at Chelopech is extremely complex and to date 71 mineral species have been identified. Chief ore minerals are irregularly distributed pyrite, chalcopyrite, tennantite, enargite, luzonite, bornite, galena and sphalerite (Todorov, 1991). Pyrite content gradually diminishes outwards and leads to the precipitation of increasingly complex sulphides. Peripheral to the pyrite dominated core is a chalcedonic silica-rich zone containing additional galena, sphalerite and other sulphides (Andrew, 1996). Gold distribution is closely controlled by a zone of intense silicification adjacent to active structures (Todorov, 1991). Pyrite (and marcasite, melknikovite etc.) forms 20% by volume of the orebodies. Quartz, barite and kaolinite are the dominant gangue minerals with subordinate chlorite, ankerite and gypsum. About 65% of the copper is in the

form of arsenides and sulphosalts and about 35% chalcopyrite. Gold usually occurs as native metal (Todorov, 1991) but may also be present in auriferous tellurides such as nagyagite, sylvanite and kostovite (Andrew, 1996).

Distinct horizontal and vertical zonation is observed in the main orebody at Chelopech. Copper ore is found at depth while lead-zinc ore dominated mineralisation at higher levels. Uppermost is a barite zone, which may be locally enriched in fluorite (Terziev, 1971). Terziev (1966) described the zonal distribution of minerals at Chelopetch as closely resembling that described for Butte, Montana.

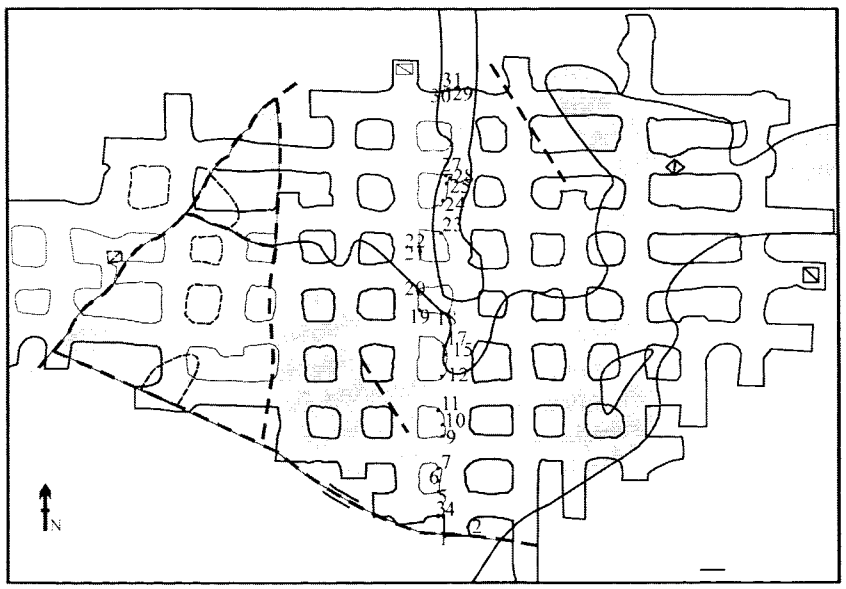

FIGURE 4.7. Geological sketch map of the underground adit of the Chelopech deposit from which the samples were taken

4.3.2 Materials and Methods

Underground mapping of the deposit by mine geologists determined a zone of intense silicification, which hosts a zone yielding the most economically productive ore. The orebody is hosted by a volcanic breccia and a felsic porphyry. To maintain analytical consistency, only samples from the porphyry were selected for study. Fist sized samples of rock were collected at successive 10m intervals along an underground traverse of a working mine adit (Fig. 4.7). Sample A1 represents unsilicified rock from the outermost extremities of the mineralised

orebody. Rock to the south of this position is deemed un-minable due to a significant reduction in the metal grade.

Infrared spectra were collected using the instrument described in section 4.2.1. Following the results of the experiment described in section 4.2.4, individual phenocrysts were separated by hand from the groundmass using a scalpel and pressed onto an infrared transparent NaCl window for analysis. An aperture of 100mm was used to analyse different sections of the NaCl window to obtain spectra with the resolution desired for interpretation of the absorbencies in different regions of the spectrum (section 4.2.5).

4.3.3 Results

4.3.3.1 Infrared spectra

Representative infrared spectra obtained following analysis of individual phenocrysts extracted from samples obtained at different positions throughout the traverse (Fig. 4.7) are reproduced on Figure 4.8. The frequencies of the fundamental vibrations generated by each sample are listed on Table 4.4. From these, two types of alteration mineral assemblage may be identified by infrared spectroscopy throughout the analytical traverse. The fundamental vibrations of sample A1 are quite different to those produced by all of the other samples.

Sample A1

Sample A1 represents the analysis of the clay fraction of a sample which lies just outside the main silicified zone of the orebody (Fig. 4.7). The infrared spectrum produced by the sample shows a major OH stretching vibration at 3628 cm^{-1}, accompanied by a very broad band of reduced intensity centred at 3420 cm^{-1}. Additional bands occur at *1102*, 1025, *919,*

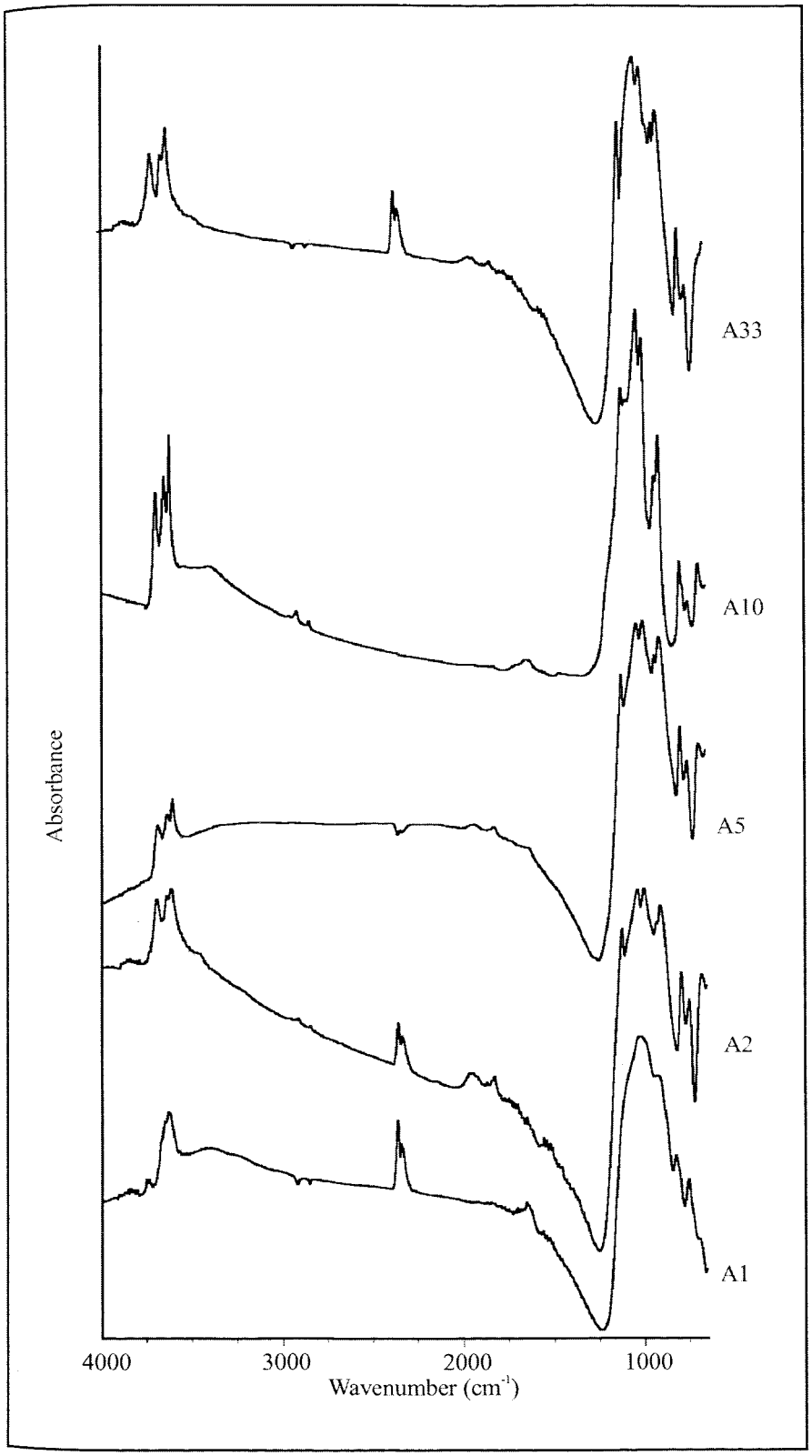

FIGURE 4.8. Stacked infrared spectra of the samples collected during the traverse outlined on Figure 4.6.

828, *807* 756, 693 and 678 cm^{-1} (Fig. 4.9). Numbers in Italics represent shoulders on the spectrum.

Table 4.4. Principle vibrational frequencies of the bands evident on each of the spectra illustrated on Figure 4.8.

sample																
A1		3628			3420		1102	1035	919	828	807	756	693	678		
A2	3703	3655	3620		3476		1122	1037	1002	933	913	795	753	685		
A5	3699	3646	3619				1119	1033	998	935	909	792	752	689		
A7	3701	3648	3619	3622			1119	1052	999	925	910	794	754	692		
A10	3703	3652	3649	3623	3471	3381	1121	1036	1000	934	913	795	754	691		
A13	3694	3653	3645	3621	3389		1118	1034	1006	937	917	797	781	754	689	671
A16	3702	3648	2654	3618			1116	1035	1002	935	909	792	764			
A33	3706	3650	3619				1119	1037	1001	936	910	792	751			

Although the frequency of the intense band at 3628 cm^{-1} overlaps the vibrations of inner OH groups in kaolinite, the lack of any additional bands, suggests that the dominant OH stretching vibrations may be representative of illite or a montmorillonite group mineral (Farmer, 1974b; Russell and Fraser, 1994). Illite is characterised by a sharp band at 3622 cm^{-1} accompanied by a broad, water-like absorption centred at approximately 3440cm^{-1} (Russell and Fraser, 1994). A doublet at 825, 750 cm^{-1} has been cited as diagnostic vibrations indicative of the illite structure, although complexities in the observed spectra make illite difficult to identify using infrared spectroscopy (Russell and Fraser, 1994). In the montmorillonite crystal structure both tetrahedral (Al, and occasionally Fe^{3+}, for Si) and octahedral (Fe^{3+} and Mg for Al) isomorphous substitutions are possible (Russell and Fraser, 1994). Because of these substitutions, considerable broadening of infrared bands due to structural imperfections in the crystal lattice is observed in the OH stretching region of the spectrum (Fig. 4.9). The vibration at 3628 cm^{-1} may be indicative of low-iron montmorillonite, which typically shows a broad stretching band at 3622cm^{-1} (Russell and Fraser, 1994). Alternatively, although the primary OH stretch, assigned to Si-OH groups created by the breaking of Si-O-$Al^{[IV]}$ bonds (Schutz et al., 1987) is found at 3661 cm^{-1} in pure beidellite, beidellite intermixed with montmorillonite generates an absorbance at 3632 cm^{-1}.

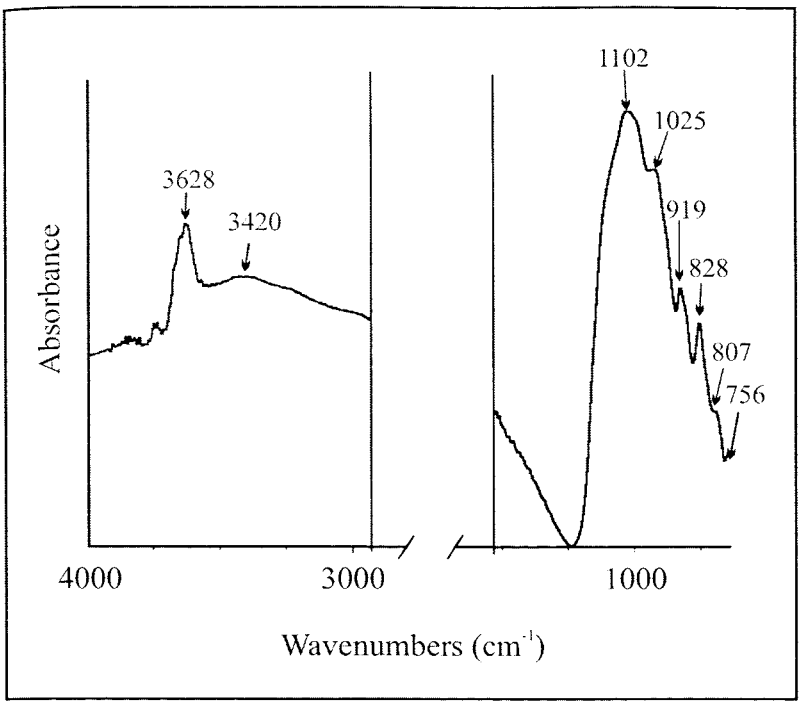

FIGURE 4.9. Infrared spectrum of sample A1

The broad band absorption centred at 3420 cm^{-1} closely resembles that of liquid water (Aines and Rossman, 1984) although vibrations associated with Si-O-Al linkages may provide an alternative explanation (Kloprogge and Frost, 1999).

In the region associated with cation vibrations, bands are observed at 1102, 1025, 919 and 828 cm^{-1}. The strong band at 1103 cm^{-1} may be indicative of silica in the sample. The intense band at 1030 cm^{-1} may be associated with the fundamental Si-O stretching frequencies of all montmorillonite structures (Russell and Fraser, 1994). Characteristic montmorillonite bands occur at 920 (AlAlOH) and 840 cm^{-1} (AlMgOH) (Russell and Fraser, 1994) whereas beidellite substitution, which involves incorporation of Al for Si in the tetrahedral sheet, gives rise to two characteristic bands at 818 and 770 cm^{-1} (Farmer, 1974b). OH deformation bands of beidellite containing some montmorillonite lie at 890 and 845 cm^{-1}.

Samples from the silicified zone

Figure 4.10 shows the infrared spectrum obtained following analysis of sample A2 (Fig. 4.7). Absorbance bands generated are typical of those produced by all samples taken from inside the silicified zone of the orebody (Table 4.4). A2 clearly shows sharp OH vibrations at 3703, 3655 and 3620 cm^{-1}, accompanied by additional bands at 1122, 1037, 1002, 933, 913, 795, 753, and 685 cm^{-1}. Bands at 3700 cm^{-1}, which lies at a distinct frequency compared to bands generated by most other minerals, and 3620 cm^{-1} are characteristic of the kaolin group of minerals.

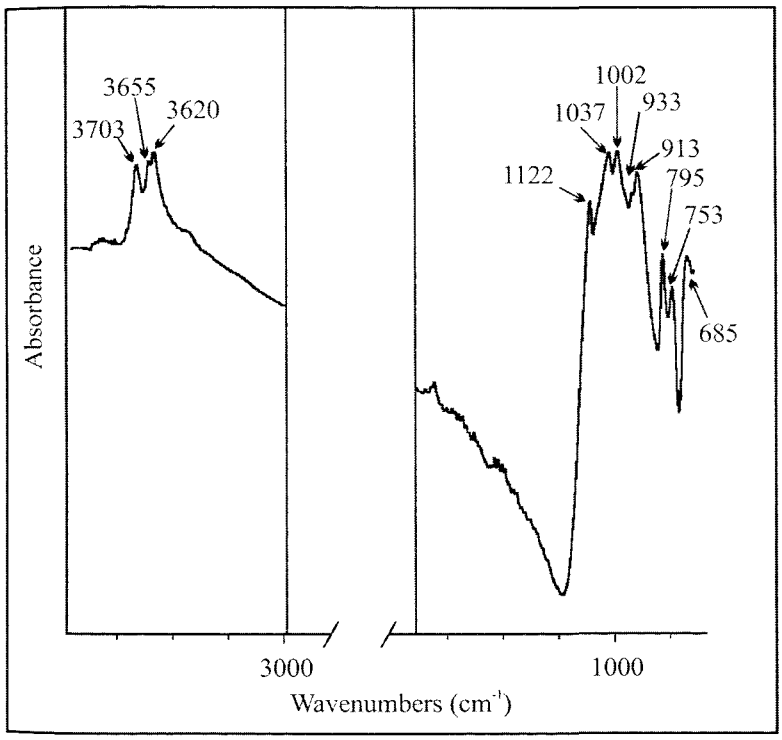

FIGURE 4.10. Infrared absorbance spectrum of sample A2.

On the sample spectrum, sharp OH vibrations at 3703, 3655 and 3620 cm^{-1} are generated by hydroxyl groups constituting one side of the kaolin sheet (Farmer, 1974b; Russell and Fraser, 1994). Although, the infrared spectrum of well-crystallised kaolinite presents four OH stretching bands (Rouxhet et al., 1977), increasing disorder in the structure leaves bands at 3620 and 3700 cm^{-1} unchanged while those at 3669 and 3652 cm^{-1} are replaced by a single band at 3653 cm^{-1} (Russell and Fraser, 1994). This vibration at 3653 cm^{-1} is associated with a hydroxyl group lies close to the plane of the sheet (Rouxhet et al., 1977). OH groups lying

nearly perpendicular to the sheet, give rise to the in phase vibrations responsible for the absorptions at 3700 (Prost et al., 1989). Deuteration of intercalated kaolinite has shown that the band at 3625-3620 cm^{-1} is generated by inner hydroxyl groups located inside the sheet (Ledoux and White, 1974). The band at 3476 has been described previously in synthetic kaolinites (Petit and Decarreau, 1990), disordered kaolinites and iron-rich kaolinites (Delineau et al., 1994), but has not yet been accurately assigned. A weak inflexion observed in the spectrum for in some analysis of sample A2 at 3600 cm^{-1} arises from OH stretching vibrations of $AlFe^{3+}OH$ groups resulting from Fe^{3+} substitution for Al in the octahedral sheet of the kaolinite structure (Petit and Decarreau, 1990).

Discrimination between the kaolin minerals can be made using the stretching vibrations between 3000 and 4000 cm^{-1} (Kodama and Oinuma, 1963). Identification of the particular kaolin in the sample is suggested by the additional OH stretch at 3655 cm^{-1}. This band, coupled with the similar intensity of the doublet at 1037 and 1002, might be used to suggest that halloysite is the kaolin mineral (Russell and Fraser, 1994). Vibrations at 953 cm^{-1} and 913 cm^{-1} are associated with in-plane bending vibrations of surface and inner hydroxyl groups of halloysite respectively (Wada, 1967).

Spectra of all members of the kaolin group show strong, characteristic bands between 1200-250 cm^{-1}, although significant variation between the absorptions generated between 1150 and 1100cm^{-1} may be produced by variation in the degree of crystallinity, particle size and shape (Rendon and Serna, 1981). A measure of the degree of crystallinity in kaolinite may be made using the two bands at 753 and 795 cm^{-1} (Russell and Fraser, 1994). The two bands are of equal intensity in well-crystallised kaolinite, whereas in reduced order halloysite the band at 795 cm^{-1} is reduced to a weak inflection. In accordance with the observations made in the OH stretching region of the spectrum, the relative intensity of the bands observed on Figure 8.8 suggests poorly ordered kaolinite. Vibrations at 755 and 701 cm^{-1} are probably associated with the inner hydroxyl layer (Farmer, 1974b). Bands at 938 and 916 cm^{-1} are attributed to deformation of OH molecules of the inner and inner-surface groups of the kaolinite structure respectively (Ledoux and White, 1974).

Other samples from the silicified zone

All samples from within the silicified zone yield comparable infrared spectra (Table 4.4). A10 shows a similar a spectrum to that of that generated by sample A2, but with the notable addition of weaker bands at 3471 and 3381 cm^{-1} (Fig 4.8, Table 4.4). The frequency of fundamental OH stretching vibrations is intimately associated with the length of the bond linking the molecule. Bands at 3471 and 3381 lie towards the low frequency end of the spectrum of vibrations associated with clay minerals. The frequencies of the absorptions at 3471 and 3381cm^{-1} represent OH vibrations associated with short hydrogen bonds located in structurally ordered locations. Such vibrations at these frequencies are commonly generated following the substitution of defect Al and Li for Si in the quartz crystal lattice. Accordingly, the bands at 3381 and 3471 are attributed to silica in the sample. A broad band at 3500cm^{-1}, indicative of OH stretching vibrations of water located at the interlayer space (Yariv and Shoval, 1976), might suggest that samples are predominantly composed of dehydrated halloysite (Mendelovici and Sagarzazu, 1985).

In addition to those observed in sample A10, bands at 935 cm^{-1} in A5, 937 cm^{-1} in A13 and at 936 cm^{-1} in sample A33 are also observed (Table 4.4). Precise speciation of the absorption at 934 cm^{-1} remains problematical although an absorbance associated with Al-OH-Al defect in dickite centred at 935 cm^{-1} (Russell and Fraser, 1994) and 940cm^{-1} (Mendelovici et al., 1979) may be responsible.

4.3.3.2 Comparison with XRD

XRD investigations of the clay separates analysed using infrared spectroscopy were conducted to provide an alternative identification of the mineral assemblages present. In accordance with the patterns of alteration mineralogy elucidated by micro-FTIR investigation, two distinct types of alteration assemblage are encountered during the sampling traverse (Fig. 4.11).

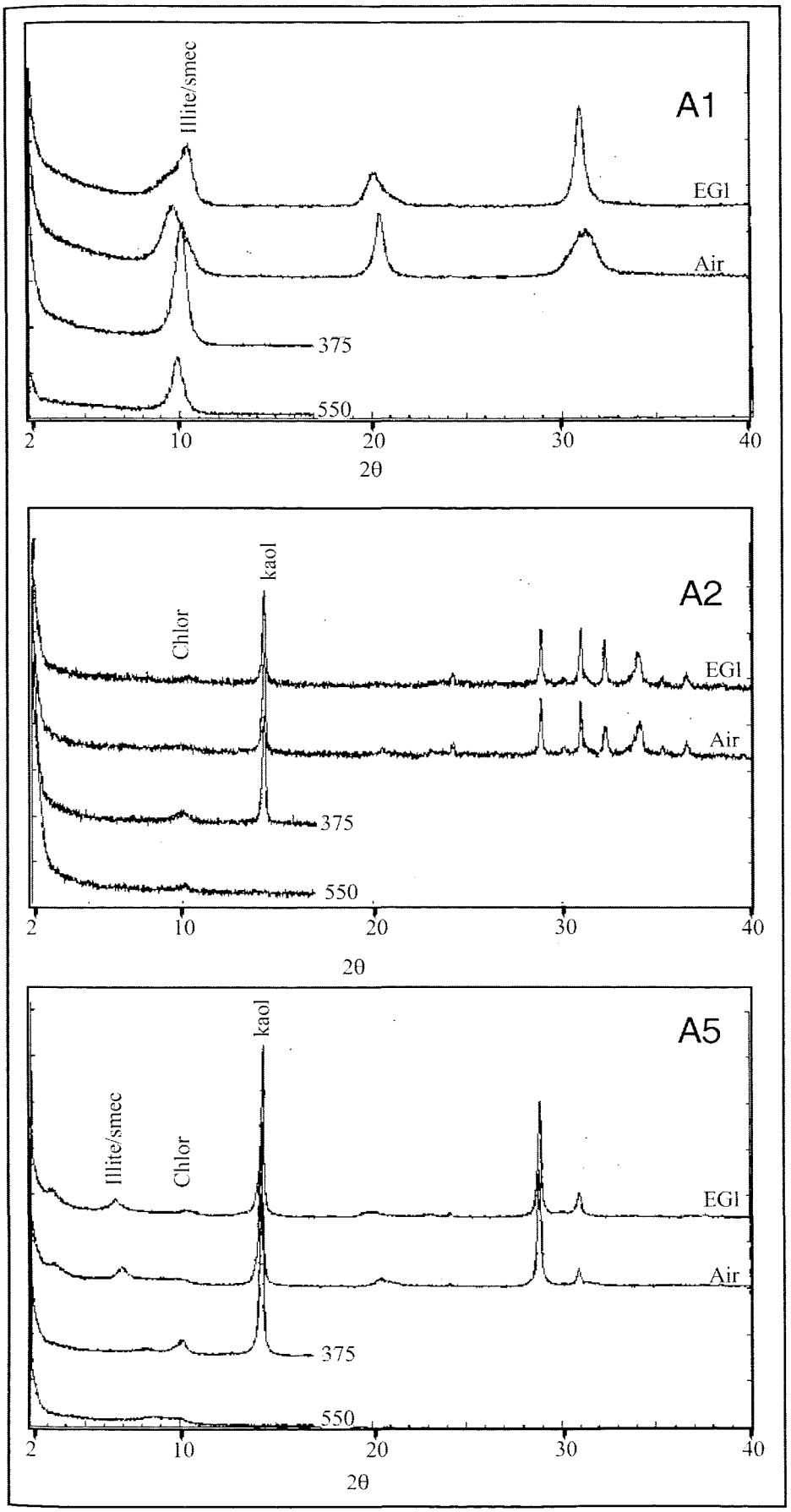

FIGURE 4.11. X-ray patterns of ground samples from Chelopetch. Shown are the results of ethylene glycol solvation followed by heating at 350 and 550°C.

XRD analysis shows interstratified illite/smectite to be the dominant clay mineral in sample A1 from the non-silicified region of the orebody (Fig. 4.11). Mineral assemblages in the silicified zone typically contain dominantly kaolinite. A mior peak at 6. although minor quantities of chlorite and smectite are also identified in some of the samples (Fig. 4.10). The non-identification of chlorite using infrared spectroscopic techniques has been previously reported and it has been suggested that infrared spectroscopy is not as sensitive as XRD to trace or minor amounts of chlorite (Yang et al., 2001). Although XRD analysis identified the presence of smectite, comparable diffraction patterns does not allow discrimination between individual di-octahedral smectites. However, the sensitivity of infrared analysis to differential Al-contents of minerals enabled the characterisation of the dioctahedral smectite species in the sample. Thus smecties of both high (probably beidellite) and low (montmorillonite) Al varieties are found intermixed in sample A1. Using infrared spectroscopy, kaolin group minerals can be identified in a sample at concentrations >10%. It has been previously suggested that quartz, gibbsite kaolinite and halloysite have all been recognised by the infrared spectrum where their presence was uncertain from XRD (Farmer, 1974a).

4.3.4 Discussion of mineral assemblages

The mineralogy of sample A1, from outside the main silicified zone, is dominated by smectites, probable montmorillonite or beidellite. Beidellite represents the Al for Si tetrahedrally substituted end member of the dioctahedral smectite whereas montmorillonite represents the Mg for Al octahedrally substituted end member (Brindley, 1980). On the basis of field observations it has been suggested that beidellite forms, via allophane, as a result of extreme alteration of precursor minerals (Patrier et al., 1998). Beidellite has been interpreted to crystallise under conditions of high fluid flows, under alkaline conditions at temperatures slightly higher than those necessary for the crystallisation of montmorillonite which also forms under lower discharge regimes (Patrier et al., 1998).

Poorly crystalline kaolinite has been previously described associated with the Broadlands-Ohaaki geothermal system, New Zealand, where it crystallises in response to cool, acidic groundwaters have percolated downwards or where CO_2 rich waters dominate (Yang et al., 2001). The dominance of kaolinite in the silicified region of the orebody suggests that gold distribution was intimately controlled by silica-rich, acidic, hydrothermal fluids. Further

characterisation of the hydrothermal events experienced at Chelopech require a significantly more detailed study.

4.4 Summary

The identification of hydrothermal minerals is of great importance to mineral exploration. Until recently, accurate mineral identification has only been possible under laboratory conditions. This study demonstrates the suitability of infrared spectroscopy in determining clay composition using infrared spectroscopy. The spectral analysis indicates the locations of alteration and mineralisation zones at Chelopech, as confirmed by XRD analysis. Mineral spectra obtained by micro-FTIR using traditional time consuming and intricate laboratory sample preparation techniques are similar to those generated using simple, less sophisticated sample preparation methods. However, the identification of minerals using infrared spectroscopy remains far from simple. It is worth noting that although important compilations of mineral spectra are increasing in quantity, incorrect mineral identification or impurities within samples has resulted in numerous cases of misidentification of mineral species (Farmer, 1974b). Despite this, infrared spectroscopy is an exciting new technique in identifying hydrothermal minerals. The potential of micro-FTIR as a rapid, field-based analytical technique will rely heavily on the composition of the alteration assemblage. Samples primarily composed of minerals containing fundamental bands in discrete parts of the infrared spectrum may be readily identified using infrared spectroscopy. Problems may arise where a sample is composed of several minerals which generate absorptions in the same spectral region. Attempting to differentiate between minerals which, due to similar structural and chemical characteristics, show characteristic absorptions in the same regions of the infrared spectrum may require more complex, laboratory-based analysis. A major limitation of infrared spectroscopy is that interstratified minerals may not be distinguished from a mineral mixture.

Infrared spectroscopy is probably holds greatest potential as a technique to characterise between individual members of a mineral species, for example the kaolins, and ultimately, because the sensitivity of infrared spectroscopy in identifying components in a mineral mixture is often very different from other techniques, mineral identification using infrared spectroscopy compliments existing methods of mineral analysis. Further studies

characterising alteration mineralogy using coupled micro-FTIR and PIMA spectroscopic techniques are needed to elucidate potential advantages of the increased resolution afforded by the former.

Chapter 5

THE MORENCI PORPHYRY COPPER DISTRICT

5 The Morenci Porphyry Copper District

5.1 INTRODUCTION

The Younger Granodiorite Porphyry is an intrusion associated with the Morenci Porphyry Copper Deposit Arizona. Chapters 6, 7 and 8 of this thesis report on studies performed on quartz phenocrysts, and mineral phases found within them, taken from this intrusion. This chapter aims to, 1) present a brief overview of the geology of the Morenci porphyry copper region, and, 2) provide details of the petrography of the intrusion from which the samples were taken.

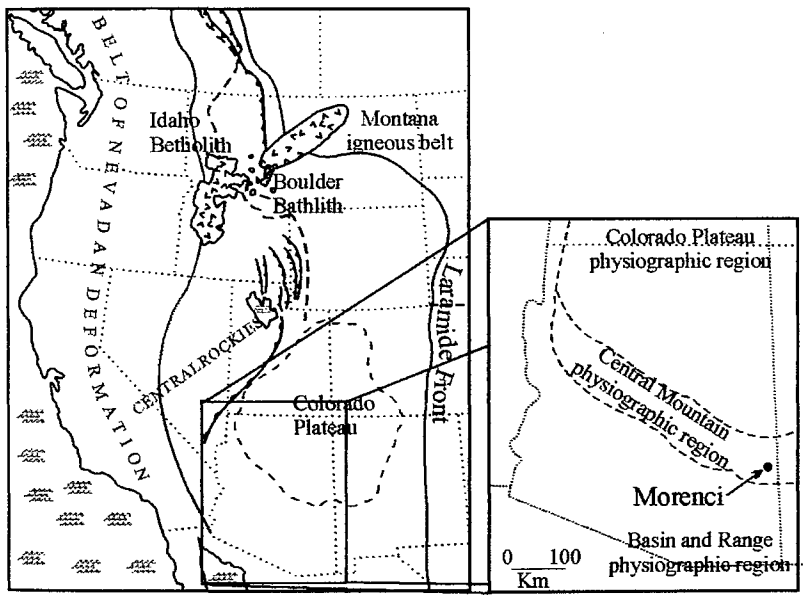

FIGURE 5.1. Location map of the, Morenci district related to the main tectonic regions and the Laramide orogenic front.

5 The Morenci Porphyry Copper District

5.1 INTRODUCTION

The Younger Granodiorite Porphyry is an intrusion associated with the Morenci Porphyry Copper Deposit Arizona. Chapters 6, 7 and 8 of this thesis report on studies performed on quartz phenocrysts, and mineral phases found within them, taken from this intrusion. This chapter aims to, 1) present a brief overview of the geology of the Morenci porphyry copper region, and, 2) provide details of the petrography of the intrusion from which the samples were taken.

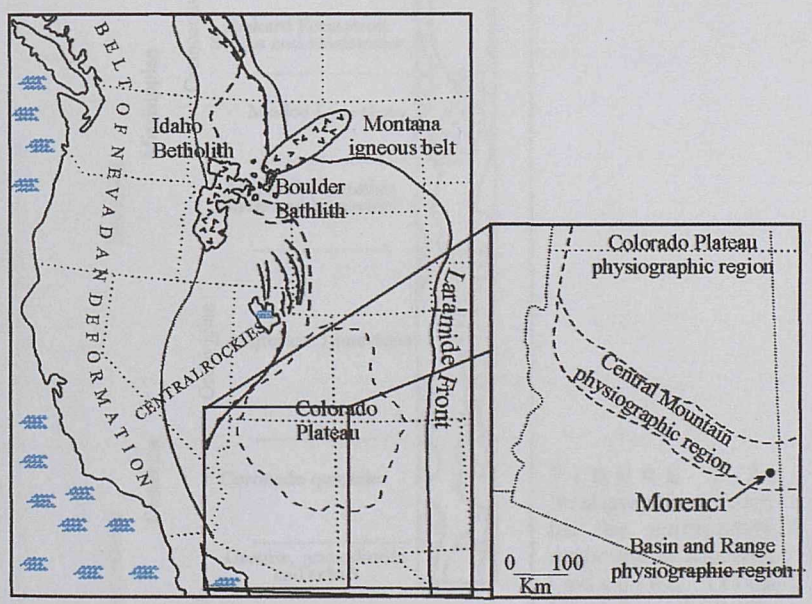

FIGURE 5.1. Location map of the, Morenci district related to the main tectonic regions and the Laramide orogenic front.

5.2 GEOLOGICAL SETTING OF THE MORENCI REGION:

The Morenci mining district lies within the Central Mountain Province, Arizona, between the Colorado Plateau and the Basin and Ranges Provinces (Fig. 5.1). Located on what was once an Upper Cretaceous continental shelf, the region is underlain by steeply dipping Precambrian Penal schists, quartzite, and a coarse-grained, basement granite. Morenci was discovered in 1865 and rapidly became the primary copper-producing deposit in Arizona. It is currently one of the largest porphyry copper deposits in North America.

5.2.1 General Geology

In the Morenci region a 300 m thick sedimentary sequence of Paleozoic quartzites, limestones and shales rests unconformably upon a Proterozoic crystalline basement (Fig. 5.2).

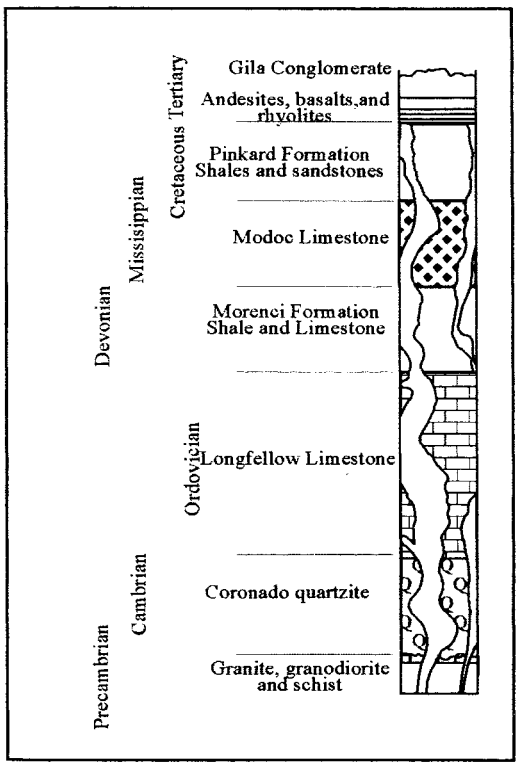

FIGURE 5.2. Stratigraphic column for the sedimentary sequence at Morenci (adapted from Moolick and Durek, 1966).

The Precambrian basement consists of schists, granites and granodiorite. Limestones, typically argillaceous with siliceous or shaly horizons, compose most of the uninterrupted Paleozoic and Mesozoic section, which is terminated by a Cretaceous, brachiopod bearing

marine shale. The entire region is encircled by basaltic, andesitic and rhyolitic Tertiary volcanic flows and intrusive pipes.

Following the intrusion of the Precambrian granite-granodiorite complex, no igneous activity is evident until the emplacement of the Laramide intrusive complex (51-62 Ma.). Measuring 10km along strike by 4km wide (Moolick and Durek, 1966), the Cretaceous-Tertiary Laramide intrusive is manifested by numerous stocks, laccoliths and associated dykes which are almost entirely porphyritic in texture. Three distinct stages of progressively silica-rich intrusions, from oldest to youngest; diorite to quartz monzonite to granite, are found (Fig. 5.3).

Much of the central part of the intrusive suite consists of several intrusions of granite-granodiorite porphyry, which is the principle ore-bearing rock. The stock-like Quartz Monazite porphyry consists of small, closely packed phenocrysts of orthoclase, albite and oligioclase in a microcrystalline quartz-feldspar groundmass. Small quartz phenocrysts are occasionally evident but quartz is generally restricted to the groundmass. Once abundant biotite is rarely preserved.

The ore and associated alteration minerals at Morenci are generally localised in, and adjacent to, the quartz-monzonite porphyry intrusive. Ore-grade copper mineralisation in the stock and surrounding host rocks consists largely of small veinlets and disseminations of pyrite, chalcopyrite, molybdenite, sphalerite, rare galena, gold and silver. Supergene enrichment is confined to pyritic veins and non-carbonate rocks in the region.

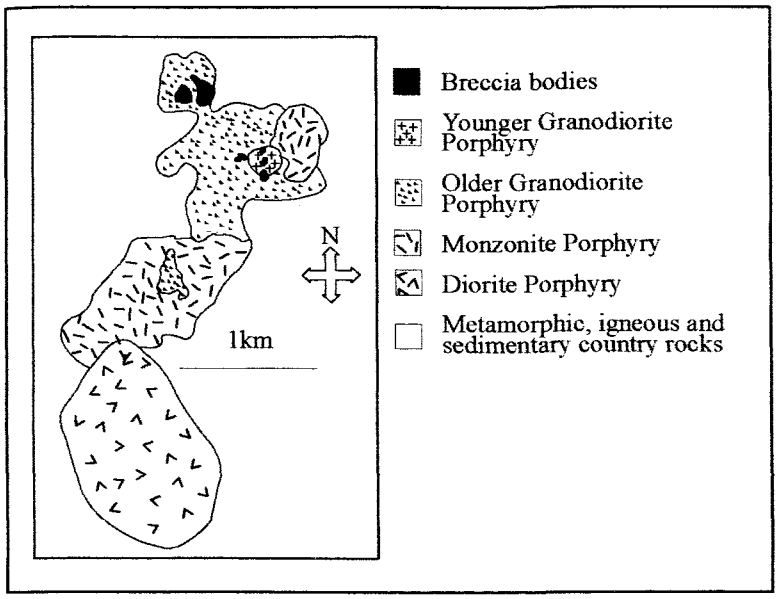

FIGURE 5.3. Geological map of the Morenci Porphyry copper deposit and the distribution of intrusive rocks (adapted from Armstrong, 1999, unpubl. PhD thesis. Univ. of Southampton).

5.2.2 Alteration

Hydrothermal alteration in the Precambrian and Laramide igneous complexes is characterised by a potassic core telescoped by a pyritic-phyllic zone, which is enveloped by widespread propylitic alteration. At least three separate stages of hypogene alteration and mineralisation can be recognised (Langton, 1971). Alteration is dominantly hypogene phyllic and supergene argillic, the former dominant in the east side of the mine, the latter to the west (Moolick and Durek, 1966)). All of the ore currently mined is supergene in origin.

In general, the rocks were altered to calc-silicates or pelitic hornfels and skarn of the amphibolite facies (Moolick and Durek, 1966). The mineral assemblage generally consists of dipside, epidote, garnet, and tremolite accompanied by localised actinolite, chlorite, idocrase, magnetite, specularite, serpentinite and talc. High-temperature contact minerals such as wollastonite and the aluminium silicates are absent. Scarn is typically developed in calcareous sediments adjacent to porphyries.

5.2.3 Mineralisation

The intensely mineralised region is situated at a major regional tectonic intersection and the framework of currently minable orebodies may be attributed directly to those rejuvenated Precambrian faults (Langton, 1971). Mineralisation is predominantly hosted in the porphyritic Laramide stocks, laccoliths and associated dykes. Four principal vein types have

been identified. These are, from oldest to youngest, potassium feldspar + quartz, quartz + molybdenite, quartz + pyrite ± chalcopyrite, and quartz + chalcopyrite ± pyrite. Primary fluid inclusions in all four vein types include; vapour only, liquid + vapour, liquid + vapour + halite, and liquid + vapour + halite + hematite (with chalcopyrite, and sylvite in some instances) (Holick and Wood, 1999). Fluid inclusions from the quartz + pyrite +/- chalcopyrite, quartz + chalcopyrite ± pyrite, and quartz + molybdenite veins had modes for the homogenization temperatures of 325-330°C, 340-345°C and 335-360°C, respectively (Holick and Wood, 1999). Fluid inclusion salinities showed two distinct populations of inclusions. A low-salinity group with 3-12 wt % NaCl eq., and a high-salinity group with 33-50 wt % NaCl eq (Holick and Wood, 1999).

5.3 THE YOUNGER GRANODIORITE PORPHYRY

Samples analysed in Chapters Six, Seven, and Eight were extracted from the Younger Granodiorite Porphyry (YGD) (Fig. 5.3). Individual phenocrysts of dipyramidal quartz, measuring between 0.1 and 12 mm in diameter, and lesser amounts of altered relict K-feldspar and plagioclase measuring between 0.25 and 10 mm, accompanied by an extremely altered Fe-Mg, phase give the intrusion a distinct porphyritic texture. Original feldspar compositions are difficult to ascertain due to extensive overprinting by the products of hydrothermal alteration. Quartz phenocrysts are commonly zoned with larger crystals exhibiting spherical, anhedral cores surrounded by several euhedral outer zones interpreted to represent cyclic oscillatory zoning (Armstrong, 1999). The fine-grained matrix has undergone intense alteration with extensive development of sericite and secondary quartz. Occasional epidote, magnetite and chlorite are also observed. The rock has been penetrated by patchy Fe-staining caused by very fine crystal boundary controlled Fe-oxide smear. No sulphides are found in the sample.

Apatite, biotite and zircon micro-phenocrysts, studied in Chapter eight, are found included within the cores of quartz phenocrysts along regions delineated by narrow bands of co-existing, primary hypersaline and vapour rich inclusions and primary melt inclusions. Euhedral apatite and zircon needles, commonly measure ~10-15μm in length. Larger, light brown, biotite micro-phenocrysts measure up to 100μm.

Melt inclusion analysis suggested the original melt contained 60-67 wt% SiO_2, between 1 and 6.5wt% H_2O and a Cl concentration of approximately ~6920 ppm. Additionally, a Cl/H_2O ratio of 0.1-0.2 was calculated. Difficulties in determining F and S contents resulted in most of the analyses falling below the detection limit for the element by EMPA (Armstrong, 1999. unpubl. PhD thesis. Uni. of Southampton).

Chapter 6

CATHODOLUMINESCENCE ELUCIDATION OF GROWTH ZONATION IN QUARTZ PHENOCRYSTS: EVIDENCE OF MAGMATIC SYSTEM EVOLUTION?

6 Cathodoluminescence elucidation of growth zonation in quartz phenocrysts: Evidence of magmatic system evolution?

6.1 Introduction

Processes in subvolcanic magma chambers play a significant role, not only in producing the spectrum of igneous rock compositions found on Earth (McBirney, 1993), but also in the development of numerous types of magmatic-related ore deposits (Candela, 1997). As an intrusion cools, crystallisation and convection of the magma, crystal fractionation or retention in residual melt, chamber-wide stratification, chemical mixing, degassing, and eventually eruption all place fundamental constraints on the make-up of the final product (Bacon, 1986; Bacon *et al.*, 1989; Cashman, 1992; Druitt and Bacon, 1989; Eichelberger, 1978; Rutherford and Hill, 1993). Despite theoretical and experimental studies on such magmatic processes (Sparks *et al.*, 1993; Sparks *et al.*, 1984; Sparks and Marshall, 1986), extracting unambiguous information about the crystallisation history of natural magmas has proved difficult (Marsh, 1990; Marsh, 1991; Sparks, 1990).

Zoned mineral phenocrysts have long been recognized to record evidence of variations in the physiochemical parameters of the system in which the mineral grew (Bowen, 1928; Emmons, 1952; Harloff, 1927; Hills, 1936). In recent years textural relationships between mineral phases in ore-related rocks have been extensively studied (Candela, 1997; Candela and Blevin, 1995). Gradual or sudden changes in the state of equilibrium associated with the migration, cooling and extrusion of melts can be preserved as discrete textural or geochemical zones in a crystal (Allegre *et al.*, 1981; Anderson, 1984; Haase *et al.*, 1980; L'Heureux and Fowler, 1994; Ortoleva, 1990; Pearce and Kolisnik, 1990; Shimizu, 1990). The analysis of mineral zonation in explosively erupted, zoned feldspar phenocrysts has contributed significantly to our understanding of pre-eruption magma chamber dynamics (Anderson, 1984; Hattori and Sato, 1996; Singer *et al.*, 1995). A similar, detailed understanding of magmatic crystallisation history would prove invaluable to workers attempting to establish the

magmatic dynamics of intrusions associated with porphyry copper deposits. Unfortunately, this is frequently impossible due to intense hydrothermal alteration.

Quartz phenocrysts, which remain relatively unaffected by subsequent hydrothermal alteration (Roedder, 1984), are a common feature of many shallow emplaced, subvolcanic rocks (Deer *et al.*, 1992) and have been frequently reported in intrusions associated with numerous porphyry systems (Armstrong, unpub. PhD thesis, Univ. Southampton, 1999). In large volume magmas, quartz phenocrysts may be primary magmatic crystals, xenocrysts from wallrocks or other magmas entrained during magma ascent or metamorphic restite from the magma source region (Watt *et al.*, 1997). Primary magmatic phenocrysts might themselves be derived from the crystalline walls of the magma (Nakada *et al.*, 1994) or from remobilised crystal mush (Lipman *et al.*, 1997; Mahood, 1990). A quantitative model for evaluating the cooling history of granitic magmas based on quartz morphologies suggested that examination of quartz textures provides reliable information about the thermodynamic history of a melt (MacLellan and Trembath, 1991). This suggests that, unlike compositional variations in feldspar, which record a complex response to both chemical and physical variations during cooling, specific quartz morphologiess crystallise uniquely as a function of cooling rate. Unfortunately, internal heterogeneities in quartz frequently remain undetected and, due to its low tolerance for impurities, chemical zoning is rarely documented (Rovetta *et al.*, 1989). Additionally, where reported, the infrequency and obscurity of textural heterogeneities observed in quartz commonly leads to ambiguous conclusions concerning the relationship of individual features to crystal growth (Peppard *et al.*, 2001).

Cathodoluminescence is the emission of electromagnetic radiation from a material when excited by an electron beam. The cause of cathodoluminescence in quartz remains controversial, but specific emissions are well know to result from substitutional and interstitial incorporation of trace elements from different types of intrinsic and extrinsic defect centres in the quartz (Ramseyer and Mullis, 1990).

Previously, cathodoluminescence has been successfully applied to the study of pressure solution, cementation, and provenance studies in sandstone (Demars *et al.*, 1996; Dickinson and Millikinen, 1995; Hogg *et al.,* 1992; Millikinen, 1994; Owen and Carozzi, 1986; Seyedolali *et al.,* 1997; Sippel, 1968; Zinkernagel, 1978) and hydrothermal vein formation (Pennison-Dorland, 2001). It has also been correlated with oxygen isotope measurements to determine the fractionation of isotopes during crystal growth (Onasch and Vennemann, 1995) and the flow of hydrothermal fluids from an igneous body (Valley and Graham, 1996). Despite this, studies detailing quartz zonation in granitic rocks remain few. Recently, the description of growth zones within otherwise homogeneous igneous quartz crystals has been made (D'Lemos *et al.*, 1997; Watt *et al.,* 1997). In this study cathodoluminescence imaging techniques were applied to quartz phenocrysts from the Morenci Porphyry copper deposit, Arizona. Images presented here show that zoning in quartz phenocrysts may yield a previously unrecorded internal growth patterns. Comparisons with feldspar morphologies, made in the light of these findings, enable a detailed record of the evolution of phenocryst growth to be constructed.

6.2 METHODS

The scanned cathodoluminescence technique used in this study records the light emitted from a sample using a photomultiplier. Scanned cathodoluminescence images collected on the SEM produce a panchromatic black and white image that captures the relative intensities of the cathodoluminescence emissions. Although the technique does not provide quantitative information on the light intensity or the wavelength of the radiation generated, scanned cathodoluminescence images do show a wealth of textural information detailing the growth history of the sample (Pennison-Dorland, 2001).

Phenocrysts were separated from the groundmass through a process of coarse crushing, and individual quartz grains separated by hand. Crystals were then mounted in resin, perpendicular to the optical *c*-axis, and prepared as standard 200μm-thick, double polished thin sections. Samples were carbon coated prior to cathodoluminescence analysis. Scanned cathodoluminescence images were collected using a K.E. Developments cathodoluminescence detector mounted on a Hitachi S2500 scanning electron microscope. A typical accelerating potential of 20kV was used with a 20*n*A gun current velocity.

6.3 Results and Discussion

6.3.1 Quartz Morphologies

Quartz phenocrysts from Morenci are of euhedral to subhedral habit suggesting initial quartz growth early in the evolution of the system (Watt *et al.*, 1997). Phenocrysts vary between 0.1 and 12mm in diameter across the widest part of the *c*-axis. Large variation in grain size may be attributable to quartz crystallisation on relict grains or rapid, dynamic crystallisation during fluid-assisted grain growth (Channer and Spooner, 1991; Graupner *et al.*, 2000). Co-joining crystals are frequently observed in the sample suggesting crystallisation in a crystal-rich enviroment.

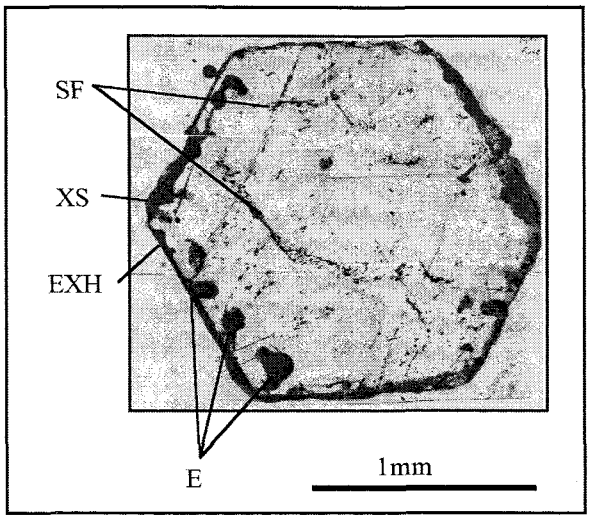

Figure 6.1 . Photomicrograph of a quartz phenocryst sectioned perpendicular to the - *c* crystallographic axis. EXH = euhedral crystal habit, XS = crystal surface, SF = secondary microfractures containing lines of fluid inclusions, E = embayed crystal faces.

Dark, curved embayments are found intermittently along the external crystal faces, intruding into the crystal (Fig. 6.1). Embayments in crystals may form following; 1) unstable growth under supersaturated conditions (Donaldson, 1976; Lofgren, 1980), 2) resorption of an originally euhedral crystal (Donaldson and Henderson, 1988; Harris and Anderson Jr, 1984), or 3) stagnation of growth in the central parts of a crystal (Roedder, 1984; Torgesen and Jackson, 1965). Further identification of the individual process responsible for the generation of embayments requires assessment of the textural features present in that crystal and will be discussed in a later section.

6.3 Results and Discussion

6.3.1 Quartz Morphologies

Quartz phenocrysts from Morenci are of euhedral to subhedral habit suggesting initial quartz growth early in the evolution of the system (Watt *et al.*, 1997). Phenocrysts vary between 0.1 and 12mm in diameter across the widest part of the *c*-axis. Large variation in grain size may be attributable to quartz crystallisation on relict grains or rapid, dynamic crystallisation during fluid-assisted grain growth (Channer and Spooner, 1991; Graupner *et al.*, 2000). Co-joining crystals are frequently observed in the sample suggesting crystallisation in a crystal-rich enviroment.

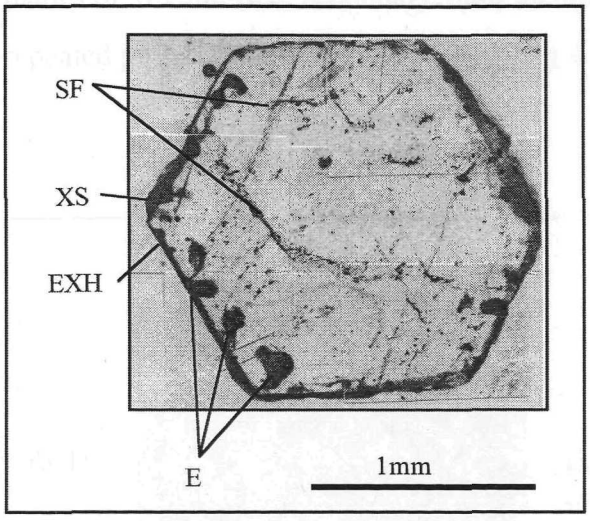

Figure 6.1 . Photomicrograph of a quartz phenocryst sectioned perpendicular to the - *c* crystallographic axis. EXH = euhedral crystal habit, XS = crystal surface, SF = secondary microfractures containing lines of fluid inclusions, E = embayed crystal faces.

Dark, curved embayments are found intermittently along the external crystal faces, intruding into the crystal (Fig. 6.1). Embayments in crystals may form following; 1) unstable growth under supersaturated conditions (Donaldson, 1976; Lofgren, 1980), 2) resorption of an originally euhedral crystal (Donaldson and Henderson, 1988; Harris and Anderson Jr, 1984), or 3) stagnation of growth in the central parts of a crystal (Roedder, 1984; Torgesen and Jackson, 1965). Further identification of the individual process responsible for the generation of embayments requires assessment of the textural features present in that crystal and will be discussed in a later section.

Co-existing, primary hypersaline fluid inclusions, melt inclusions, and biotite, apatite and zircon micro-phenocrysts, are frequently found trapped within the quartz phenocrysts. Growth zones, defined by geometric arrays of fluid inclusions and solid phases oriented parallel to the crystal faces, are evident in some samples (Fig. 6.2). Fluid inclusions in the growth zones may be, 1) oblong with smooth surfaces or, 2) of highly irregular shape. Due to the parallelism of the arrays with the crystal edges, the fluid inclusions are judged to be of primary origin. Up to six such growth zones have been identified in the Morenci quartz phenocrysts (Armstrong, unpub. PhD thesis, Univ. Southampton, 1999). Successive zones of fluid inclusions within the phenocrysts attest to crystallisation in a volatile-saturated early magma. Abundant planes of volatile-rich, secondary fluid inclusions show samples have been subject to repeated post-crystallisation fracturing (Fig 6.2).

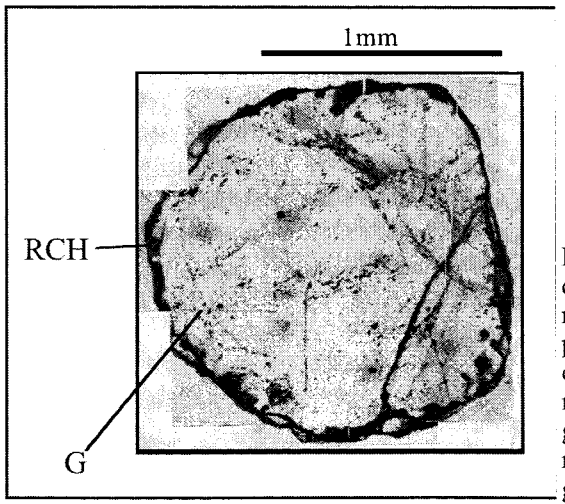

FIGURE 6.2. Photomicrograph of a quartz phenocryst cut perpendicular to the c-crystallographic axis. RCH rounded crystal habit, and G = growth zone defined by primary fluid inclusions. The image, showing the entire cross section of the crystal, demonstrates the relationship between the growth zones, delineated by geometric arrays of solid phases along with fluid and melt inclusions, with the crystal faces. Four such growth zones are evident on the image.

Co-existing, primary hypersaline fluid inclusions, melt inclusions, and biotite, apatite and zircon micro-phenocrysts, are frequently found trapped within the quartz phenocrysts. Growth zones, defined by geometric arrays of fluid inclusions and solid phases oriented parallel to the crystal faces, are evident in some samples (Fig. 6.2). Fluid inclusions in the growth zones may be, 1) oblong with smooth surfaces or, 2) of highly irregular shape. Due to the parallelism of the arrays with the crystal edges, the fluid inclusions are judged to be of primary origin. Up to six such growth zones have been identified in the Morenci quartz phenocrysts (Armstrong, unpub. PhD thesis, Univ. Southampton, 1999). Successive zones of fluid inclusions within the phenocrysts attest to crystallisation in a volatile-saturated early magma. Abundant planes of volatile-rich, secondary fluid inclusions show samples have been subject to repeated post-crystallisation fracturing (Fig 6.2).

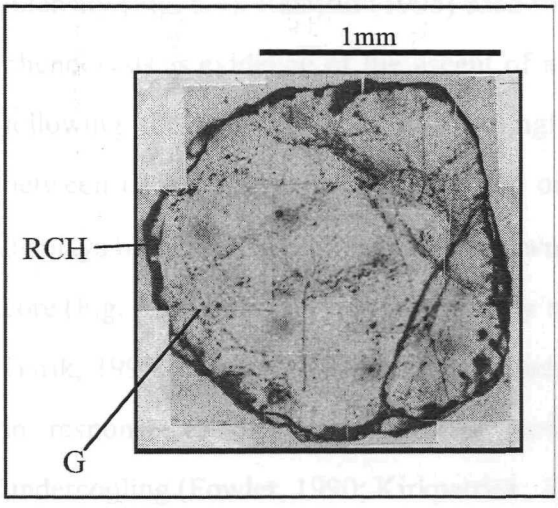

FIGURE 6.2. Photomicrograph of a quartz phenocryst cut perpendicular to the c-crystallographic axis. RCH = rounded crystal habit, and G = growth zone defined by primary fluid inclusions. The image, showing the entire cross section of the crystal, demonstrates the relationship between the growth zones, delineated by geometric arrays of solid phases along with fluid and melt inclusions, with the crystal faces. Four such growth zones are evident on the image.

6.3.2 Cathodoluminescence Petrography

In the scanning SEM cathodoluminescence images, a zone is defined as a region containing a band of contrasting intensity to an adjacent section of the crystal. Cathodoluminescence reveals significant zonation in all of the quartz phenocrysts examined. Zones elucidated in the cathodoluminescence images create a roughly concentric pattern around the central region of the crystal. In accordance with previous cathodoluminescence studies of quartz phenocrysts from other acidic magmas, there are rarely greater than 20 growth zones in any phenocryst (Peppard *et al.*, 2001; Watt *et al.*, 1997). Cathodoluminescence images elucidate two distinct types of growth zonation patterns in the sample phenocrysts:

6.3.2.1 Type I

Type I phenocrysts contain a rounded core of uniform, moderate luminescence intensity (Fig. 6.3). Ratajski (1995) used rounded, relict crystals in the cores of quartz phenocrysts as evidence of the ascent of a vapour-undersaturated melt. Immediately following the rounded core is a strongly luminescent, euhedral zone measuring between 10 and 30μm in thickness. The outer edge of this brightly luminescent zone displays branched, tree-like crystals, grown perpendicular to the faces of the rounded core (Fig. 6.3) which are morphologically similar to mineral dendrites (Ben-Jacob and Garik, 1990; Doherty, 1974). Experimental studies have shown dendrites crystallise in response to diffusion-controlled, cellular crystal growth at high degrees of undercooling (Fowler, 1990; Kirkpatrick, 1981; Swanson and Fenn, 1986). Fluid and silicate melt inclusions are frequently captured along the outer branched edges of this zone. The capture of included phases may arise due to the trapping and adsorption of impurities between the branches. Fluctuation and heterogeneity in the growth rate, changes in nutrient concentration, variations in pH, agitation of fluid and the development of cracks at the crystal surface provide alternative mechanisms (Sisson *et al.*, 1993).

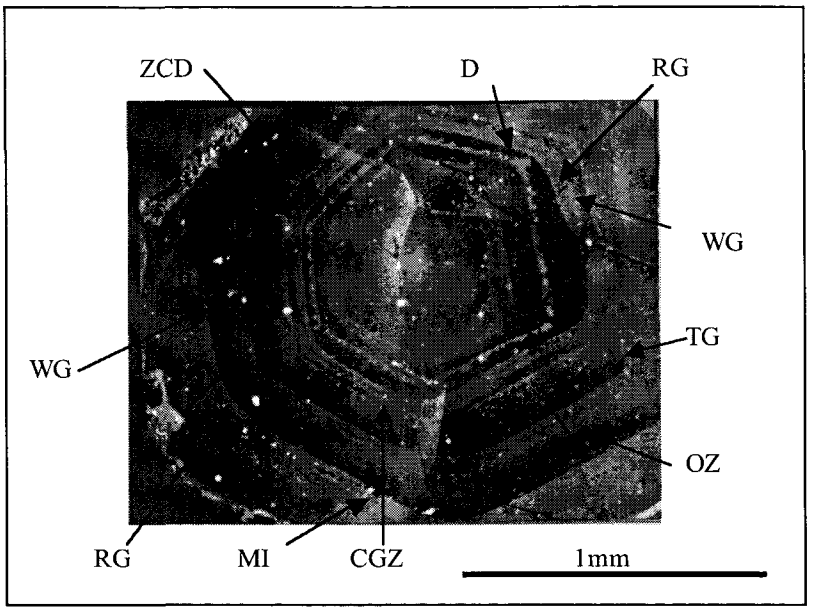

FIGURE 6.3. Scanning SEM cathodoluminescence image of a type 1 quartz phenocryst. Evident on the image is: OZ = oscillatory zoning, D = dendritic zones, WG = wavy growth zones, RC = relict rounded core, ZCD = a zone of constant dark luminescence, MI = included mineral phases, TG = truncated growth zones, R = crystal rounding, CGZ = concentric growth zones. Line of sight of the image is down the optical *c*-axis of the crystal. White specks on the crystal are likely to be traces of corundum left over from the following process.

Generally, a zone of uniform, dark luminescence response immediately follows the dendritic growths. Commonly rounded along its crystal edges, this is succeeded by a series of oscillatory growth zones. The onset of each oscillatory zone is manifested by bright luminescence. Continued crystallisation leads to progressively reduced intensity luminescence response until termination of a sequence by euhedral morphologies, commonly displaying dark luminescence response. The onset of the succeeding zone is heralded by a sharp reversal to a bright cathodoluminescence response. The net result is the development of successive oscillatory growth zones, the evolution of each characterised by a distinctive progressive reduction in luminescence intensity.

Oscillatory zoning resembles chemical zoning in plagioclase, which may be attributable to variations in melt composition, growth conditions, growth rate, and

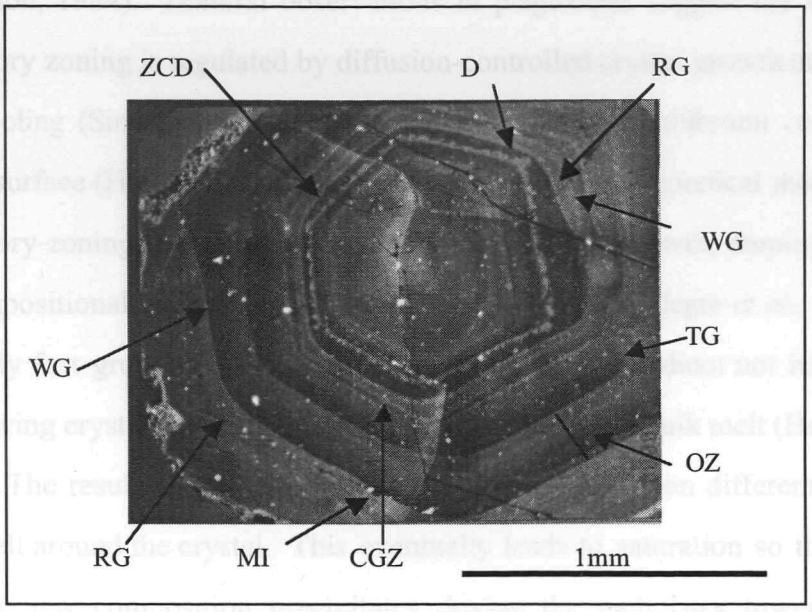

FIGURE 6.3. Scanning SEM cathodoluminescence image of a type 1 quartz phenocryst. Evident on the image is: OZ = oscillatory zoning, D = dendritic zones, WG = wavy growth zones, RC = relict rounded core, ZCD = a zone of constant dark luminescence, MI = included mineral phases, TG = truncated growth zones, R = crystal rounding, CGZ = concentric growth zones. Line of sight of the image is down the optical *c*-axis of the crystal. White specks on the crystal are likely to be traces of corundum left over from the following process.

Generally, a zone of uniform, dark luminescence response immediately follows the dendritic growths. Commonly rounded along its crystal edges, this is succeeded by a series of oscillatory growth zones. The onset of each oscillatory zone is manifested by bright luminescence. Continued crystallisation leads to progressively reduced intensity luminescence response until termination of a sequence by euhedral morphologies, commonly displaying dark luminescence response. The onset of the succeeding zone is heralded by a sharp reversal to a bright cathodoluminescence response. The net result is the development of successive oscillatory growth zones, the evolution of each characterised by a distinctive progressive reduction in luminescence intensity.

Oscillatory zoning resembles chemical zoning in plagioclase, which may be attributable to variations in melt composition, growth conditions, growth rate, and

diffusion controlled chemical changes between the mineral and its environment (Anderson, 1984). Textural observations in plagioclase suggest the development of oscillatory zoning is regulated by diffusion-controlled crystal growth at low degrees of undercooling (Singer *et al.*, 1995) in response to near-equilibrium conditions at the crystal surface (Haase *et al.*, 1980; Sibley *et al.*, 1976). Theoretical modelling suggests oscillatory zoning represents slow to moderate crystal growth, dominantly controlled by compositional changes at the crystal-melt interface (Allegre *et al.*, 1981). During relatively fast growth in a viscous liquid, precipitating medium not incorporated into the growing crystal is not sufficiently homogenised in the bulk melt (Hosaka and Taki, 1981). The result is the build-up of a liquid of composition different to that of the bulk melt around the crystal. This eventually leads to saturation so that a crystalline zone of new composition precipitates driving the melt back towards the original composition where the cycle repeats (Haase *et al.*, 1980).

The frequent parallelism of successive growth zones with quartz phenocryst edges suggests that progressive changes in crystallisation conditions experienced during crystal growth are responsible for the observed oscillatory zoning. However, oscillatory zoning in quartz may arise due to quite different circumstances than necessary for development in plagioclase. Experimental studies suggest that, unlike feldspar, quartz crystallisation remains a function of cooling rate and is unaffected by external factors (MacLellan and Trembath, 1991). Additionally, unlike the equilibrium partitioning of trace elements between growing plagioclase crystal and the precipitating medium, the incorporation of defects into quartz is a kinetic process that does not directly reflect the temperature or pressure of the system (Ihinger and Zink, 2000). Accordingly, if cathodoluminescence response in quartz is attributable to the incorporation of impurity defects in the crystal structure (D'Lemos *et al.*, 1997; Ramseyer *et al.*, 1988; Ramseyer and Mullis, 1990; Sprunt, 1981; Stevens Kalkeff and Phillips, 1995; Stevens Kalkeff *et al.*, 1997; Watt *et al.*, 1997), a model to describe the formation of oscillatory zoning in quartz may need to be formulated around variations in the cooling rate of the system. The fact that oscillatory zoning is more common in

volcanic than plutonic quartz (Watt *et al.*, 1997) provides additional evidence that changes in temperature may control its formation.

The outermost regions of any individual oscillatory growth zone commonly exhibit a dark luminescence response. These regions are generally composed of euhedral to rounded faces, with a small degree of rounding/resorption evident on some of the corners (Fig. 6.3). Rounding may be attributable to resorption of the crystal but recent experimental studies (Laporte, 1994) and geometrical modeling (Elbaum and Wettlaufer, 1993; Wettlaufer *et al.*, 1994) which show that quartz crystallised in equilibrium with the surrounding medium has pyramidal faces that are separated by smoothly curved, convex regions. During crystal growth, if accretion of material onto the growth front is much slower than all available diffusion and relaxation processes the shape of the resulting crystal will represent the equilibrium form of that crystal. Sets of oscillatory zones are usually laterally continuous although may be terminated by homogeneous zones of moderate luminescence (Fig. 6.3). Truncated growth zones may arise under several regimes: 1) dissolution of a crystal in thermal or chemical disequilibrium with the surrounding environment (Kerr, 1995; Watt *et al.*, 1997), 2) rounding and embayment of euhedral morphologies along crystal boundaries during prolonged crystallization (MacLellan and Trembath, 1991), 3) quartz removal following simple mechanical breakage of the crystal during the magmatic process, 4) rapid growth leading to the crystallisation of a laterally incomplete zone (Donaldson and Henderson, 1988).

6.3.2.2 Type II

Cathodoluminescence images of phenocrysts belonging to group II show central parts to be composed of a relict paired crystal (Fig. 6.4). Zones, individually measuring several microns in thickness, commence at, or very near, to the core of the relict paired crystal. Mineral aggregates, represented by paired crystals or mineral intergrowths may be indicative of crystals derived from the crystal-rich walls of the magma chamber.

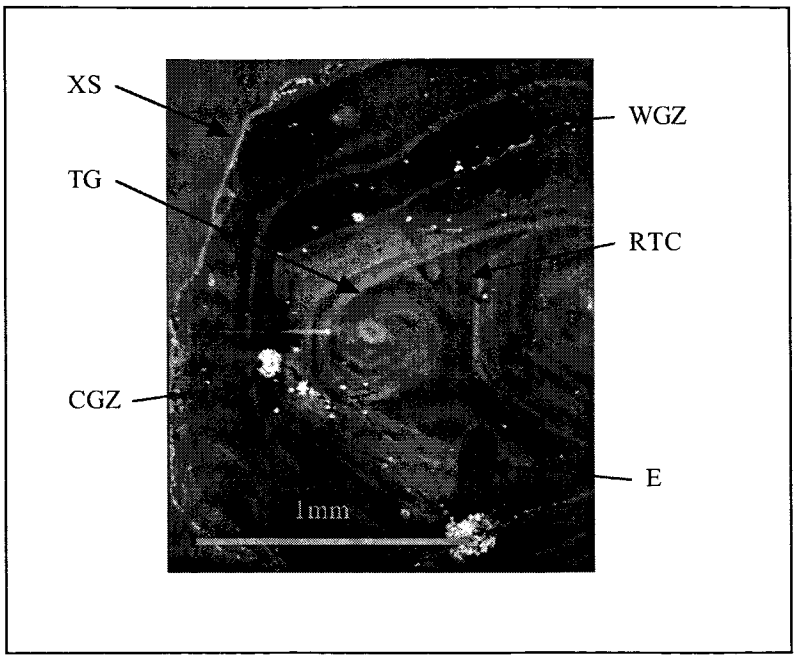

Figure 6.4. Scanning SEM cathodoluminescence images of a type II quartz phenocryst. In addition to many of the same features evident on the image of a type I phenocryst presented on Fig. 6.3, also apparent on On this image are: RTC = a relict paired core, E = embayments and XS the crystal edge.

The outermost zones evident in the relict core have been severely rounded and resorbed. Typically, a zone of strong luminescence, which measures between 10 and 250μm in thickness, follows this rounded, relict core. The outer termination of this zone is morphologically similar to dendritic crystal growths described earlier for type I phenocrysts. Concentric domains of successive dark and light luminescence response follow this brightly luminescent zone. Individually, bands measure between 10 and 250μm in thickness. Concentric growth zones are defined by sharp alternations between monotone light and dark growth bands and are bounded by

6.3.2.2 Type II

Cathodoluminescence images of phenocrysts belonging to group II show central parts to be composed of a relict paired crystal (Fig. 6.4). Zones, individually measuring several microns in thickness, commence at, or very near, to the core of the relict paired crystal. Mineral aggregates, represented by paired crystals or mineral intergrowths may be indicative of crystals derived from the crystal-rich walls of the magma chamber.

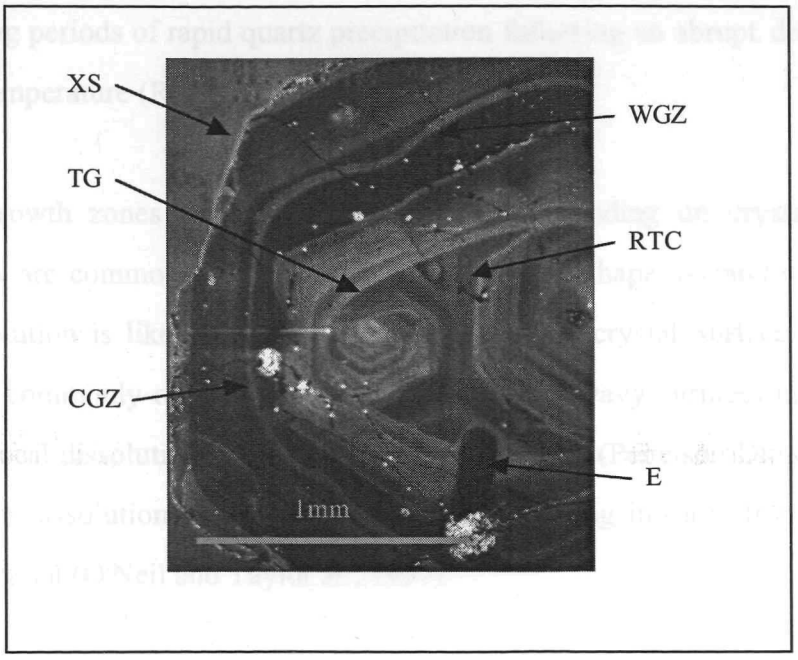

Figure 6.4. Scanning SEM cathodoluminescence images of a type II quartz phenocryst. In addition to many of the same features evident on the image of a type I phenocryst presented on Fig. 6.3, also apparent on On this image are: RTC = a relict paired core, E = embayments and XS the crystal edge.

The outermost zones evident in the relict core have been severely rounded and resorbed. Typically, a zone of strong luminescence, which measures between 10 and 250μm in thickness, follows this rounded, relict core. The outer termination of this zone is morphologically similar to dendritic crystal growths described earlier for type I phenocrysts. Concentric domains of successive dark and light luminescence response follow this brightly luminescent zone. Individually, bands measure between 10 and 250μm in thickness. Concentric growth zones are defined by sharp alternations between monotone light and dark growth bands and are bounded by

abrupt changes in luminescence intensity. Accordingly, crystallisation conditions necessary for the development of concentric zoning contrast significantly to those described for oscillatory zoning. The generation of concentric zoning requires repeated abrupt alterations in the nature of the precipitating fluid (Müller *et al.*, 2000). Concentric zones in plagioclase form following crystallisation from a dynamic medium of heterogeneous composition, variable precipitation, or periodic pulsation of fluid pressure or temperature (Anderson, 1984). Irregular, concentric growth zones may develop during periods of rapid quartz precipitation following an abrupt drop in fluid pressure or temperature (Roedder, 1984).

Concentric growth zones generally show significant rounding on crystal corners. Crystal edges are commonly wavy and euhedral crystal shape is rarely preserved. Crystal dissolution is likely to generate a wavy uneven crystal surface. Uniform luminescence commonly observed immediately overlying wavy surfaces may form in response to local dissolution and reprecipitation of quartz (Pennison-Dorland, 2001) or be due to a dissolution and reprecipitation front moving inwards from the outer edge of the crystal (O'Neil and Taylor Jr., 1967).

Figure 6.4 shows embayments in the Morenci phenocrysts cut through the existing growth zones. This suggests that embayment formation is attributable to a post-crystallisation process, such as the upwards drilling of gas bubbles into a crystal (Donaldson and Henderson, 1988). This upward movement causes small scale convection at the crystal-melt interface, due to gravitational instabilities caused by concentration gradients in the boundary diffusion layer, flushing undersaturated melt into the thin film of melt between the crystal and bubble.

6.3.3 Cathodoluminescence response and quartz morphology: Implications for the cause of variable cathodoluminescence response in quartz

The cause of variable cathodoluminescence response in quartz remains a source of great debate (D'Lemos *et al.*, 1997; Ramseyer *et al.,* 1988; Ramseyer and Mullis, 1990; Sprunt, 1981; Stevens Kalkeff and Phillips, 1995; Stevens Kalkeff *et al.,* 1997; Watt *et al.,* 1997). Detailed examination of the specific quartz morphologies within the phenocrysts, and the intensity of the luminescence response of each, demonstrates a correlation between the two. For example, in all of the samples studied, dendritic morphologies are manifested by bright luminescence (Fig. 6.3). As stated previously, dendritic morphologies form under rapid crystallisation, during high ΔT conditions (Swanson and Fenn, 1986). Accordingly, the observations presented here suggest bright luminescence to be generated in response to the defect species incorporated during crystallisation by the above mechanism. In addition, brightly luminescent quartz also characterises growth early in the evolution of an oscillatory zone (Fig 6.3). It is therefore suggested that the onset of each oscillatory zone is produced under a rapid crystallisation regime, at high ΔT conditions (Fig. 6.5). Progressive crystallisation leads to a reduction in the intensity of the luminescence response. The outermost regions of an oscillatory zone are characterised by euhedral, dipyramidal quartz morphologies, indicative of increasingly stable crystal growth at low ΔT conditions (MacLellan and Trembath, 1991). During such periods, crystallisation and trace element incorporation is strongly controlled by the planar growth of spiral growth steps around screw dislocations (Sisson *et al.*, 1993). Accordingly, individual oscillatory zones appear to record a sequence of ΔT conditions. Initiated by high ΔT, continued crystallisation leads to a increased stability in the system. The outer edges of individual oscillatory zones represent low ΔT conditions. The following zone is heralded by a sharp increase in ΔT, possible due to a degassing event.

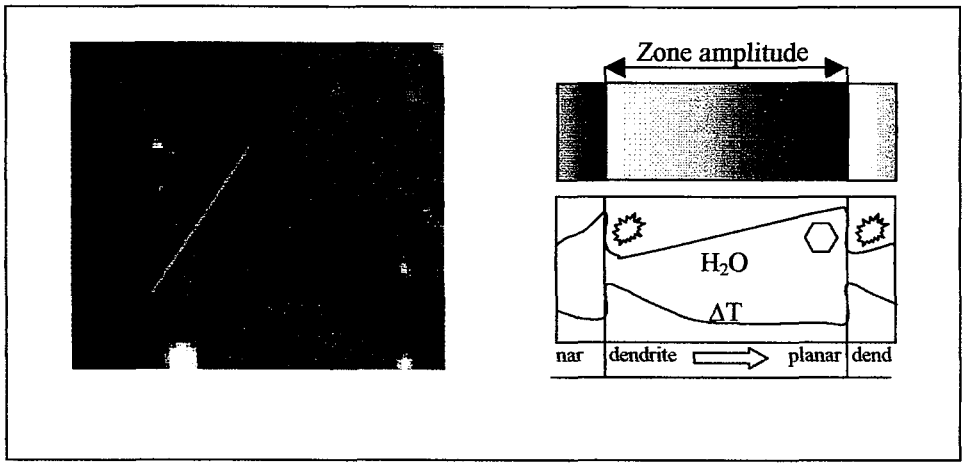

Figure 6.5. SEM-cathodoluminescence image and accompanying schematic diagram demonstrating the nature of oscillatory zoning in a quartz phenocryst illustrating the nature of individual zones. Strongly luminescent material commonly highlights dendritic morphologies and the onset of individual zones. This suggest that the strong luminescence is generated by impurity incorporation controlled by interface diffusion kinetics in response to rapid crystallisation under high DT conditions. Luminescence becomes progressively darker and the morphologies more euhedral as the zone progresses outwards. Trace element incorporation under stable conditions is strictly controlled by planar growth mechanisms leading to increasingly ordered crystal structures.

6.3.4 Petrologic Implications

In contrast to the chemical composition of feldspar, which due to self-organisation, remains in equilibrium with changing melt composition, quartz stability is governed by successive generations of different size, habit and structural states (MacLellan and Trembath, 1991). Cathodoluminescence images elucidate crystal interiors composed of sequences of individual growth zones (Fig. 6.3 and 6.4). The specific luminescence and morphology of a zone is dictated by the environment of crystallisation experienced while that part of the crystal is on the paleo-crystal surface. Accordingly, successive zones in individual phenocrysts record the crystallisation history experienced by the crystal through time. Because of this, and because the phenocrysts co-exist in a single hand specimen, the outermost zone on each phenocryst may be assumed contemporaneous a crude crystallisation history of the phenocryst may be established.

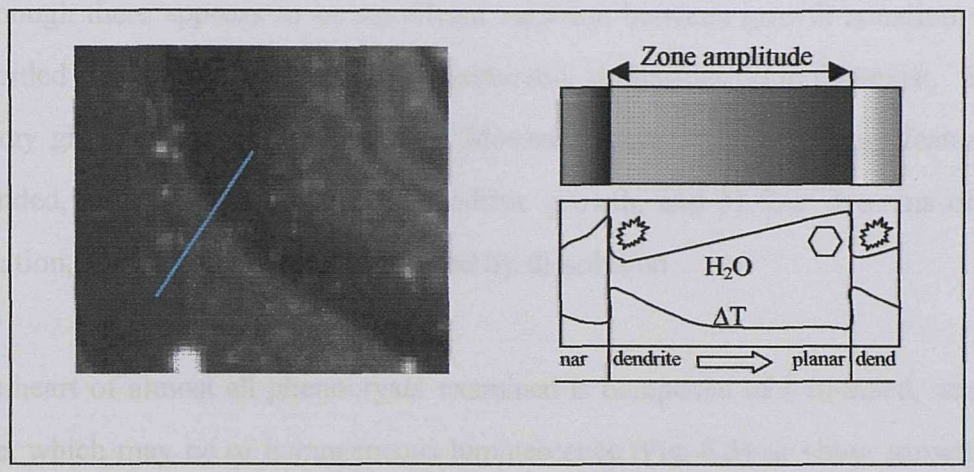

Figure 6.5. SEM-cathodoluminescence image and accompanying schematic diagram demonstrating the nature of oscillatory zoning in a quartz phenocryst illustrating the nature of individual zones. Strongly luminescent material commonly highlights dendritic morphologies and the onset of individual zones. This suggest that the strong luminescence is generated by impurity incorporation controlled by interface diffusion kinetics in response to rapid crystallisation under high DT conditions. Luminescence becomes progressively darker and the morphologies more euhedral as the zone progresses outwards. Trace element incorporation under stable conditions is strictly controlled by planar growth mechanisms leading to increasingly ordered crystal structures.

6.3.4 Petrologic Implications

In contrast to the chemical composition of feldspar, which due to self-organisation, remains in equilibrium with changing melt composition, quartz stability is governed by successive generations of different size, habit and structural states (MacLellan and Trembath, 1991). Cathodoluminescence images elucidate crystal interiors composed of sequences of individual growth zones (Fig. 6.3 and 6.4). The specific luminescence and morphology of a zone is dictated by the environment of crystallisation experienced while that part of the crystal is on the paleo-crystal surface. Accordingly, successive zones in individual phenocrysts record the crystallisation history experienced by the crystal through time. Because of this, and because the phenocrysts co-exist in a single hand specimen, the outermost zone on each phenocryst may be assumed contemporaneous a crude crystallisation history of the phenocryst may be established.

6.3.4.1 A crystallisation history?

Although there appears to be significant variation between growth zonation patterns recorded by two phenocryst types, considerable similarities do in fact exist. The bulk of any given quartz phenocryst from Morenci consists of three main features: 1) a rounded, relict core, 2) a zone of dendritic growth, and 3) four domains of growth zonation, separated by regions modified by dissolution.

The heart of almost all phenocrysts examined is composed of a rounded, xenocrystic core, which may be of homogeneous luminescence (Fig. 6.3) or show growth zoning (Fig. 6.4). Relict cores are representative of punctuated, two stage, crystal growth history (Cashman, 1992). Following initial crystallisation, each relict core records a significant dissolution event, which occurred following the cessation of the first major period of quartz growth (Armstrong, unpub. PhD thesis, Univ. Southampton, 1999). Resorption of the relict cores has resulted in significant crystal rounding which may cut across several of the existing cyclic growth zones. Due to the nature of this erosion, it is unclear how much of the original crystal has been removed by the disolution event. Rounding of the crystal edges, caused by resorption of quartz surfaces, is due to SiO_2 undersaturation of the melt, which may be caused by an increase in temperature, isothermal depressurisation or magma mixing (Holtz and Johannes, 1994). Cyclic growth zones in magmatic minerals are likely crystallise following devolatilisation or rapid uplift of the magma body (Anderson, 1984). The universal nature of the dissolution event across all of the phenocrysts examined, followed by crystallisation of contrasting quartz morphologies suggest a wide-scale change in the magma body during crystal growth.

Resorbed cores were then utilised as nuclei for the precipitation of growth zones during the second major growth event. Growth zones, which have crystallised on a resorbed surface, or immediately overgrowing a relict paired core, commonly define euhedral crystal forms. This contrasts sharply with observations of plagioclase zoning, where wavy zone boundaries, caused by mineral resorption, are continuously

mirrored by subsequent mineral growth zones (Pearce and Kolisnik, 1990). Variability in the form of successive growth zone morphologies in the two minerals probably reflects contrasting crystallisation mechanisms between the two outlined above.

The final event to be experienced by all of the phenocrysts is the development of four, successive growth zones. Although, as discussed previously, the mechanism involved in the generation of the growth zones described for each type differs, it is noted that the number of zones is the same for both. The hexagonal habit of the zoning suggests magmatic crystallisation at high temperatures (750°C; Yoder, 1950). Thus far it has been suggested that, because crystallisation and resorption of relict cores and the generation of dendritic morphologies are evident in all in quartz phenocrysts, both phenocryst types record the same, magma-chamber wide events. It therefore seems reasonable to assume that the development of four successive growth zones in each of the two phenocryst types, although they may be of a contrasting nature, probably also reflect the same events. It is suggested that variation in the types of growth zoning evident is attributable to the same system-wide event, but recorded by crystals in different positions in the melt. Cyclic, oscillatory zoning develops when a melt cannot convect and therefore the bulk chemical composition progressively changes with time (Allegre *et al.*, 1981; Haase *et al.*, 1980; Sibley *et al.*, 1976; Singer *et al.*, 1995). This could have been induced during periods of fractional crystallization of the melt, or perhaps continuous open system addition of melt to the system (D'Lemos *et al.*, 1997). Abrupt, concentric zoning requires dynamic crystallization (Müller *et al.*, 2000; Roedder, 1984). Accordingly, the mechanism employed in their development is likely to be environment controlled rather than due to local self-organisation. Rapid, repeated changes in temperature are unlikely due to the mechanics involved in heating and cooling such a large magma body. Zonation attributed to transport of grains into a different environment, either due to ascent or to convection seems a likely explanation (Anderson, 1984; Hibbard, 1991; Müller *et al.*, 2000). The frequency of the growth zoning, coupled with the rhythmic dissolution events may be consistent with

turbulent convection in slow, steady-state flow of viscous magma. Quartz zonation in the outer parts of the phenocryst may be analogous to plagioclase crystals undergoing dissolution as they descended to the hotter parts of a magma chamber followed, in the ascending, cooling limbs, by the resumption of slow, near-equilibrium growth (Marsh, 1988; Marsh and Maxey, 1985). Because no two crystals traversed identical paths in the magma chamber, and not all convection cells have the same geometry or thermal gradient, variable conditions experienced by individual crystals within these cells would lead to the development contrasting textural patterns.

Chapter 7

CATHODOLUMINESCENCE RESPONSE AND TRACE ELEMENT HYDROXYL GROUP ZONING IN QUARTZ PHENOCRYSTS

7 Scanned cathodoluminescence images: High-resolution determination of OH-related defect concentrations in magmatic quartz

7.1 INTRODUCTION

Luminescence is the emission of electromagnetic radiation from a material when it is excited by some form of incident energy. Usually the emitted radiation lies at or near to frequencies in the visible range. The incident ray may be in the form of electromagnetic radiation (e.g. photoluminescence, X-ray luminescence etc.), heat (thermoluminescence), vibrations, (sonoluminescence) or following bombardment with electrons (cathodoluminescence). Cathodoluminescence (CL) emissions may be measured by either, 1) recording the spatial distribution of regions displaying variable luminescence, or 2) recording the spectral intensity of the emission. The former, high resolution scanned SEM-CL imaging at a single wavelength, has developed into a powerful petrologic technique which may reveal textural variations in quartz, not normally detected using other analytical methods (Marshall, 1988; Ramseyer and Mullis, 1990; Perny, *et al.*, 1992; D'Lemos, *et al.*, 1997; Pennison-Dorland, 2001). Scanned SEM-CL has been successfully applied to the elucidation of complex growth histories in quartz from numerous geological environments (Koyama, 1980; Owen and Carozzi, 1986; Hogg, *et al.*, 1992; Onasch and Vennemann, 1995; Demars, *et al.*, 1996; Valley and Graham, 1996; Götze, *et al.*, 1999; Graupner, *et al.*, 2000; Müller, *et al.*, 2000; Pennison-Dorland, 2001).

Despite the frequent employment of CL as a tool for determining the presence of internal heterogeneities in quartz, the cause of variable luminescence in quartz remains poorly understood (Zinkernagel, 1978; Sprunt, 1981; Ramseyer and Mullis, 1990; Perny, *et al.*, 1992; Demars, *et al.*, 1996). Accordingly, the maximum potential of CL images as petrological tool may not yet have been fully realised. Recently, considerable work has being carried out in an attempt to relate CL response with specific impurity defects in quartz (Stevens Kalkeff and Phillips, 1995; Ramseyer, 1996; Stevens Kalkeff, *et al.*, 1997). Variable CL emissions are thought to be related to aluminium in the sample

(Sprunt, 1978; Halliburton, *et al.*, 1981; Marshall, 1988; Ramseyer, *et al.*, 1988; Itoh, *et al.*, 1990; Ramseyer and Mullis, 1990; Bahadur, 1993; Stevens Kalkeff and Phillips, 1995; D'Lemos, *et al.*, 1997; Guzzo, *et al.*, 1997; Stevens Kalkeff, *et al.*, 1997; Watt, *et al.*, 1997), which may cause variable CL emissions either 1) directly, by simple chemical zonation on a micron to submicron scale or, 2) indirectly by distorting the crystal lattice of the quartz structure. Quantitative, in situ measurements of the bulk aluminium concentration in quartz have recently become possible using SIMS (Hervig and Peacock, 1989; Rovetta, *et al.*, 1989). Using this and electron microprobe techniques, a positive correlation between Al content, and CL response has been suggested by some authors (Ramseyer, *et al.*, 1988; Ramseyer and Mullis, 1990; Demars, *et al.*, 1996). However, Ramasayer and Mullis (quoted in Marshall, 1988) suggest an inverse relationship between Al content and CL response, whilst others found no simple correlation (Sprunt, 1981; Perny, *et al.*, 1992).

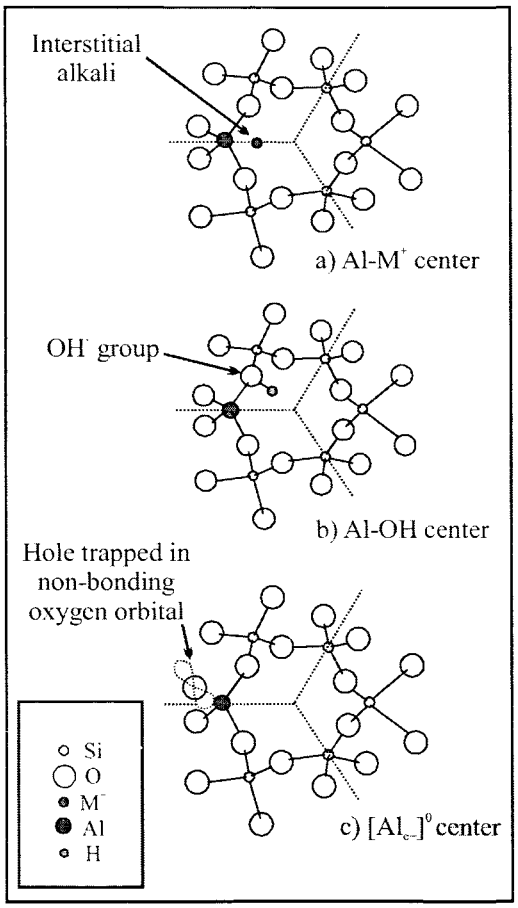

FIGURE 7.1. Schematic diagram illustrating (a) the Al-M$^+$ center (where M = either Li, Na or K), (b) the Al-OH center (Kronenberg 1994), and (c) the [Al$_{c-}$]^0 center. Field of view is down the optical *c*-axis of the crystal.

Although Al^{3+} substitution for Si^{4+} is the most common impurity in natural and synthetic quartz (Kats, 1962; Aines and Rossman, 1984; Rovetta, *et al.*, 1989; Kronenberg, 1994), to retain charge neutrality, this exchange must be additionally charge compensated by the incorporation of H^+, Li^+, Na^+, or K^+ ions at interstitial sites, or electron holes trapped at oxygen ions (Kats, 1962; Halliburton, *et al.*, 1981; Aines and Rossman, 1984; Itoh, *et al.*, 1990; Bahadur, 1993; Iwasaki, and Iwasaki, 1993; Kronenberg, 1994; Guzzo, *et al.*, 1997). Strong Coulombic attraction locates the charge compensators adjacent to the substitutional Al^{3+} ions (Momburquette and Weil, 1985), giving rise to either Al-M^+ (where M= Li^+, Na^+ or K^+), Al-OH^- or $[Al_{e+}]^0$ centres (Fig. 7.1). Due to the diverse chemical and physical nature of these Al-related species no one technique permits reliable identification of every individual centre. $[Al_{e+}]^0$ centres form a paramagnetic defect, which may be detected by electron spin resonance (ESR), (Halliburton, *et al.*, 1981; Weil, 1984). OH-related defect centres are easily observed using infrared spectroscopy where the highly polarised stretching motions of specific centres absorb energy at discrete wavelengths in the infrared spectrum (Kats, 1962; Aines and Rossman, 1984; Paterson, 1989; Kronenberg, 1994).

Previous studies aimed at correlating CL response with Al content have utilised techniques which record total Al contents measured at each analytical point and so may miss variable concentrations of individual Al-related species in the sample. Calculations of the geometric configurations necessitated by the substitutional Al-M and Al-OH centres show that interstitial Li^+ located near to Al^{3+} does not break the twofold symmetry of the *x*-axis, however this symmetry is broken following the incorporation of H^+ (Momburquette and Weil, 1985). Lattice deformation caused by the substitution of Al-OH defects may therefore prove a likely mechanism in generating variable CL in quartz. Accordingly, the presence of variable concentrations of Al-OH defect in the sample may prove significant in establishing the mechanisms responsible for the generation of variable CL response in quartz. Al-OH centres are formed when an interstitial H^+ ion is bonded to an oxygen atom, adjacent to a substitutional Al^{3+} (Kats, 1962; Aines and Rossman, 1984; Paterson, 1989; Kronenberg, 1994). The resulting OH defects in the crystal lattice give rise to sharp absorption bands in the infrared spectrum at 3435, 3371 and 3311 cm^{-1} (Kats, 1962).

Recently, the advent of Fourier Transform Infrared micro-spectroscopy (micro-FTIR) has been successfully applied to the quantitative analysis of hydrous components in minerals with resolution down to 10 μm in diameter (McMillan and Hofmeister, 1988). Here, microprobe microanalysis, which enables examination of the spatial distribution of bulk Al in the sample, are used in conjunction with micro-FTIR determination of the Al-OH species throughout an optically oriented section of a natural quartz phenocryst. The primary objective was to investigate the role of OH-related species in generating variable cathodoluminescence response in natural quartz crystals.

7.2 EXPERIMENTAL METHODS

7.2.1 Sample Preparation

In this study, a natural dipyramidal quartz phenocryst from an intrusion associated with the Morenci Porphyry copper deposit, Arizona (Chapter 5), was separated from the groundmass following a process of coarse crushing and selected by hand under an optical microscope. The apical points of the phenocryst were removed and the crystal mounted perpendicular to the optical *c*-axis. The orientated crystal was then set in resin and fashioned into a 200 μm thick, double polished fluid inclusion wafer. The wafer was then mounted onto a glass slide and carbon coated for cathodoluminescence analysis. For micro-infrared spectroscopic investigation, the wafer was removed from the glass slide and cleaned to remove any remnants of the carbon coating and adhesive from the sample.

7.2.2 Cathodoluminescence images

Monochromatic scanned cathodoluminescence images were collected using a K.E. Developments cathodoluminescence detector mounted on a Hitachi S2500 scanning electron microscope. A typical accelerating potential of 20 kV was used with a 20 *n*A gun velocity.

7.2.3 Electron Microprobe analysis

Trace element concentrations in the sample were measured using a Cameca SX50 microprobe at the Natural History Museum, London. Operating conditions were; beam energy of 15 kV; sample current of 60 nA; and a counting time of 60 seconds. Calculated detection limit for aluminium in quartz was 0.005 wt% (47 ppm).

7.2.4 Infrared spectroscopy

The nature of OH-related defect species in the quartz phenocryst were obtained at room temperature on a Nicolet™ protégé 460 Fourier Transform infrared spectrometer, coupled with a Nic-plan™ infrared microscope. Infrared light, passed via a KBr beamsplitter, is focused through the sample onto a liquid nitrogen cooled mercury-cadmium-telluride (MCT) detector. Profiles of the Al-OH defect centres were obtained on samples which were mounted on a motorized sample stage allowing movement in an X-Y direction. Altμs™ software permits analytical traverses to be programmed into the computer whilst observing the sample using optical light and the routine analysis of a sequence of points across the phenocryst using infrared. One hundred and twenty eight scans were accumulated for each analytical point at a resolution of 4 cm^{-1}. The data were acquired and manipulated using Omnic™ software. To create hydrogen concentration-depth profiles across the crystal, a rectangular aperture, measuring 30 μm perpendicular to and 100 μm parallel to the edge of the crystal, was programmed into the computer.

Hydrogen species concentrations were determined by subtracting the sample spectrum with a reference spectrum taken in through air. Absorptions at associated with individual defect were subtracted from the spectrum using baseline correction and the heights of the individual absorptions established. Concentrations of an absorbin species can be determined through Beer's law calibration based upon:

$$A \text{ (Absorbance)} = \varepsilon \, d \, c$$

Where, Absorbance is the height of the absorbance peak, d is the thickness of the sample in cm, ε is the molar absorptivity, a constant for each species of interest, and c is the concentration of the water species (mol^{-1}) (Aines and Rossman, 1984).

7.3 RESULTS

7.3.1 Interpretation of SEM-CL zoning textures

Cathodoluminescence images of the quartz phenocryst enable numerous textural features associated with crystal growth to be readily distinguished (Fig. 7.2). Most notably, the crystal shows several distinct oscillatory zones, which define a trend consistent with the euhedral crystal edges. The frequent parallelism of successive growth zones with quartz phenocryst edges suggests, 1) the observed growth textures are of magmatic primary origin, and, 2) oscillatory zoning may be caused by progressive changes in crystallisation conditions experienced during crystal growth. Within any single zone, a crystallisation sequence initiated by a brightly luminescent interior progressively decreases in intensity towards a poorly luminescent exterior. The intensity of the luminescence response may also be correlated with growth morphology. A strongly luminescent response is found in regions of irregular growth (Fig. 7.2), which are morphologically similar to dendritic crystals described in the literature (Doherty, 1974).

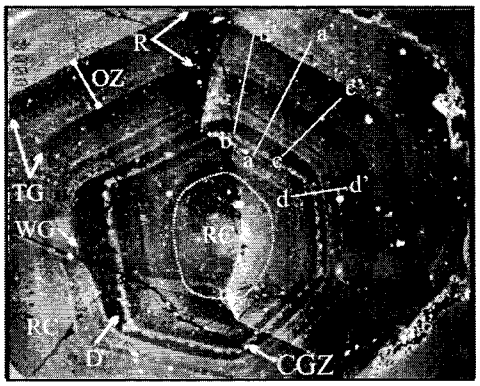

FIGURE. 7.2. A cathodoluminescence image of thin section of a quartz phenocryst examined in this study. Line of sight follows the optical c-axis of the crystal. Evident on the image are OZ, oscillatory growth zones showing rounded internal zones superceded by euhedral growth zones, D = dendritic zones, WG = wavy growth zones, RC = spherical core, TG = truncated growth zones, R = crystal rounding, CGZ = concentric growth zones, RC = zones of constant luminescence. The hatched region of the crystal was destroyed during sample preparation for infrared analysis. Sections a-a', b-b' and c-c' correspond to micro-FTIR analytical traverses performed for this study. Line a-a' also shows the approximate position of the microprobe traverse detailed in the text.

7.3 RESULTS

7.3.1 Interpretation of SEM-CL zoning textures

Cathodoluminescence images of the quartz phenocryst enable numerous textural features associated with crystal growth to be readily distinguished (Fig. 7.2). Most notably, the crystal shows several distinct oscillatory zones, which define a trend consistent with the euhedral crystal edges. The frequent parallelism of successive growth zones with quartz phenocryst edges suggests, 1) the observed growth textures are of magmatic primary origin, and, 2) oscillatory zoning may be caused by progressive changes in crystallisation conditions experienced during crystal growth. Within any single zone, a crystallisation sequence initiated by a brightly luminescent interior progressively decreases in intensity towards a poorly luminescent exterior. The intensity of the luminescence response may also be correlated with growth morphology. A strongly luminescent response is found in regions of irregular growth (Fig. 7.2), which are morphologically similar to dendritic crystals described in the literature (Doherty, 1974).

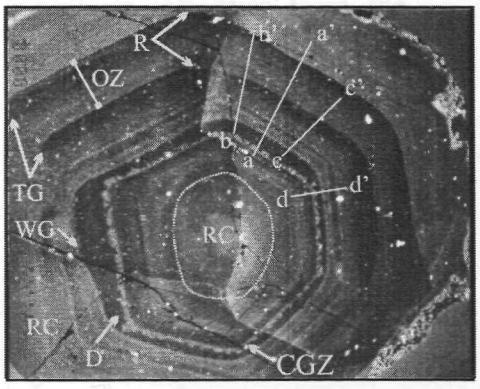

FIGURE. 7.2. A cathodoluminescence image of thin section of a quartz phenocryst examined in this study. Line of sight follows the optical c-axis of the crystal. Evident on the image are OZ, oscillatory growth zones showing rounded internal zones superceded by euhedral growth zones, D = dendritic zones, WG = wavy growth zones, RC = spherical core, TG = truncated growth zones, R = crystal rounding, CGZ = concentric growth zones, RC = zones of constant luminescence. The hatched region of the crystal was destroyed during sample preparation for infrared analysis. Sections a-a', b-b' and c-c' correspond to micro-FTIR analytical traverses performed for this study. Line a-a' also shows the approximate position of the microprobe traverse detailed in the text.

7.3.2 Trace element chemistry and cathodoluminescence response in quartz

7.3.2.1 Electron microprobe

The incorporation of impurity aluminium into quartz is a likely candidate for generating variable CL response (Sprunt, 1978; Halliburton., *et al.*, 1981; Marshall, 1988; Ramseyer, *et al.*, 1988; Itoh, *et al.*, 1990; Ramseyer and Mullis, 1990; Bahadur, 1993; Stevens Kalkeff and Phillips, 1995; D'Lemos, *et al.*, 1997; Guzzo, *et al.*, 1997; Stevens Kalkeff, *et al.*, 1997; Watt, *et al.*, 2000). However, the precise role it plays remains controversial (Sprunt, 1981; Ramseyer, *et al.*, 1988; Stevens Kalkeff, *et al.*, 1997; Watt, *et al.*, 2000). Based upon the patterns generated in the CL images, an electron microprobe was used to measure concentrations of Si, Al, K, Fe and Ti concentrations throughout the quartz phenocryst (Fig. 7.3). Microprobe analysis revealed no credible correlation between the concentrations of any impurity element with CL response. Concentrations of K, Fe and Ti remained negligible throughout most of the analysis although, like Al, which regularly produced concentrations of between 0.01 and 0.02 wt%, are occasionally punctuated by spuriously high measurements. The abrupt nature of these readings is attributed to the analysis of included mineral phases or traces of corundum left over from the polishing process rather that a true measurement of impurity Al in the phenocryst.

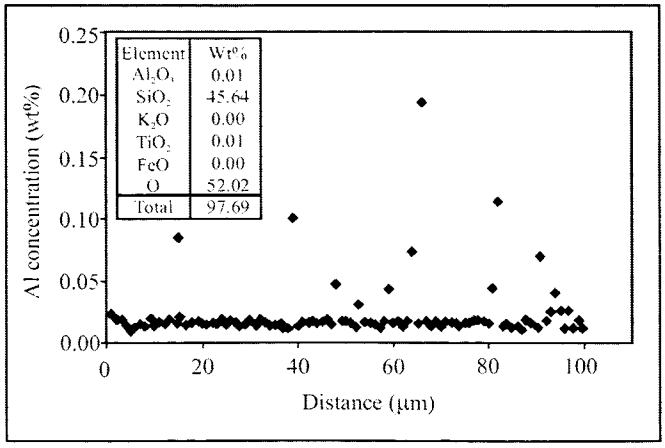

FIGURE 7.3. a) absolute Al content vs. distance traveled on the traverse outlined on Fig. 3. and, b) a table detailing representative major element concentration in quartz. Both data sets were determined by electron microprobe. The detection limit for aluminum in the samples was calculated at 0.005wt% (47ppm). The impurity aluminum content of the quartz analyzed is similar to that described in phenocrysts from Esperanza porphyry, Chile (Watt et al., 1997) and typical of magmatic quartz (Heaney, 1994).

7.3.2.2 Infrared Spectroscopy

On the room temperature infrared spectrum of the orientated quartz section, OH defects in the quartz lattice give rise to numerous sharp bands at superimposed upon a broad absorption centred at ~3440 cm^{-1} (Fig. 7.4). The band caused by the Al-OH centre, occurs at 3380 cm^{-1}. Also evident on Figure 7.4 are sharp bands at 3484 cm^{-1} and 3308 cm^{-1} attributed to Li-dependant OH centres (Kats, 1962; Aines and Rossman, 1984; Bahadur, 1989; Paterson, 1989; Kronenberg, 1994), and overtone and/or combination bands of Si-O vibrations at 3424 cm^{-1} (Kats, 1962; Guzzo, *et al.*, 1997). Unlike structurally bound Al-related centres, Li-related OH impurities are incorporated into the quartz structure as neutrally charged molecules and are not though to be an integral part of the crystal lattice (Paterson, 1989; Ihinger and Zink, 2000). The broad band at ~3440 cm^{-1} has been attributed to Si-OH groups (Griggs and Blacic, 1965), small aggregates of molecular water (Aines and Rossman, 1984) and the hydrogarnet substitution (Weil, 1984).

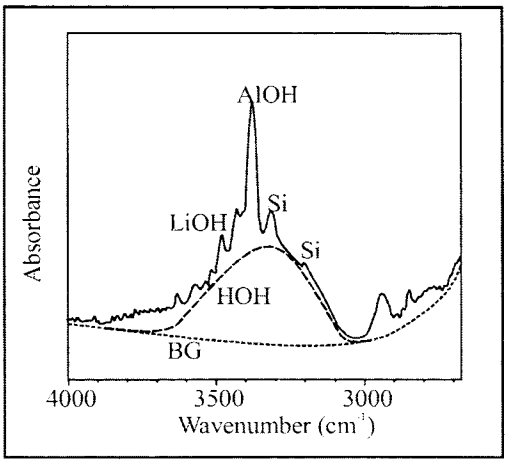

FIGURE 7.4. Room temperature infrared absorbance spectrum of a natural α-quartz phenocryst from Morenci. The spectrum was obtained at room temperature by passing the infrared beam through a 200 μm thick, double polished fluid inclusion wafer. The spectrum shows several sharp bands superimposed upon a broad band absorption associated with stretching vibrations of the water molecule, although the precise nature of the molecule and the mechanism by which it is incorporated into quartz remains controversial (see text). The most intense of the sharp absorption peaks at 3380 cm^{-1} is assigned to Al-OH centres created following the substitution of an Al in place of a structural Si^{4+}. Exact specitation of the peak at 3484 cm^{-1} remains unclear but it has been ascribed to Li-dependant OH stretching vibrations. Bands marked Si are assigned to be the overtone and/or combination bands of Si-O vibrations (Kats, 1962).

7.3.2.3 Infrared micro-spectroscopy

Although bulk aluminium content bears no resemblance to the observed CL data (Fig. 7.3), Al may be incorporated into the quartz crystal lattice by several mechanisms, leading to the generation of various Al-related centres (Fig. 7.1). In order to determine whether the variable cathodoluminescence response observed in the sample could be associated with specific Al-related defects, this study focused on the possible relationship between cathodoluminescence response and the concentration of Al-OH species. Li-dependant OH species have been previously shown to be subject to significant post-crystallisation remobilisation, (Ihinger and Zink, 2000) and as the observed textures are interpreted as primary crystallisation features, are not considered further here. An analytical traverse, aimed at determining the relative quantities of Al-OH species in same region of the sample as analysed using electron microprobe, was performed using micro-FTIR spectroscopy (Fig. 7.3). The linear traverse was composed of a sequence of analytical points programmed into the computer at 20 μm increments. The raw spectra generated by the micro-spectroscopic analytical traverse are presented on Figure 7.5, which clearly shows variable concentrations of hydrogen-related species at different points throughout the crystal. Throughout all analyses, the band generated by Al-OH centres consistently provided the strongest absorbencies. Despite this, it is worth noting that uncertainties in the specific absorption coefficient for each absorbing species inhibit the determination of absolute concentration of OH-related species in the sample. The traverse spectra merely enable the comparison between the concentrations of each absorbing species relative to other points on the traverse.

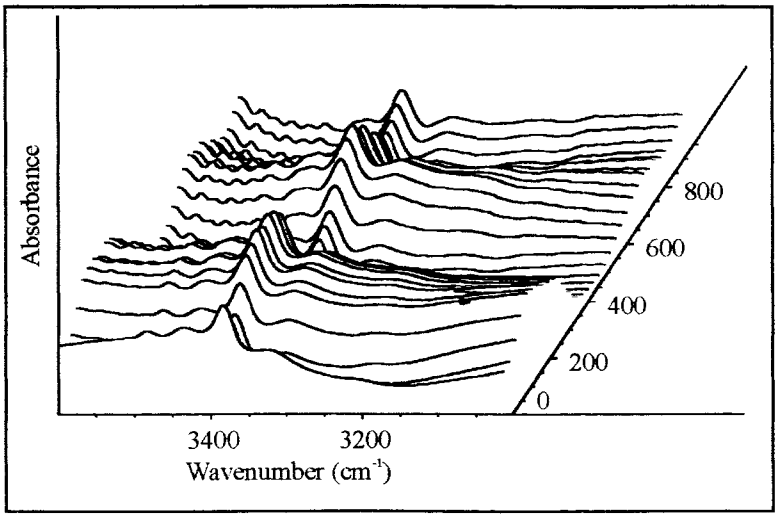

FIGURE 7.5. Stacked infrared spectra obtained from traverse a-a' depicted on Fig. 7.2, permitting ready identification of variation in the intensity of the Al-OH absorption at 3380 cm^{-1}.

The sample spectrum for each point was extracted from the spectral compilation obtained by the computer following the traverse (Fig. 7.5), and examined individually. Absorbencies associated with H-OH species in the sample were removed from the baseline. The content of Al-OH centres were evaluated by assuming that the peak at 3380 cm^{-1} is simply superimposed upon that generated by H-OH species. Peak heights associated with individual absorbing species were then plotted against distance travelled along the traverse (Fig. 7.6).

Sample thickness (200 μm), and the frequency of the absorptions associated with the Al-OH band (3380 cm^{-1}) remain constant throughout the traverse. Accordingly, variations in the intensities of the H-OH and Al-OH absorptions may be solely attributed to variations in the absolute concentration of OH-related centres. Due to the Beer-Lambert relationship outlined above, assessment of peak heights provides an accurate determination of the relative concentration of hydrous species across the sample. Coupled examination of the results of the spectroscopic traverse (Fig. 7.5) with the cathodoluminescence image (Fig. 7.2) correlates regions of high H-OH concentration with parts of individual growth zones displaying the most intense luminescence response. Al-OH concentrations do not vary significantly across the sample. It is noted that the highest H-OH contents are measured at analytical points recorded towards the core of the phenocryst (Fig. 7.6) and attribute this feature to the geometry of the crystal at the point through which the infrared beam passed. The sectioning process shall cut in an almost perpendicular fashion through zones near to the core of the crystal, providing an true measure of the hydrous species present in that zone. Geometrically, zones towards the crystal edge must be sectioned obliquely and, accordingly, transmission of the infrared beam through this will result in the analysis of not only the zone as imaged on the surface by SEM-CL, but also regions underneath this which may contain a significantly lower OH content.

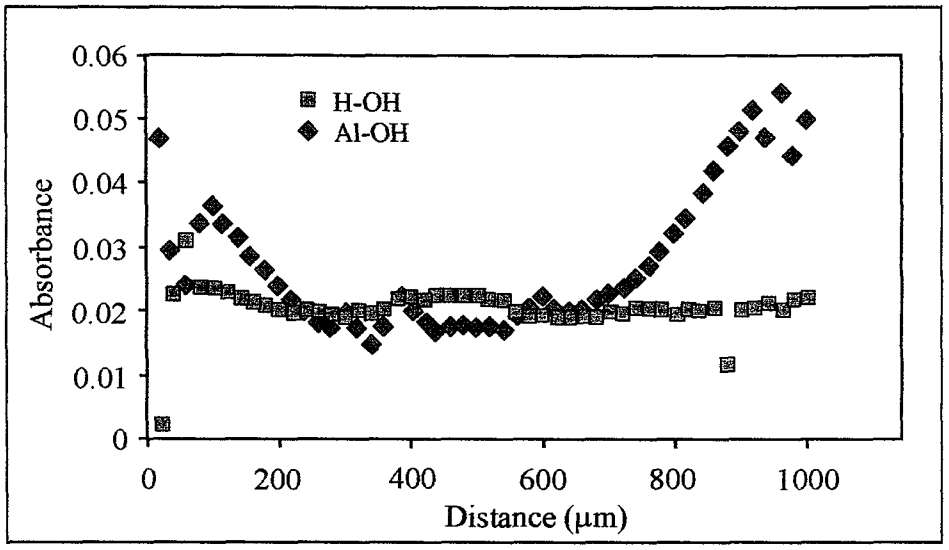

FIGURE 7.6. The intensity of the absorptions generated by H-OH (3440cm^{-1}) and Al-OH (3381 cm^{-1}) throughout the traverse outlined on Figure 7.3.

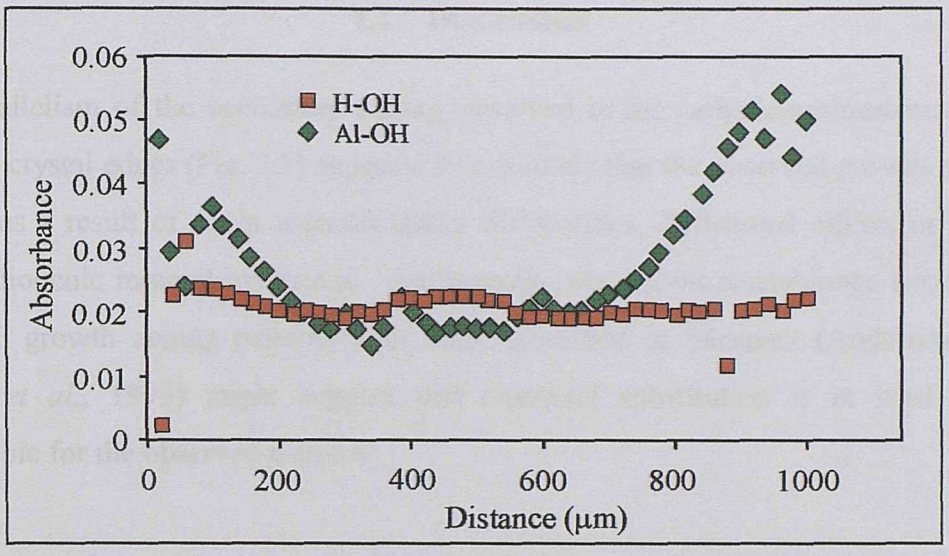

FIGURE 7.6. The intensity of the absorptions generated by H-OH (3440cm^{-1}) and Al-OH (3381 cm^{-1}) throughout the traverse outlined on Figure 7.3.

7.4 DISCUSSION

The parallelism of the oscillatory zoning observed in the cathodoluminescence image with the crystal edges (Fig. 7.2) suggests it is unlikely that the observed growth zonation formed as a result of strain induced lattice dislocations, diffusional effects or damage from radiogenic mineral inclusions. Additionally, significant resemblance between the observed growth zoning patterns with those described in feldspars (Anderson, 1984; Singer, *et al.*, 1995) might suggest that chemical substitution is at least in part responsible for the observed patterns.

Comparison of the observed textural features with those described in other minerals, coupled with knowledge of crystallisation kinetics, permits a crude crystallisation history of the phenocryst to be assembled. Maclellan and Trembath (1991) noted that, depending on the degree of undercooling and time allowed for crystallisation, experimentally grown quartz crystals could take the form of several morphologies. Growth of dendritic morphologies is restricted to crystallisation at high degrees of undercooling (Mullis, 1996). High degrees of undercooling may dominate in the system following rapid ascent of a partially crystallised magma into a high-level magma chamber (Kerr, 1995), or following sudden decompression of the intrusive system (Anderson, 1984).

7.4.1 Relationship between CL and hydrous species

Micro-infrared spectroscopy has been previously used to determine of the variable abundance of hydrogen bearing impurities in quartz in an attempt to record the rate of crystal growth (Ihinger and Zink, 2000). The results presented in this study (Fig. 7.6), coupled with the nature of quartz morphologies elucidated by the CL images, further consolidate the use of hydrogen defects in quartz as a measure of crystal growth speed. The concentration and speciation of defects incorporated into a growing quartz crystal are controlled by the crystallographic structure of the mineral and the growth mechanism at the time of defect incorporation (Ihinger and Zink, 2000). Because quartz growth mechanism is itself controlled by the rate of crystal growth (MacLellan and Trembath, 1991), measurement of defect concentration at any given point in the crystal permits the

rate of growth of that point to be evaluated (Ihinger and Zink, 2000). Following examination of the CL images (Fig. 7.2), it is noted that external regions of individual growth zones contain low H-OH impurity concentrations. These outer regions of individual zones are generally of dark luminescence and define euhedral quartz morphologies which reflect the ordered incorporation of impurity components during periods of stable planar growth at small degrees of undercooling (Swanson and Fenn, 1986; MacLellan and Trembath, 1991). In contrast, sections of the crystal displaying the highest H-OH contents are identified in regions which define dendritic morphologies (Fig. 7.6). These textural features suggest rapid crystallisation in response to large degrees of undercooling (Swanson and Fenn, 1986) where growth rate is regulated by lateral growth steps from surface nucleation, and interface diffusion kinetics (Dowty, 1980).

7.4.2 Cause of variable CL response in quartz

Although the role of hydrous defects in influencing luminescence response in quartz has been previously noted (Owen and Carozzi, 1986), much work has focused on the role of aluminium (Mackey, 1963; Halliburton *et al.*, 1981; Itoh, *et al.*, 1990; Stevens Kalkeff and Phillips, 1995; Stevens Kalkeff, *et al.*, 1997). Using bulk analytical techniques (e.g. electron and ion micro-probe analysis) site specific determination of the concentration retained by individual species cannot be attained, and as a result, Al-OH, Al-M^+ and $[Al_{e+}]^0$ centres, along with included mineral phases are all included in the recorded result. Calculation of the reaction energies released when the uncompensated $[AlO_4]^-$ centre combines with one of the possible compensators (H^+, Li^+ or Na^+) suggests that the Al-OH centre is significantly more stable than other Al-related centres (Momburquette and Weil, 1985). Irradiation experiments found that H^+ ions will be more easily incorporated interstitially into the quartz framework than Li and Na ions (Halliburton *et al.*, 1981). Geometric configurations suggest that the quartz lattice will be significantly less distorted by the formation of Al-Li centres than Al-OH centres (Guzzo, *et al.*, 1997). Accordingly, the controversy that exists in detailing the role of Al in generating cathodoluminescence response (Sprunt, 1981; Ramseyer and Mullis, 1990; Perny, *et al.*, 1992; Demars, *et al.*, 1996; Watt, *et al.*, 1997), may be attributed, not to the absolute concentration of the specific element measured, but to the nature of that element and

how it is contained within the species. In the case of quartz, quantification of total Al concentration and refinement of the role played by individual Al species in generating variable cathodoluminescence in quartz may benefit significantly from investigation of the nature of the contributions made by Al defects. Due to the arguments outlined above, that lattice distortion associated with incorporation of Al-OH species may provide a likely mechanism for the generation of variable CL in quartz, however the results of this study would suggest otherwise. Indeed, the results presented here would suggest that H-OH contents impose a primary control in generating the observed luminescence.

7.5 CONCLUSIONS

Variable concentrations of H-OH species measured in study are significant because, 1) they represents a significant development in determining the cause of variable luminescence in quartz, and 2) it suggests that scanned CL images may be used to provide a rapid estimate of the concentration of H-OH species throughout the entire crystal. Micro-FTIR spectroscopy demonstrates a correlation between regions of bright luminescence with regions displaying augmented H-OH concentrations. Correlation between rapidly grown crystal morphologies, elucidated by cathodoluminescence images, and high concentrations of OH-related defects further support the suggestion of Ihinger and Zink (2000) that determination of OH-related defect concentrations may provide an accurate measure of crystal growth rate. Further, this study suggests that scanned CL images of quartz crystals provide rapid determination of crystal-wide OH concentration.

Chapter 8

HALOGEN GEOCHEMISTRY OF A PORPHYRY FORMING MELT AND ASSOCIATED VAPOUR PHASE CALCULATED FROM APATITE AND BIOTITE COMPOSITIONS

8 The halogen geochemistry of a granite melt associated with porphyry copper mineralisation, Morenci, Arizona

8.1 INTRODUCTION

Porphyry copper deposits are related to the final, cooling stages of hydrous magmas which have been emplaced to shallow (1-4 km) depths in the crust. Large quantities of volatile constituents (H_2O, CO_2, S, Cl, F) are exsolved and discharged by the magma as a consequence of depressurisation experienced during emplacement. The importance of these components in generating hydrothermal ore forming systems is well established. The halogen (Cl and F), H_2O, and S concentrations of these fluids effect a variety of processes which determine the ore-forming potential of a system, such as the timing of vapour saturation, and the partitioning and complexing of important cations (Candela and Holland, 1984; Candela and Holland, 1986). Understanding the origins of halogen enrichment in the magmatic volatile phase provides workers with an important insight into the genesis of ore bearing magmas (Anderson *et al.*, 1989; Dilles, 1987; Lowestern, 1993; Lowestern, 1994a; Lowestern, 1994b) and much attention has focussed on methods of determining the relative fugacities of halogens in these systems (Gunow *et al.*, 1980; Munoz, 1984; Munoz, 1992; Munoz and Ludington, 1974).

As a silicate melt cools, it becomes saturated with halogen bearing minerals such as apatite and biotite. These crystallise with variable halogen ratios and are recognised as potential indicators of the relative activities (fugacities) of HF (f_{HF}) and HCl (f_{HCl}) in the precipitating fluid (Finch *et al.*, 1995; Munoz and Swenson, 1981; Parsons *et al.*, 1991; Sisson, 1987; Yardley, 1984). A common accessory mineral in almost all igneous rocks, apatite contains OH, F, and Cl in its structure. Homogenous solid solution in the ternary system; hydroxylapatite, $[Ca_{10}(PO_4)_6(OH)_2]$, chlorapatite $[Ca_{10}(PO_4)_6Cl_2]$, and fluorapatite $[Ca_{10}(PO_4)_6F_2]$ is possible across the entire compositional range (Tacker and Stormer, 1989) because apatite incorporates the larger Cl^- ion in an entirely different site to F and OH (Hughes *et al.*, 1990). Typically the first, if not only, halogen bearing mineral to crystallise, this ideal solid solution suggests that apatite composition may provide an insight into the halogen evolution in magmas (Piccoli and Candela, 1994) and indicate volatile fugacity in magmatic processes (Piccoli *et al.*, 1999). Apatites have also been used

to provide a temporal record of the sulphur evolution of oxidised magmas associated with porphyry copper systems (Streck and Dilles, 1998).

Unlike apatite, the halogen content of biotite is strongly controlled by crystal-chemical factors (Gunow *et al.*, 1980). Thanks to its frequent occurrence and wide compositional range, biotite provides a useful indicator of the halogen composition of the magma or fluid from which it was precipitated (Gunow *et al.*, 1980; Munoz, 1984; Munoz, 1992; Munoz and Ludington, 1974). F, Cl and OH contents of biotite have been previously used to determine the composition and circulation of fluids during, and subsequent to, the emplacement of plutons (e.g. Finch *et al.*, 1995; Munoz and Swenson, 1981). Additionally, biotite halogen concentrations have been recently used to infer the halogen fugacities of several intrusions associated with porphyry copper deposits (Jacobs and Parry, 1979b; Munoz and Swenson, 1981; Selby and Nesbitt, 2000).

This study reports on electron microprobe analyses of quartz-included apatite and biotite crystals from the Younger Granodiorite Porphyry intrusion which is associated with the Morenci porphyry copper deposit, Arizona. In the samples, apatite and biotite micro-crystals are found trapped within quartz phenocrysts. Their inclusion within these quartz hosts suggest that the data recovered may have escaped the effects of subsequent, intense hydrothermal alteration and analysis provides an opportunity to investigate magmatic conditions early in the crystallisation history of the system, but also crystallisation of the quartz phenocrysts. This study uses 1) apatite halogen concentrations to infer initial volatile concentrations in the magma (Piccoli and Candela, 1994). 2) apatite sulphur data to place constraints upon the oxidation state of the magma (Barth and Dorais, 2000). 3) biotite data to estimate the fugacities of HF and HCl of the medium from which they precipitated (Munoz, 1984), and, 4) coupled apatite and biotite data provide alternative fugacity (Loferski and Ayuso, 1995) and temperature (Zhu and Sverjensky, 1992) estimates. The analysis further demonstrate the usefulness of apatite and biotite chemistry in detailing the sulphur and halogen chemistry of magmatic intrusions, in this case associated with an economic porphyry copper deposit.

8.2 GEOLOGICAL BACKGROUND

The Morenci intrusive sequence, which consists progressively younger stocks of diorite, quartz monzonite, and granite porphyry was emplaced into a Precambrian basement complex and Paleozoic-Mesozoic sedimentary rocks during the Laramide orogeny.

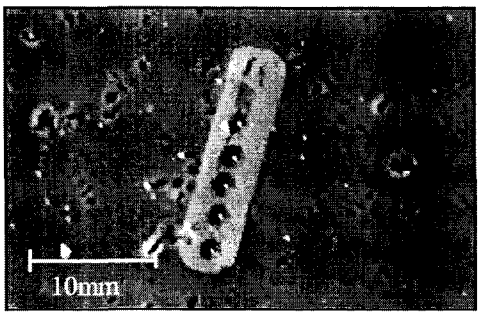

FIGURE 8.1. SEM photomicrograph of a quartz-included apatite. Analytical pits evident on the image correspond to analyses YGD2.1-YGD2.6 shown on Table 8.1 and described in the text..

Samples analysed in this study were taken from the younger granodiorite porphyry, the youngest member of the intrusive suite. Euhedral apatite needles, commonly measuring ~10-15μm in length, are found either towards the outer regions of quartz phenocrysts within growth zones defined by geometric arrays of fluid inclusions and solid phases or as isolated micro-crystals within the phenocryst (Fig. 8.1). Successive zones of fluid inclusions within the phenocrysts attest to crystallisation in a volatile-saturated early magma. Larger, light brown, biotite micro-phenocrysts measure up to 100 μm. These are found within the quartz phenocrysts, commonly accompanied by primary hypersaline and vapour rich inclusions, primary melt inclusions, and zircon micro-phenocrysts. The discovery of both of these included phases hosted within quartz suggests they may have escaped post-solidification, hydrothermal alteration (Roedder, 1984) and thus might record initial, primary magmatic conditions early in the crystallisation history of the Morenci intrusion.

8.2 GEOLOGICAL BACKGROUND

The Morenci intrusive sequence, which consists progressively younger stocks of diorite, quartz monzonite, and granite porphyry was emplaced into a Precambrian basement complex and Paleozoic-Mesozoic sedimentary rocks during the Laramide orogeny.

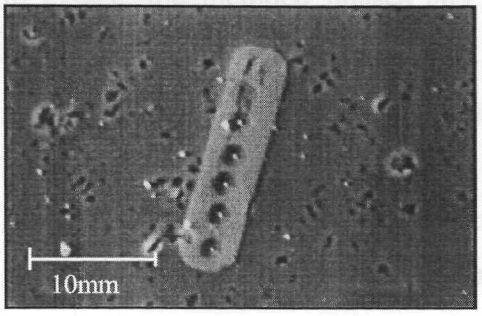

FIGURE 8.1. SEM photomicrograph of a quartz-included apatite. Analytical pits evident on the image correspond to analyses YGD2.1-YGD2.6 shown on Table 8.1 and described in the text..

Samples analysed in this study were taken from the younger granodiorite porphyry, the youngest member of the intrusive suite. Euhedral apatite needles, commonly measuring ~10-15μm in length, are found either towards the outer regions of quartz phenocrysts within growth zones defined by geometric arrays of fluid inclusions and solid phases or as isolated micro-crystals within the phenocryst (Fig. 8.1). Successive zones of fluid inclusions within the phenocrysts attest to crystallisation in a volatile-saturated early magma. Larger, light brown, biotite micro-phenocrysts measure up to 100 μm. These are found within the quartz phenocrysts, commonly accompanied by primary hypersaline and vapour rich inclusions, primary melt inclusions, and zircon micro-phenocrysts. The discovery of both of these included phases hosted within quartz suggests they may have escaped post-solidification, hydrothermal alteration (Roedder, 1984) and thus might record initial, primary magmatic conditions early in the crystallisation history of the Morenci intrusion.

8.3 ANALYTICAL METHODS

Individual quartz phenocrysts were separated by hand from the groundmass following a process of coarse crushing and set in resin under a microscope, perpendicular to the optical *c*-axis. The tops and bottoms of the crystals were then removed and the remaining cores mounted onto glass slides. Examination under an optical microscope determined the presence of included apatite or biotite crystals. Each phenocryst was then carefully ground to expose the included phases and prepared as standard polished thin sections. Once exposed, the section was then finely polished using diamond oil suspension of decreasing grade to generate a suitable finish required for microprobe analysis.

Apatites were analysed with a Cameca SX-50 microprobe at The Natural History Museum, London. Standard operating conditions were 15kV accelerating potential, 15nA beam current, 10μm beam diameter and counting time of 10-40s.

8.4 RESULTS

8.4.1 Apatite chemistry

Eleven analyses from two separate quartz-included apatite grains were obtained from the Morenci phenocrysts. Major element contents of the studied crystals are presented on Table 8.1. The halogen site of the apatites is predominantly filled by the fluor-hydroxyapatite end members, both of which are present in almost equal quantities (Fig. 8.2). X_{Cl}^{ap} generally represents <0.05 mole percent. Although the absolute fluorine contents vary considerably (0.81 – 2.04 wt%), all analyses display a significant fluorapatite end member component. Calculated hydroxyl contents are high, commonly accounting for greater that 1 wt%. OH end member concentrations (with the exception of one analysis, $X_{OH}^{ap} > 0.5$), are uncharacteristically high for apatites from granitic bodies (Deer *et al.,* 1992). Of the minor elements, Na_2O ranges between 0.15 to 0.36, MgO between 0 and 0.06, and, MnO between 0.01 and 0.27 wt%. Sr concentrations measure up to 0.52 wt%. Sulphur concentrations of sample the Morenci apatite YGD2 record a mean at about 0.5wt%, overlap many reported in the literature, and are in accordance with apatite crystallisation from I-type magmas (Sha and Chappell, 1999).

TABLE 8.1. Microprobe analysis of quartz-included apatites. OH content is calculated using wt% OH = 1.79*(1-(wt% F in apatite / 3.767)-(Cl wt% in apatite/6.809)). The mole fraction of F in apatite (X^{F}_{ap}) was calculated using wt% F in apatite/3.767 and the mole fraction of Cl in apatite (X^{Cl}_{ap}) was calculated using wt% Cl in apatite/6.809 (Piccoli and Candela, 1994).

	YGD1.1	YGD1.2	YGD1.3	YGD1.4	YGD1.5	YGD2.1	YGD2.2	YGD2.3	YGD2.4	YGD2.5	YGD2.6
F	0.81	1.78	2.04	0.92	0.93	1.42	1.49	1.43	1.45	1.41	1.23
Na_2O	0.15	0.15	0.38	0.35	0.35	0.19	0.27	0.32	0.36	0.26	0.37
MgO	0.16	0	0	0.01	0.06	0.06	0.02	0.01	0.04	0.03	0.05
Al_2O_3	0.01	0	0	0.01	0.056	0	0	0	0	0.02	0.03
SiO_2	0.23	0.14	0.21		0.76	0.51	0.42	0.4	0.38	0.45	0.47
CaO	54.29	55.89	55.03	55.91	54.4	54.79	54.27	54.04	53.9	54.85	54.07
P_2O_5	40.11	40.78	40.34	42.05	41.18	41.45	40.5	40.63	40.64	41.08	40.05
SO_3	0.21	0.02	0.31	0.44	0.32	0.21	0.45	0.55	0.61	0.51	0.53
Cl		0	0.01	0.23	0.24	0.35	0.33	0.33	0.32	0.35	0.35
MnO	0.01	0.09	0.07	0.17	0.23	0.21	0.26	0.23	0.27	0.25	0.23
FeO	0.06	0.04	0.04	0.12	0.15	0.12	0.15	0.08	0.17	0.16	0.13
SrO	0.52	0.19	0.51	0.12	0.08	0.12	0.09	0.05	0.11	0.07	0.01
BaO	0.07	0	0.04	0	0	0.1	0.13	0.02	0.03	0	0.06
Ce_2O_5	0.2	0.21	0.36	0.33	0.21	0.19	0.23	0.24	0.22	0.29	0.29
OH	1.40	0.94	0.81	1.29	1.28	1.02	0.99	1.02	1.01	1.02	1.11
Total	98.48	99.33	99.35	101.94	99.01	99.76	98.65	98.36	98.54	99.75	97.88
X_F^{ap}	0.215	0.4725	0.5415	0.2442	0.2469	0.377	0.3955	0.3796	0.3849	0.3743	0.3265
X_{Cl}^{ap}	0	0	0.0015	0.0338	0.0352	0.0514	0.0485	0.0485	0.047	0.0514	0.0514
X_{OH}^{ap}	0.785	0.5275	0.457	0.722	0.7179	0.5716	0.556	0.5719	0.5681	0.5743	0.6221

Apatites from porphyry copper settings are commonly relatively Cl-rich hydroxy-fluorapatites, with Cl contents ranging between 0.7 and 2.5% and OH between 0.61 and 0.99wt% (Williams and Cesbron, 1977). Cl and OH contents of apatites from Morenci vary between 0 and 0.35wt% and 0.81 and 1.4wt% respectively. Depleted Cl and enriched OH concentrations, as recorded in the apatites from Morenci, suggest either, 1) the precipitating medium was also comparatively Cl poor, or, 2) hydrothermal alteration of existing Cl or F-rich microphenocryst has generated an OH enriched crystal (Boudreau and McCallum, 1990; Rendon-Angeles *et al.*, 2000). Crystallisation from a Cl poor magma may be associated with the progressive Cl depletion during magmatic evolution (Boudreau et al., 1995) due to an increased partitioning of Cl into the exsolved aqueous fluid (Dilles, 1987).

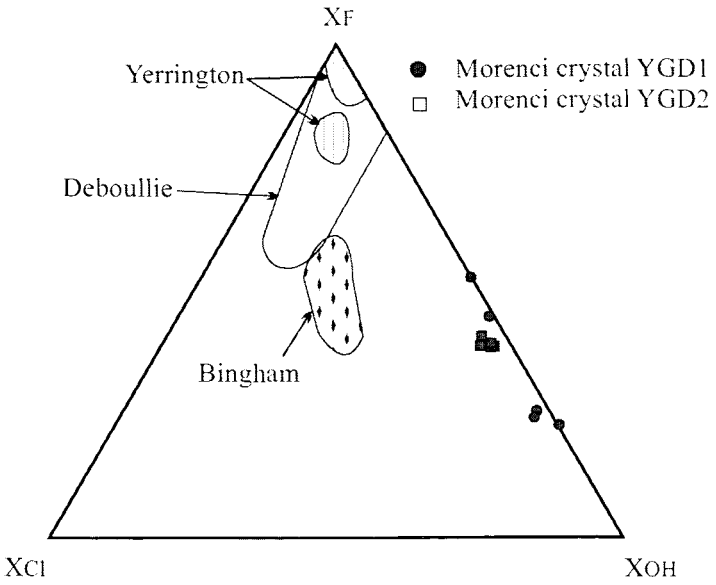

FIGURE 8.2. Compositions of quartz-included apatites shown relative to the end-member components chlorapatite (Cl), fluorapatite (F), and hydroxylapatite (OH). Shown for reference is the range of apatite compositions from Yerrington (Dilles, 1987), Bingham (Parry et al., 1978), and Deboullie (Loferski and Ayuso, 1995).

8.4.2 Magmatic fO_2

Magmatic oxidation-state is critical to the generation of an economic porphyry copper deposit. Because oxidised sulphur (SO_4^{2-}) substitutes easily for $P_4O_3^-$ in the apatite structure, it has been suggested that apatite sulphur contents may record oxidisation state and sulphur content of the precipitating magma (Luhr *et al.*, 1984; Peng *et al.*, 1997; Streck and Dilles, 1998). Early crystallisation under oxidising, sulphur-saturated conditions leads to the crystallisation of sulphur-rich apatite. 0.31wt% SO_3 was recorded in apatite coexisting with magmatic anhydrite (Barth and Dorais, 2000). This figure is less than the SO_3 content determined for Morenci apatites (range between 0.21-0.61, mean of YGD2 at about 0.5wt%) which suggests Morenci apatites crystallised under similar, anhydrite saturated, highly oxidising conditions. Such conditions are expected of a magma associated with porphyry copper mineralisation as these systems typically form at high oxygen fugacities (Loferski and Ayuso, 1995).

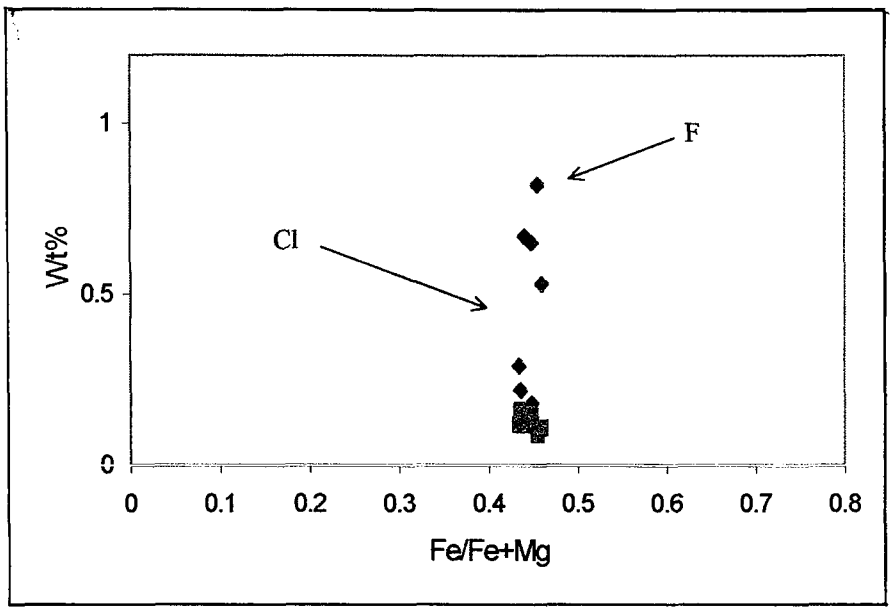

FIGURE 8.3. Range of fluorine and chlorine contents of quartz-included biotites from Morenci shown with respect to Fe/(Fe+Mg).

8.4.3 Apatite-biotite geothermometry

Armstrong (Unpublished PhD thesis; Univ. of Southampton, 1999,) presented chemical analysis of quartz-included biotite microphenocrysts from the Younger Granodiorite Porphyry, Morenci. These biotite data are reproduced on Table 8.2. Incorporating the apatite data generated for this study with the data on biotite chemistry, an estimate of the temperature of the system can be made using the apatite-biotite thermometer. Apatite-biotite geothermometry relies on the dependence of the biotite Mg/Fe ratio during the incorporation of F into that phase (Zhu and Sverjensky, 1992). F-OH exchange between end member biotite and apatite compositions can be expressed by:

$$1/2KMg_3AlSi_3O_{10}F_2 + Ca_5(PO_4)_3(OH) = 1/2KMg_3AlSi_3O_{10}(OH)_2 + Ca_5(PO_4)_3(F)$$

(F)biotite (OH)apatite = (OH)biotite (F)apatite

and a partition coefficient for the above reaction described by:

$$K_D = (X_F/X_{OH})^{apatite}/(X_F/X_{OH})^{biotite}$$

where X_F and X_{OH} represent the mole fraction F or OH in apatite or biotite respectively. Applying this to quartz-included biotite-apatite pairs found in the Morenci quartz phenocrysts at an estimated pressure of 2kbar (a crude pressure estimate is deemed viable

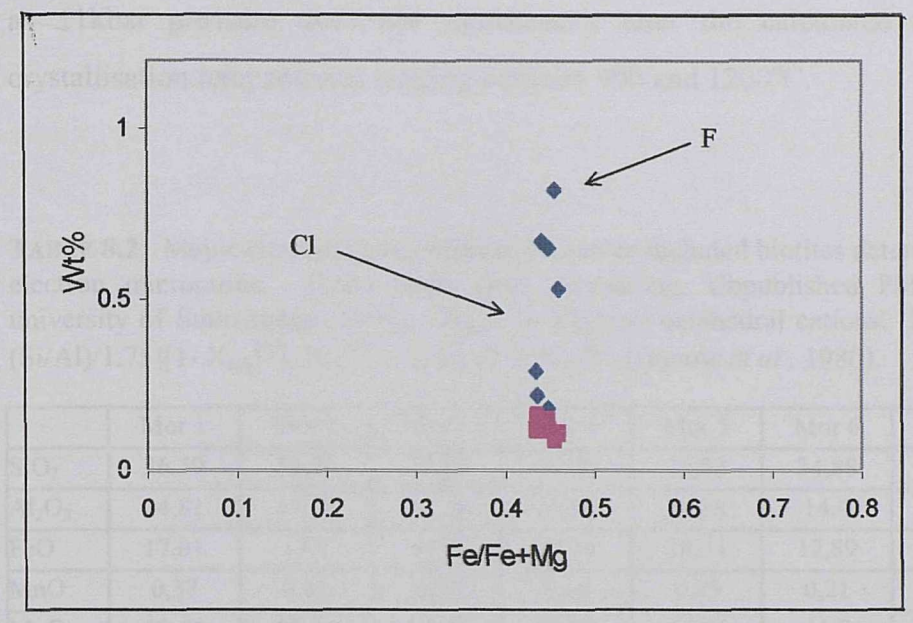

FIGURE 8.3. Range of fluorine and chlorine contents of quartz-included biotites from Morenci shown with respect to Fe/(Fe+Mg).

8.4.3 Apatite-biotite geothermometry

Armstrong (Unpublished PhD thesis; Univ. of Southampton, 1999,) presented chemical analysis of quartz-included biotite microphenocrysts from the Younger Granodiorite Porphyry, Morenci. These biotite data are reproduced on Table 8.2. Incorporating the apatite data generated for this study with the data on biotite chemistry, an estimate of the temperature of the system can be made using the apatite-biotite thermometer. Apatite-biotite geothermometry relies on the dependence of the biotite Mg/Fe ratio during the incorporation of F into that phase (Zhu and Sverjensky, 1992). F-OH exchange between end member biotite and apatite compositions can be expressed by:

$$1/2KMg_3AlSi_3O_{10}F_2 + Ca_5(PO_4)_3(OH) = 1/2KMg_3AlSi_3O_{10}(OH)_2 + Ca_5(PO_4)_3(F)$$

$$\text{(F)biotite} \quad \text{(OH)apatite} \quad = \quad \text{(OH)biotite} \quad \text{(F)apatite}$$

and a partition coefficient for the above reaction described by:

$$K_D = (X_F/X_{OH})^{apatite}/(X_F/X_{OH})^{biotite}$$

where X_F and X_{OH} represent the mole fraction F or OH in apatite or biotite respectively. Applying this to quartz-included biotite-apatite pairs found in the Morenci quartz phenocrysts at an estimated pressure of 2kbar (a crude pressure estimate is deemed viable

as ±1kbar pressure does not significantly alter the calculated temperatures), yields crystallisation temperatures ranging between 900 and 1200°C.

TABLE 8.2. Major element concentrations in quartz-included biotites determined by electron microprobe. (Data taken from Armstrong, Ubpublished PhD thesis, university of Suthampton, 1999). X_{Mg}^{biot} = Mg/sum octahedral cations. X_{sid} = [3-(Si/Al)/1.75][1- X_{Mg}^{bio}], X_{an}^{biot} = 1-(X_{Mg}^{bio} + X_{sid}^{bio}) (Gunow *et al.*, 1980).

	Mor 1	Mor 2	Mor 3	Mor 4	Mor 5	Mor 6	Mor 7
SiO_2	36,59	36,26	35,27	37,98	35,93	34,88	37,66
Al_2O_3	14,81	14,59	14,29	15,96	14,38	14,4	15,57
FeO	17,01	17,7	17,79	17,26	18,24	17,89	17,72
MnO	0,37	0,31	0,34	0,16	0,25	0,21	0,23
MgO	12,44	12,22	12,24	12,52	12,24	11,8	12,62
CaO	0	0	0	0	0	0,03	0
Na_2O	0,22	0,17	0,21	0,18	0,17	0,17	0,15
F	0,29	0,18	0,65	0,22	0,82	0,53	0,67
Cl	0,12	0,15	0,12	0,16	0,09	0,11	0,13
H_2O	5,95	6,28	7,4	3,95	7,13	9,2	4,99
Total	94,05	93,72	92,6	96,05	92,87	90,8	95,01
Si	5,248	5,203	4,970	5,515	5,019	4,782	5,324
Al	2,503	2,467	2,373	2,731	2,367	2,327	2,594
Fe	2,040	2,124	2,096	2,096	2,131	2,051	2,095
Mn	0,045	0,038	0,041	0,020	0,030	0,024	0,028
Mg	2,660	2,614	2,571	2,710	2,550	2,412	2,660
F	0,132	0,817	0,290	0,101	0,362	0,230	0,300
Cl	0,026	0,032	0,025	0,035	0,019	0,022	0,027
OH	2,846	3,005	3,477	1,912	3,321	4,206	2,352
F/(F+Cl)	0,707	0,545	0,844	0,579	0,902	0,828	0,838
sum oct ions	4,745	4,775	4,708	5,071	4,709	4,487	4,782
X_F^{biot}	0,046	0,027	0,080	0,051	0,102	0,054	0,116
X_{Cl}^{biot}	0,019	0,023	0,015	0,037	0,011	0,011	0,022
X_{OH}^{biot}	0,936	0,950	0,906	0,912	0,887	0,935	0,862
log X_F/X_{cl}^{biot}	0,383	0,079	0,734	0,138	0,960	0,683	0,712
X_{Fe}^{biot}	0,719	0,725	0,724	0,726	0,727	0,732	0,725
X_{Mg}^{biot}	0,561	0,547	0,546	0,534	0,541	0,537	0,556
X_{sid}^{biot}	0,445	0,475	0,484	0,451	0,495	0,493	0,447

8.4.4 Estimated pre-eruption halogen contents

The method of Piccoli and Candela (1994) enables the calculation of the temperature at which apatite saturates in the crystallising melt, and an approximation of the Cl and F contents of a magma and associated aqueous phase in equilibrium with the apatite-melt assemblage to be made. Applying this method to the Morenci magmas yields apatite saturation at 956°C.

TABLE 8.3. Calculated compositions of the melt and associated magmatic volatile phase at apatite saturation temperature. The ratio f_{HCl}/f_{H2O} was calculated using the equations of Piccoli et al. (1999)

	YGD2.1	YGD2.2	YGD2.3	YGD2.4	YGD2.5	YGD2.6
WR SiO_2	73.9	73.9	73.9	73.9	73.9	73.9
WR P_2O_5	0.04	0.04	0.04	0.04	0.04	0.04
Temp (°C)	950	950	950	950	950	950
Wt% Cl^{ap}	0.35	0.33	0.33	0.32	0.35	0.35
Wt% OH^{ap}(c)	1.01	0.99	1.02	1.02	1.02	1.01
C_{aq}^{Cl}	11700	11285	11016	10754	11685	10598
C_{melt}^{Cl} (at AST)	330	318	310	303	329	299
C_{aq}^{F} (at AST)	5	5	5	5	5	4
C_{melt}^{F} (at AST)	28	30	28	28	27	22
f_{HCl}/f_{H2O}	0.0005	0.0004	0.0004	0.0004	0.0005	0.0004

The relationship between the ratio of HCl to ΣCl in the melt-vapour phase has been experimentally determined to rely heavily on the pressure of the system (Shinohara et al., 1989). Piccoli and Candela (1994) used this, along with thermodynamic data on the solubility of apatite (Harrison and Watson, 1984) to calculate the concentration of Cl (C_{Cl}^{MVP}) and F (C_F^{MVP}) in magmatic volatile phase using:

$$C_{Cl}^{MVP} = [(X_{Cl}^{ap}/X_{OH}^{ap})*([3.54 \times 10^7]/18)*[(1/10^{[0.04661+(2535/T)-(0.0303*(P-1))/T)]})/ 10^{[-0.63-0.00035 \times P]}]]$$

$$C_F^{MVP} = [(X_F^{ap}/X_{OH}^{ap})*([1.90 \times 10^7]/18)*[(1/(10^{[0.18219+(5301.1/T)-(0.00360*(P-1))/T)]}]]$$

Where X_P^{ap} is the mole fraction of the subscripted element p in apatite, T is the temperature of apatite saturation (Kelvin) and P is the pressure of the system (bars). Additionally, the

concentration of Cl and F in the melt (C_{Cl}^{M} and C_{F}^{M} respectively) co-existing with this magmatic volatile phase may be calculated using:

$$C_{Cl}^{M} = \frac{[(X_{Cl}^{ap}/X_{OH}^{ap})*([3.54 \times 10^{7}]/18)*[(1/(10^{[0.04661+(2535/T)-(0.0303*(P-1)/T)]}]]}{[D_{Cl}^{vap/liq} \times 10^{[-0.63-0.00035 \times P]}]}$$

$$C_{F}^{M} = \frac{[(X_{F}^{ap}/X_{OH}^{ap})*([1.90 \times 10^{7}]/18)*[(1/10^{[0.18219+(5301.1/T)-(0.00360*(P-1)/T)]})]}{D_{F}^{vap/liq}}$$

Where the additional component $D_{M}^{vap/liq}$ is the partition coefficient between liquid and vapour of the subscripted element *M*.

Owing to the regularity of the elemental data from the sample, calculations were performed on uniquely crystal YGD2 (Fig. 8.1; Table 8.1). These calculations suggest that Cl content in the YGD melt and associated MVP were approximately 300 ppm and 11000 ppm respectively, at apatite saturation (Table 8.3). Assuming incompatibility of the halogens prior to apatite saturation temperature estimated F contents of the melt and MVP at apatite saturation are approximately 30 and 6 ppm respectively.

Unfortunately, significant variability in Cl and F concentrations obtained following a study of melt inclusions found in quartz phenocrysts from Morenci (Armstrong, 1999. Unpub. PhD thesis. Univ. Southampton) renders comparison between halogen concentrations calculated by the two methods impossible. Cl contents of the Morenci melt yielded by calculations using apatite data are in reasonable agreement with melt Cl concentrations measured from melt inclusions associated with porphyry-molybdenum mineralisation (Lowestern, 1994b).

8.4.5 Composition of the precipitating medium

Experimental studies have led to a greater understanding of the partitioning behaviour of Cl, F, and OH between halogen bearing phases and the coexisting fluid. Burnham et al. (1969) published experimentally determined values for the fugacity of water at a variety of pressures and temperatures found within the Earth. Using this, the fugacity of HF (f_{HF}) and HCl (f_{HCl}) in a fluid, at a known pressure and temperature, can be estimated using experimental data on the partitioning of these phases between either apatite (Korzhinskii, 1981) or biotite (Gunow et al., 1980; Munoz and Swenson, 1981) and the fluid phase.

TABLE 8.4. Fugacity ratios of the precipitating meduim calculated using apatite halogen data (Table 8.1) at a pressure of 2kbar, at a temperature of 950°C. These parameters suggest f_{H2O} = 2000bars (Birnham et al., 1969), $\log K_E^{Cl/OH}$ = -4.3, and $\log K_E^{F/OH}$ = -3.13 (Korzhinskii (1981).

				Apatite YGD sample							
	1.1	1.2	1.3	1.4	1.5	2.1	2.2	2.3	2.4	2.5	2.6
X_{Cl}^{ap}/X_{OH}^{ap}	0.43	0	0.004	0.04	0.05	0.09	0.08	0.08	0.08	0.09	0.08
$\log(f_{HCl}/f_{H2O})$	-2.76	0	-0.71	-1.79	-1.8	-2.08	-2.07	-2.06	-2.0	-2.08	-2.06
f_{HCl} (bars)	0.76	0	0.01	0.06	0.07	0.13	0.13	0.12	0.11	0.13	0.12
X_F^{ap}/X_{OH}^{ap}	0.93	0.90	1.18	0.33	0.34	0.66	0.71	0.66	0.67	0.65	0.52
f_{HF} (bars)	0.25	0.11	0.08	0.29	0.28	0.15	0.14	0.14	0.14	0.15	0.19
$\log(f_{H2O}/f_{HCl})$	3.40	0	5.54	4.46	4.41	4.17	4.18	4.19	4.25	4.17	4.21
$\log(f_{H2O}/f_{HF})$	3.89	4.25	4.37	3.83	3.83	4.12	4.15	4.12	4.13	4.11	4.01
$\log(f_{HF}/f_{HCl})$	-0.48	0	1.16	0.63	0.57	0.04	0.03	0.07	0.11	0.05	0.19

8.4.5.1 Apatite

Korzhinskii, (1981) showed that $\log (f_{HCl}/f_{H2O})^{fluid}$ or $\log (f_{HF}/f_{H2O})^{fluid}$, display a linear relationship with the log ratio of the mole fractions of the appropriate apatite end members, (i.e. $\log X_{Cl}^{ap}/X_{OH}^{ap}$ or $\log X_F^{ap}/X_{OH}^{ap}$) and equilibrium constants (K_E,) can be defined for both the Cl-OH and the F-OH substitutional systems in apatite by:

$$K_E^{Cl/OH} = [(f_{HCl})(a_{OH\text{-}Ap})]/[(f_{H2O})(a_{Cl\text{-}Ap})].$$

Korzhinskii (1981) also presented experimentally determined expressions for both $K_E^{Cl/OH}$ and $K_E^{F/OH}$ as a function of P and T. If ideal solid solution between chlor-, hydroxyl- and fluorapatite end members is assumed, then apatite composition can be combined with the

appropriate K_E to give values for (f_{HCl}/f_{H2O}) and log (f_{HF}/f_{H2O}). f_{HCl} and f_{HF} may then be extracted using published the water fugacities at the appropriate P-T conditions (Burnham et al., 1969). Calculated fugacity ratios witnessed by the apatite crystal YGD2 if crystallisation at 950°C is assumed show $\log(f_{H2O})/(f_{HCl})$ = 4.17 to 4.25, $\log(f_{H2O})/(f_{HF})$ = 3.84 to 4.15, and $\log(f_{HF})/f_{HCl})$ = 0.03 and 0.11 (Table 8.4).

TABLE 8.5. Halogen fugacities in the precipitating fluid calculated in this study using biotite compositional data (Armstrong. Unpubl. PhD thesis. Univ. of Southampton, 1999), and the equations of Munoz (1992), outlined in the text. Calculations were carried out assuming biotite crystallisation at 950°C and at 2kbar.

	Mor 1	Mor 2	Mor 3	Mor 4	Mor 5	Mor 6	Mor 7
F (wt%)	0.29	0.18	0.65	0.22	0.82	0.53	0.67
Cl (wt%)	0.12	0.15	0.12	0.16	0.09	0.11	0.13
H_2O (wt%)	5.95	6.28	7.4	3.95	7.13	9.2	4.99
X_F^{biot}	0.04	0.02	0.07	0.05	0.10	0.05	0.11
X_{OH}^{biot}	0.93	0.95	0.90	0.91	0.88	0.93	0.86
X_{Cl}^{biot}	0.01	0.22	0.01	0.03	0.01	0.01	0.02
X_{Mg}^{biot}	0.56	0.54	0.54	0.53	0.54	0.53	0.55
$\log(f_{H2O}/f_{HCl})$	3.73	3.73	3.73	3.72	3.72	3.72	3.73
$\log(f_{H2O}/f_{HF})$	4.53	4.75	4.26	4.45	4.14	4.44	4.09
$\log(f_{HF}/f_{HCl})$	-0.94	-1.22	-0.57	-1.14	-0.33	-0.60	-0.60

8.4.5.2 Biotite

Fluorine-hydroxyl exchange in biotites is dependant upon the Mg/(Fe+Mg) ratio, and aluminium content (Gunow et al., 1980) whereas chlorine-hydroxyl exchange is dependant upon Mg/(Mg+Fe) ratio (Munoz and Swenson, 1981). The mole fraction of phlogopite, annite and siderophllite components of biotite solid solutions can be related to biotite F:OH ratio, and to the fugacity ratio H_2O:HF of the coexisting aqueous fluid (Gunow et al., 1980). Munoz (1984) adopted this formulation for the activity constants for the reciprocal exchange reaction:

$$\text{OH-phlog} + \text{F ann} = \text{F phlog} + \text{OH ann}$$

which assumes complete disorder of Fe and Mg on the M1 and M2 sites and of OH and F on the anion sites. Munoz (1992) described how F and Cl contents of magmatic biotites can be used to infer halogen fugacity ratios in the associated magma or fluid at the time of crystallisation using:

$$\log(f_{H2O}/f_{HF})^{fluid} = 1000/T(2.37+1.1(X_{Mg})^{biot}) + 0.43-\log(X_F/X_{OH})^{bio}$$

$$\log(f_{H2O}/f_{HCl})^{fluid} = 1000/T(1.15+0.55(X_{Mg})^{biot}) + 0.68-\log(X_{Cl}/X_{OH})^{bio}$$

$$\log(f_{HF}/f_{HCl})^{fluid} = -1000/T(1.22+1.65(X_{Mg})^{biot}) + 0.25+\log(X_F/X_{Cl})^{bio}$$

where X_{Mg}, X_F and X_{Cl} represent the mole fraction Mg, F and Cl in the halogen site of biotite, respectively, $(X_{Mg})^{biot}$ is the sum of octahedral cations and T is the temperature of the halogen exchange, in Kelvin.

The composition of quartz-included biotites from the Younger Granodiorite Porphyry are given in Armstrong (Unpubl. PhD thesis, Univ. of Southampton, 1999). In this study, the fugacity ratios which correlate with biotite crystallisation at 950°C were calculated using the relevant equations above (Table 8.5). Calculated fugacity ratios of the Morenci biotites, crystallised from a hydrothermal fluid at 950°C, show $\log(f_{H2O})/(f_{HCl}) = 3.7$, $\log(f_{H2O})/(f_{HF}) = 4.1$ to 4.8, and $\log(f_{HF})/f_{HCl}) = -1.2$ and -0.3

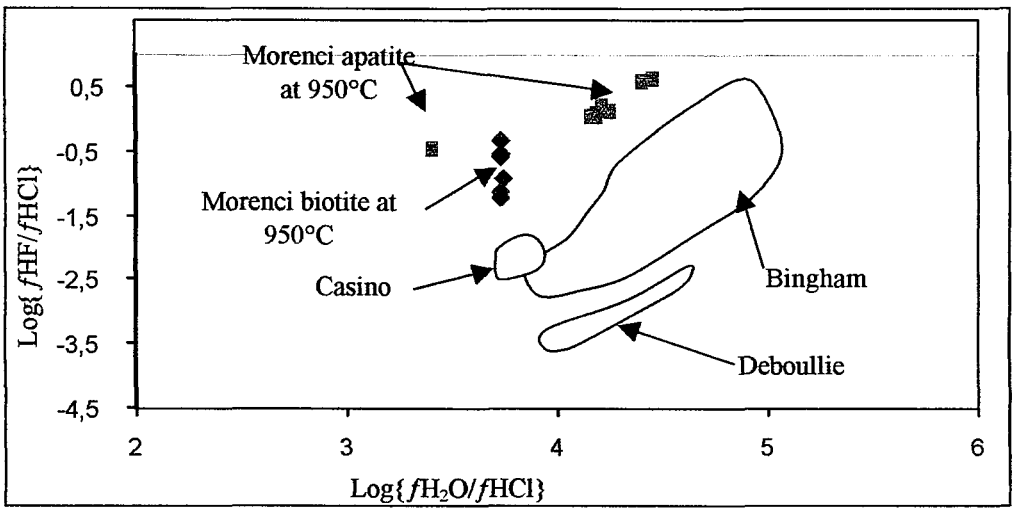

FIGURE 8.4. $Log(f_{H2O})/(f_{HCl})$ vs. $log(f_{HF})/f_{HCl})$ calculated using both biotite and apatite compositions

8.4.6 Comparison with fugacity ratios from other porphyry copper systems

Selby and Nesbitt (2000) complied $log(f_{H2O})/(f_{HCl})$, $log(f_{H2O})/(f_{HF})$, and $log(f_{HF})/f_{HCl})$ data from intrusions associated with the Bingham (Bowman et al., 1987; Lanier et al., 1978; Parry et al., 1978), Santa Rita (Jacobs and Parry, 1979b), Los Pelambres (Taylor, 1983), Hanover (Jacobs and Parry, 1979a) and Deboulle (Loferski and Ayuso, 1995), with their own data from the Casino and Babine Lake porphyry copper systems. Figures 8.4 and 8.5 show fugacity data from Morenci (Tables 8.4 and 8.5) plotted on to $log(f_{H2O})/(f_{HCl})$ vs $log(f_{HF})/f_{HCl})$ and $log(f_{H2O})/(f_{HCl})$ vs $log(f_{H2O})/f_{HF})$ with data from the other porphyry copper systems (Selby and Nesbitt, 2000). In Figure 8.4, which shows $log(f_{H2O})/(f_{HCl})$ and $log(f_{HF})/f_{HCl})$ data obtained following fugacity calculations from apatite and biotite, performed at 950°C, reasonable correlation between the values of $log(f_{H2O})/(f_{HCl})$ and $log(f_{HF})/f_{HCl})$ obtained using the two techniques is noted. Fugacity data calculated using both techniques show the data to lie within the field associated with other mineralised systems. Figure 8.5 shows plots of $log(f_{H2O})/(f_{HCl})$ and $log(f_{H2O})/f_{HF})$ ratios for Morenci. Fugacity ratios calculated at 950°C, using apatite (Table 8.4) and biotite (Table 8.5) data are in reasonable accordance with each other, although, when plotted against those from other porphyry copper occurrences, the data from Morenci are separated from the other data.

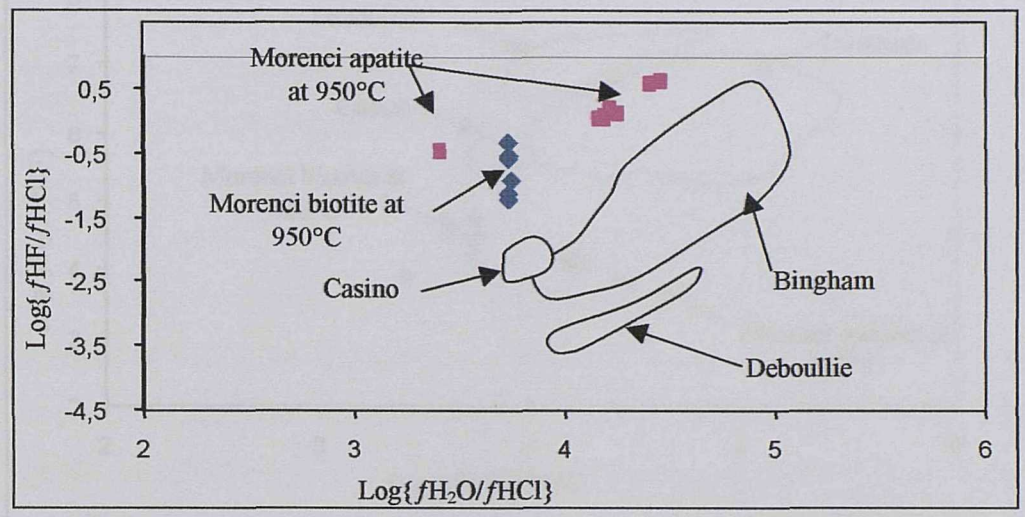

FIGURE 8.4. Log(f_{H2O})/(f_{HCl}) vs. log(f_{HF})/f_{HCl}) calculated using both biotite and apatite compositions

8.4.6 Comparison with fugacity ratios from other porphyry copper systems

Selby and Nesbitt (2000) complied log(f_{H2O})/(f_{HCl}), log(f_{H2O})/(f_{HF}), and log(f_{HF})/f_{HCl}) data from intrusions associated with the Bingham (Bowman et al., 1987; Lanier et al., 1978; Parry et al., 1978), Santa Rita (Jacobs and Parry, 1979b), Los Pelambres (Taylor, 1983), Hanover (Jacobs and Parry, 1979a) and Deboulle (Loferski and Ayuso, 1995), with their own data from the Casino and Babine Lake porphyry copper systems. Figures 8.4 and 8.5 show fugacity data from Morenci (Tables 8.4 and 8.5) plotted on to log(f_{H2O})/(f_{HCl}) vs log(f_{HF})/f_{HCl}) and log(f_{H2O})/(f_{HCl}) vs log(f_{H2O})/f_{HF}) with data from the other porphyry copper systems (Selby and Nesbitt, 2000). In Figure 8.4, which shows log(f_{H2O})/(f_{HCl}) and log(f_{HF})/f_{HCl}) data obtained following fugacity calculations from apatite and biotite, performed at 950°C, reasonable correlation between the values of log(f_{H2O})/(f_{HCl}) and log(f_{HF})/f_{HCl}) obtained using the two techniques is noted. Fugacity data calculated using both techniques show the data to lie within the field associated with other mineralised systems. Figure 8.5 shows plots of log(f_{H2O})/(f_{HCl}) and log(f_{H2O})/f_{HF}) ratios for Morenci. Fugacity ratios calculated at 950°C, using apatite (Table 8.4) and biotite (Table 8.5) data are in reasonable accordance with each other, although, when plotted against those from other porphyry copper occurrences, the data from Morenci are separated from the other data.

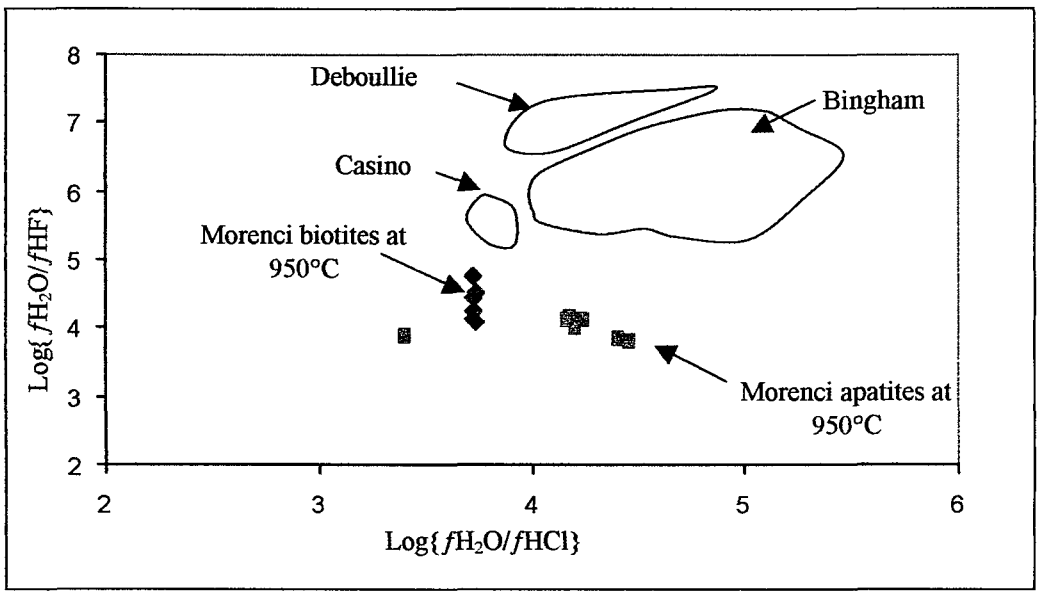

FIGURE 8.5. Log(f_{H2O})/(f_{HCl}) vs. log(f_{H2O})/f_{HF}) calculated using both biotite and apatite compositions

Selby and Nesbitt (2000) showed that although log(f_{H2O})/(f_{HCl}) and log(f_{HF})/f_{HCl}) ratios of the hydrothermal fluids associated with potassic and phyllic alteration at Bingham, Santa Rita, Los Pelambres, Hanover, Deboulle, Casino and Babine Lake porphyry copper systems were of similar value, significant variation exists in ration of log(f_{H2O})/(f_{HF}). They noted that the log(f_{H2O})/(f_{HF}) ratios for fluids associated with porphyry copper mineralisation were significantly higher than those associated with porphyry molybdenum deposits. Measured log(f_{H2O})/(f_{HF}) ratios for the Henderson porphyry molybdenum deposit fell between 4.3 and 4.6 (Selby and Nesbitt, 2000). Magmas associated with porphyry molybdenum deposits are typically F-rich, more silicic and more extensively differentiated than those associated with porphyry copper mineralisation (Loferski and Ayuso, 1995). F enrichment in porphyry molybdenum magmas may be inherited from the source, either by previous melting or by significant dehydration of the source during metamorphism. Alternatively, high F/Cl ratios may be the result of early vapour saturation and exsolution, a process which results in significant loss of Cl from the system.

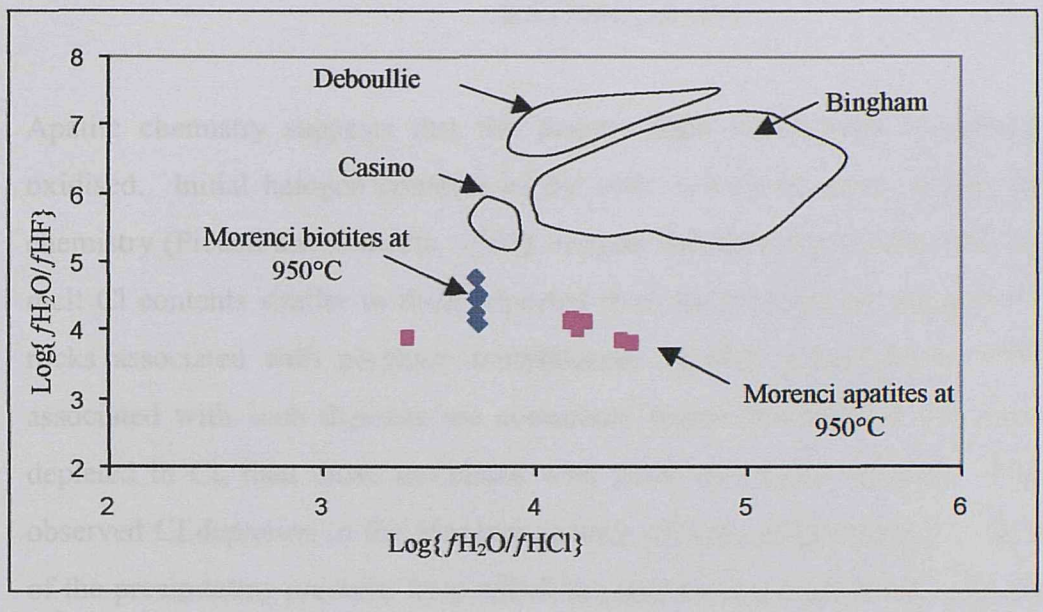

FIGURE 8.5. Log(f_{H2O})/(f_{HCl}) vs. log(f_{H2O})/f_{HF}) calculated using both biotite and apatite compositions

Selby and Nesbitt (2000) showed that although log(f_{H2O})/(f_{HCl}) and log(f_{HF})/f_{HCl}) ratios of the hydrothermal fluids associated with potassic and phyllic alteration at Bingham, Santa Rita, Los Pelambres, Hanover, Deboulle, Casino and Babine Lake porphyry copper systems were of similar value, significant variation exists in ration of log(f_{H2O})/(f_{HF}). They noted that the log(f_{H2O})/(f_{HF}) ratios for fluids associated with porphyry copper mineralisation were significantly higher than those associated with porphyry molybdenum deposits. Measured log(f_{H2O})/(f_{HF}) ratios for the Henderson porphyry molybdenum deposit fell between 4.3 and 4.6 (Selby and Nesbitt, 2000). Magmas associated with porphyry molybdenum deposits are typically F-rich, more silicic and more extensively differentiated than those associated with porphyry copper mineralisation (Loferski and Ayuso, 1995). F enrichment in porphyry molybdenum magmas may be inherited from the source, either by previous melting or by significant dehydration of the source during metamorphism. Alternatively, high F/Cl ratios may be the result of early vapour saturation and exsolution, a process which results in significant loss of Cl from the system.

8.5 CONCLUSIONS

Apatite chemistry suggests that the magma from which they crystallised was highly oxidised. Initial halogen contents of the melt, calculated using apatite and whole rock chemistry (Piccoli and Candela, 1994), suggest that the crystallising melt contained initial melt Cl contents similar to those reported from melt inclusions recovered from intrusive rocks associated with porphyry molybdenum deposits (Lowenstern, 1994b). Magmas associated with such deposits are commonly highly fractionated, and accordingly more depleted in Cl, than those associated with porphyry copper deposits. The cause of the observed Cl depletion in the Morenci apatites remains problematical. Log fugacity ratios of the precipitating medium from which the apatites crystallised were calculated using the apatite data obtained in this study. Calculated ratios of $\log(f_{H2O})/(f_{HCl})$ and $\log(f_{HF})/(f_{HCl})$ were similar to those reported from other porphyry copper settings, while log of $\log(f_{H2O})/(f_{HF})$ varied significantly. Similar variability in $\log(f_{H2O})/(f_{HF})$ ratios has been reported by other authors (Selby and Nesbitt, 2000). Log fugacity ratios were subsequently calculated using major element biotite compositional data from the same intrusion (Armstrong, Unpubl. PhD thesis. Univ of Southampton, 1999). Values generated using biotite data are in good agreement with those calculated using apatite chemistry.

Chapter 9

CONCLUSIONS

9 Conclusions

In situ micro-infrared spectroscopic investigation of hydrothermal vein quartz known to have anomalous dD signatures has identified two hydrogen reservoirs. In samples that generate an isotopic signature in accordance with that anticipated for the accepted model of quartz crystallization, submicroscopic aggregates of liquid water are the dominant hydrous species. Samples which generate an anomalous dD signature contain, in addition to liquid water, structurally incorporated hydrous species associated with impurity cations. High temperature infrared spectra obtained during in situ stepped heating experiments, coupled with infrared analysis at 25°C, demonstrate that hydrogen liberated between 300°C and 500∞C is chiefly molecular, liquid water. Hydrogen liberated at temperatures greater than 500°C is dominantly associated with specific structurally incorporated cation defects. Since both defect hydrogen and molecular water are contemporaneously incorporated from the precipitating medium during crystallization, we propose that irregular dD signatures, released following decrepitation at temperatures greater than 500°C, are due to isotopically fractionated hydrogen released from interstitial OH defect sites in the quartz structure.

δD signatures obtained from stoichiometrically anhydrous minerals are generally interpreted under the assumption that the hydrogen measured comes uniquely from decrepitated fluid inclusions. The results presented in Chapter 3 suggest that δD ratios obtained from hydrothermal quartz reflect a sum of the contributions made by individual hydrogen reservoirs, each with a potentially distinctive δD signature. Thus, if the overall δD signature is attributed entirely to fluid inclusion phases, the nature of the precipitating fluid may be misinterpreted. Hydrogen extracted as molecular water at between 300°C and 500°C provides a true reflection of the hydrothermal solution associated with crystal precipitation. The possible fractionation of hydrogen isotopes into defect sites in anhydrous minerals is clearly an incredibly complex subject, but one which may be fundamental to our understanding of numerous geological situations. The subject remains one which would benefit significantly from further study. For example, TEM studies on the nature of the defect sites in quartz would help elucidate the nature of the hydrous species in the samples. Additionally, experimental investigations into the sequestering of hydrogen into quartz are necessary to establish fractionation factors for the species, and calibration of the molar absorptivity of various hydrous defects in silica would facilitate their quantification using infrared spectrsocpy. If further substantiated, the fractionation of hydrogen isotopes into

quartz will strongly influence the isotopic signature retrieved and may lead to a re-interpretation of many currently accepted models which describe numerous geological processes.

Scanned SEM-cathodoluminescence images of the quartz phenocryst enable numerous textural features associated with crystal growth to be readily distinguished, notably, significant zonation of the quartz phenocryst. Growth zones create a roughly concentric pattern around the central region of the crystal. The phenocrysts contains a rounded core of uniform, moderate luminescence intensity which may suggest ascent of a vapour-undersaturated melt into the crust. The frequent parallelism of oscillatory growth zones with the phenocryst edges suggests, 1) the observed growth textures are of magmatic primary origin, and, 2) oscillatory zoning may be caused by progressive changes in crystallisation conditions experienced during crystal growth. Within any single zone, a crystallisation sequence is initiated by a brightly luminescent interior, which progressively decreases in intensity towards a poorly luminescent exterior. The intensity of the luminescence response may also be correlated with growth morphology. A strongly luminescent response is found in regions of irregular growth which are morphologically similar to dendritic crystal growth habits.

The observed oscillatory zoning resembles chemical zoning in plagioclase. In plagioclase, such growth zones have been be attributed to variations in melt composition, growth conditions, growth rate, and diffusion controlled chemical changes between the mineral and its environment. Experimental studies suggest that, unlike feldspar, quartz crystallisation remains a function of cooling rate and is unaffected by external factors. Additionally, unlike the equilibrium partitioning of trace elements between growing plagioclase crystal and the precipitating medium, the incorporation of defects into quartz is a kinetic process that does not directly reflect the temperature or pressure of the system. Accordingly, if cathodoluminescence response in quartz is attributable to the incorporation of impurity defects in the crystal structure, a model to describe the formation of oscillatory zoning in quartz may need to be formulated around variations in the cooling rate of the system. Correlation between the observed growth patterns with those described through theoretical modelling may greatly enhance our understanding the many of processes associated with magmatic crystallisation.

Monochromatic scanned SEM-cathodoluminescence images of a magmatic quartz phenocryst elucidate numerous oscillatory growth zones. Initiated by bright luminescence, the intensity of the luminescence response becomes progressively darker towards the outer termination of a zone. The onset of the succeeding zone is heralded by a sudden, sharp return to bright luminescence. Aluminium has been frequently cited as the cause of variable cathodoluminescence response in quartz, yet concentrations of the element, measured by electron microprobe across zones of highly variable luminescence response, show little spatial variation. Micro infrared spectroscopic traverses conducted across the same region of the crystal analysed suing the electron microprobe show that concentrations of Al-OH defects within the sample show no systematic variability throughout the sample. Conversely, relative concentrations of H-OH species vary significantly. High concentrations of H-OH species are noted in regions of strongly luminescent quartz. Low H-OH contents correspond to regions of weak luminescence response. The generation of the cyclic nature of the growth zones is attributed to fluctuations in the growth rate of the crystal.

Microprobe determination of the composition of apatite and biotite microphenocrysts permit the calculation of the chemistry from which they were precipited. Calculations suggest that the magma from which they crystallised was highly oxidised. Initial halogen contents of the melt, calculated using apatite and whole rock chemistry, suggest that the crystallising melt contained initial Cl contents which are similar to those recovered from melt inclusions in intrusives associated with porphyry molybdenum deposits. Magmas associated with such deposits are commonly ore extensively differentiated, and accordingly more Cl depleted, than those associated with porphyry copper deposits. The cause of Cl depletion in the Morenci melt remains problematical. Log fugacity ratios of the precipitating medium were calculated using the apatite data obtained in this study. Calculated ratios of $\log(f_{H2O})/(f_{HCl})$ and $\log(f_{HF})/f_{HCl})$ were similar to those reported from other porphyry settings, while $\log(f_{H2O})/f_{HF})$ varied significantly. Similar variability in $\log(f_{H2O})/f_{HF})$ ratios have also been reported by other authors. Log fugacity ratios calculated using biotite data from the same intrusion generate values similar to those obtained using apatite data. Further studies to constrain the nature of the sulphur contained within apathies from porphyry-copper settings may shed further light onto the origins of the abundant sulphur observed in many porphyry copper complexes.

Chapter 10

REFERENCES

10 References

Aines, R.D., and Rossman, G.R. (1984a) Water content of mantle garnets. *Geology*, **12**, 720-723.

-. (1984b) Water in minerals? A peak in the infrared. *Journal of Geophysical Research*, **89**, 4059-4071.

Allegre, C.J., Provost, A., and Jaupart, C. (1981) Oscillatory zoning in minerals: A pathological case of crystal growth. *Nature,* **294**, 223-228.

Anderson, A.T. (1984) Probable relations between plagioclase zoning and magma dynamics, Fuego Volcano, Guatemala. *American Mineralogist*, **69**, 660-676.

Anderson Jr, A.T., Newman, S., Williams, S., N., Druitt, T.H., Skirius, C., and Stolper, E. (1989) H_2O, CO_2 and Cl in plinian and ash-flow Bishop rhyolite. *Geology,* **17,** 221-225.

Andrew, C.J. (1996) The Chelopech Au deposit, Bulgaria. *MDSG Abstracts*, Glasgow.

Armstrong, R.N. (1999) The ore forming potential of Calc Alkaline systems: A magmatic perspective. School of Ocean and Earth Science. Unpublished PhD thesis. University of Southampton, Southampton.

Aronson, J.R., Emslie, A.G., and McLinden, H.G. (1966) Infrared spectra from fine particulate surfaces. *Science,* **69,** 3463-3470.

Bacon, C.R. (1986) Magmatic inclusions in silicic and intermediate volcanic rocks. *Journal of Geophysical Research,* **91,** 6091-6112.

Bacon, C.R., Adami, L.H., and Lanphere, M.A. (1989) Direct evidence for the origin of low ^{18}O silicic magmas: Quenched samples of a magma chambers partially-fused granitoid walls, Crater Lake, Oregon. *Earth and Planetary Science Letters*, **96,** 199-208.

Bahadur, H. (1993) Hydroxyl defects and electrodiffusion (sweeping) in natural quartz crystal. *Journal of Applied Physics*, **73,** 7790-7797.

Barth, A.P., and Dorais, M.J. (2000) Magmatic anhydrite in granitic rocks: First occurrence and potential petrologic implications. *American Mineralogist*, **85,** 430-436.

Beane, R.E., and Bodnar, R.J. (1995) Hydrothermal fluids and hydrothermal alteration in porphyry copper deposits. In F.W. Pierce, Ed. Porphyry Copper Deposits of the American Cordillera, 20, p. 83-93. Arizona Geological Society Digest.

Beane, R.E., and Titley, S.R. (1981) Porphyry copper deposits. Part 2. Hydrothermal alteration and mineralization. *Economic Geology,* **75th Anniversary Volume,** 235-262.

Ben-Jacob, E., and Garik, P. (1990) The formation of patterns in non-equilbrium growth. *Nature,* **343,** 523-530.

Bodnar, R.J. (1995) Fluid inclusion evidence for a magmatic source for metals in porphyry copper deposits. In J.F.H. Thompson, Ed. Magmas, Fluids and Ore Deposits, **23,** p. 139-152. *Mineralogical Association of Canada Short Course Series.*

Bonev, I.K., Kerestedisiyan, T., Kadisiyev, A., and Andryu, K. (1998) Morphology of native gold from the Chelopetch ore deposit. *Geokhimiya, Mineralogiya i Petrologiya*, **35,** 3-16.

Boudreau, A.E., Love, C., and Prendergast, M.D. (1995) Halogen geochemistry of the Great Dyke, Zimbabwe. *Contributions to Mineralogy and Petrology,* **122,** 289-300.

Boudreau, A.E., and McCallum, I.S. (1990) Low temperature alteration of REE-rich chlorapatite from the Stillwater Complex, Montana. *American Mineralogist,* **75,** 687-693.

Bowen, N.L. (1928) The Evolution of Igneous Rocks. 332 p. Princeton University Press, Princeton N. J.

Bowman, J.R., Parry, W.T., Kropp, W.P., and Kruer, S.A. (1987) Chemical and isotopic evolution of hydrothermal solutions at Bingham, Utah. *Economic Geology,* **82,** 395-428.

Briden, J.C., Drewry, G.E., and Smith, A.G. (1974) Phanerozoic equal-area world maps. *Journal of Geology*, **82**, 555-574.

Brindley, G.W. (1980) Order and disorder in clay mineral structures. In G.W. Brindley, and G. Brown, Eds. Crystal Structures of Clay Minerals and their X-ray Identification, p. 125-195. Mineralogical Society, London.

Burnham, C.W., Holloway, J.R., and Davis, N.F. (1969) Thermodynamic properties of water up to 1000°C and 10000bars. 96 p. *Geological Society of America Special Paper.*

Burnham, C.W., and Ohmoto, H. (1980) Late-stage processes in felsic magmatism. *Mining Geology Special Issue*, **8,** 1-11.

Calas, G., and Hawthorne, F.C. (1988) Introduction to Spectroscopic Methods. In F.C. Hawthorne, Ed. Spectroscopic Methods in Mineralogy and Geology, 18, p. 1-9. Mineralogical Society of America, Washington D.C.

Candela, P.A. (1991) Physics of aqueous phase evolution in plutonic environments. *American Mineralogist,* **76,** 1081-1091.

-. (1997) A review of shallow ore-related granites: Textures, volatiles and ore metals. *Journal of Petrology,* **38,** 1619-1633.

Candela, P.A., and Blevin, P.L. (1995) Do some miariolitic granites preserve evidence of magmatic volatile phase permeability? *Economic Geology,* **90,** 2310-2316.

Candela, P.A., and Holland, H.D. (1984) The partitioning of copper and molybdenum between silicate melts and aqueous fluids. *Geochimica et Cosmochimica Acta,* **48,** 373-380.

-. (1986) A mass transfer model for copper and molybdenum in magmatic hydrothermal systems: The origin of porphyry-type ore deposits. *Economic Geology,* **81,** 1-19.

Candela, P.A., and Piccoli, P. (1995) Model ore-forming potential from melts into vapor and vapor/brine mixtures. In J.H.F. Thompson, Ed. Magma, Fluids and Ore Deposits, 23, p. 101-128. Mineralogical Association of Canada, Short Course Series.

Cashman, K.V. (1992) Groundmass crystallization of Mount St Helens dacite, 1980-1986: A tool for interpreting shallow magmatic processes. *Contributions to Mineralogy and Petrology,* **109,** 431-449.

Chalmers, J.M., Everall, N.J., Hewitson, K., Chesters, M.A., Pearson, M., Grady, A., and Ruzicka, B. (1998) Fourier transform infrared spectroscopy: some advances in techniques for characterisation and structure-property elucidations of industrial minerals. *The Analyst,* **123,** 579-586.

Channer, D.M.D., and Spooner, E.T.C. (1991) Multiple fluid inclusion generations in variably deformed quartz: Hollinger-McIntyre and Kerr Addison-Chesterville Archean Au-bearing vein systems. *Ontario Geological Survey Miscellaneous Paper*, **156,** 47-64.

Charef, A., and Sheppard, S.M.S. (1987) Pb-Zn mineralisation associated with diapirism: fluid inclusion and stable isotope (H, C, O) evidence for the origin and evolution of the fluids at Fedj-el-Adoum, Tunisia. *Chemical Geology*, **61**, 113-134.

Chernov, A.A., and Kunzetsov, V.A. (1970) Kinetics of the hydrothermal crystallization of quartz in different solutions and the absorption film hypothesis. *Soviet Physical Crystallographer*, **14,** 753-756.

Clayton, R.N., and Mayeda, T.K. (1963) The use of bromine pentafluoride in the extraction of oxygen from oxides and silicates for isotope analysis. *Geochimica Cosmochimica et Acta*, **27**, 43-52.

Cline, J.S., and Bodnar, R.J. (1991) Can economic porphyry copper mineralization be generated by a typical calc alcaline melt? *Journal of Geophysical Research,* **96**, 8113-8126.

Deer, W.A., Howie, R.A., and Zussman, J. (1992) An Introduction to the Rock Forming Minerals. Longman, Harlow.

Delineau, T., Allard, T., Muller, J.P., Barres, O., Yvon, J., and Cases, J.M. (1994) FTIR reflectance vs. EPR studies of structural iron in kaolinites. *Clays and Clay Minerals,* **42,** 308-320.

Demars, C., Pagel, M., Deloule, E., and Blanc, P. (1996) Cathodoluminescence of quartz from sandstones: Interpretation of the UV range by determination of trace element distributions and fluid inclusion P-T-X properties in authigenic quartz. *American Mineralogist,* **81,** 891-901.

Dickinson, W.W., and Millikinen, K.L. (1995) The diagenetic role of brittle deformation in compaction and pressure solution, Etjo Sandstone, Namibia. *Journal of Geology*, **103,** 339-347.

Dilles, J.H. (1987) Petrology of the Yerington Batholith, Nevada; evidence for evolution of porphyry copper ore fluids. *Economic Geology,* **82,** 1750-1789.

D'Lemos, R.S., Kearsley, A.T., Pembroke, J.W., Watt, G.R., and Wright, P. (1997) Complex growth histories in granite revealed by scanning cathodoluminescence techniques. Geological Magazine, 134(4), 549-552.

Dodd, D.M., and Fraser, D.B. (1967) Infrared studies of the variation of H-bonded OH in synthetic α-quartz. *American Mineralogist*, **52**, 149-160.

Doherty, R. (1974) Dendritic growth. In R. Brian, Ed. *Crystal Growth*, **6**, p. 576-599. Permagon Press Ltd., Oxford.

Donaldson, C.H. (1976) An experimental investigation of olivine morphology. *Contributions to Mineralogy and Petrology*, **57**, 187-213.

Donaldson, C.H., and Henderson, C.M.B. (1988) A new interpretation of round embayments in quartz crystals. *Mineralogical Magazine,* **52,** 27-33.

Dowty, E. (1980) Crystal growth and nucleation theory and the numerical simulation of igneous crystallization. In R.B. Hargraves, Ed. Physics of Magmatic Processes, p. 419-486. Princeton Univ. Press, Princeton, NJ.

Druitt, T.H., and Bacon, C.R. (1989) Petrology of the zoned magma calcalkaline chamber of Mount Mazama, Crater Lake, Oregon. *Contributions to Mineralogy and Petrology,* **101,** 245-259.

Eichelberger, J.C. (1978) Andesitic volcanism and crustal evolution. *Nature,* **275,** 21-27.

Elbaum, M., and Wettlaufer, J.S. (1993) Relation of growth and equilibrium crystal shapes. *Physical Review E,* **48,** 3180-3183.

Emmons, R.C. (1952) Selected peterogenic relationships of plagioclase. *Geological Society of America Memoirs,* **52,** 142.

Farmer, V.C. (1974a) The Infrared Spectra of Minerals. Mineralogical Society, London.

-. (1974b) The Layer Silicates. In V.C. Farmer, Ed. The Infrared Spectra of Minerals, p. 331-363. Mineralogical Society, London.

-. (1986) Infrared spectroscopy in clay mineral studies. *Clay Minerals,* **7,** 373-387.

Finch, A. A., Parsons, I., and Mingard, S. (1995) Biotites as indicators of fluorine fugacities in late-stage magmatic fluids: The Gardar Province of South Greenland. *Journal of Petrology,* **36,** 1701-1728.

Foxford, K.A. (1992) Fluid flow patterns during ore formation: Controls on mineralogical zoning, Panasqueira, Portugal, Unpub. PhD Thesis, University of Manchester, Manchester.

Fowler, A.D. (1990) Self-organized mineral textures of igneous rocks: The fractal approach. *Earth Science Reviews,* **29,** 47-55.

Gleeson, S.A., Wilkinson, J.J., Boyce, A.J., Fallick, A.E., and Stuart, F.M. (1999) On the occurrence and wider implications of anomalously low δD fluids in quartz veins, South Cornwall, England. *Chemical Geology,* **160,** 161-173.

Götze, J. (1998) Principle advantages of cathodoluminescence microscopy. *Microscopy and Microanalysis,* September Issue, 17-19.

Götze, J., Plötze, M., Fuchs, H., and Haberman, D. (1999) Defect structure and luminescence behaviour of agate - results of electron paramagnetic resonance (EPR) and cathodoluminescence (CL) studies. *Mineralogical Magazine,* **63**, 149-163.

Graham, C.M., Sheppard, S.M.S., and Heaton, T.H.E. (1980) Experimental hydrogen isotope studies-Systematics of hydrogen isotope fractionation in the systems epidote-H_2O, zoisite- H_2O and $AlO(OH)^{-}$ H_2O. *Geochimica Cosmochimica et Acta,* **44**, 353-364.

Graupner, T., Götze, J., Kempe, U., and Wolf, D. (2000) CL for characterizing quartz and trapped fluid inclusions in mesothermal quartz veins: Muruntau Au ore deposit, Uzbekistan. *Mineralogical Magazine*, **64,** 1007-1016.

Griggs, D.T., and Blacic, J.D. (1965) Quartz: Anomalous weakening of synthetic crystals. *Science*, **147,** 292-295.

Gunow, A.J., Ludington, S., and Munoz, J.L. (1980) Fluorine in micas from the Henderson molybdenite deposit, Colorado. *Economic Geology*, **75,** 1127-1137.

Gustavson, L.B., and Hunt, J.P. (1975) The porphyry copper deposit at El Salvador, Chile. *Economic Geology*, **70,** 857-921.

Guzzo, P.L., Iwasaki, F., and Iwasaki, H. (1997) Al-related centers in relation to γ-radiation. *Physics and Chemistry of Minerals*, **24,** 253-263.

Haase, C.S., Chadam, J., Feinn, D., and Ortoleva, P. (1980) Oscillatory zoning in plagioclase feldspar. *Science,* **209**, 272-274.

Hall, D.L., Bodnar, R.J., and Craig, J.R. (1991) Experimental diffusion of hydrogen into synthetic fluid inclusions in quartz. *Metamorphic Geology*, **13**, 345-355.

Halliburton, L.E., Koumvakalis, N., Markes, M.E., and Martin, J.J. (1981) Radiation effects in crystalline SiO_2: The role of aluminum. *Journal of Applied Physics*, **52,** 3565.

Hammer, V.M.F., Libowitzki, E., and Rossman, G.R. (1998) Single crystal spectroscopy of very strong hydrogen bonds in pectolite, $NaCa_2[Si_3O_8(OH)]$, and serandite, $NaMn_2[Si_3O_8(OH)]$. *American Mineralogist*, **83**, 569-576.

Harloff, C. (1927) Zonal structure in plagioclase. *Leidse Geologische Mededelingen*, **2,** 99-114.

Harris, D.M., and Anderson Jr, A.T. (1984) Volatiles H_2O, CO_2, and Cl in a subduction related basalt. *Contributions to Mineralogy and Petrology*, **87,** 120-128.

Harrison, T.M., and Watson, E.W. (1984) The behaviour of apatite during crustal anatexix: equillibrium and kinetic considerations. *Geochimica et Cosmochimica Acta,* **48,** 1467-1477.

Hattori, K., and Sato, H. (1996) Magma evolution recorded in plagioclase zoning in 1991 Pinatubo eruption products. *American Mineralogist,* **81,** 982-994.

Hauff, P.L., and Cocks, T.D. (1996) SWIR - A portable field technique for mineral exploration, p. 1-11. *Intrgrated Spectronics Technical Note.*

Hibbard, M.J. (1991) Textural anatomy of twelve magma-mixed granitoid systems. In J. Didier, and B. Barbarin, Eds. Enclaves and Granite Petrology, p. 431-444. Elsevier, Amsterdam.

Hills, E.S. (1936) Reverse and oscillatory zoning in plagioclase. *Geological Magazine*, **73,** 49-56.

Hogg, A.J.C., Sellier, E., and Jourdan, A.J. (1992) Cathodoluminescence of quartz cements in the Brent Group sandstones, Alwyn South, UK North Sea. In A.C. Morton, R.S. Hazeldine, M.R. Giles, and S. Brown, Eds. Geology of the Brent Group, 61, p. 421-440. Geological Society Special Publication, London.

Holick, P.A., and Wood, S.A. (1999) Fluid-inclusion study of the Morenci porphyry copper deposit, Arizona; metal content of the ore-forming brine. *Geological Society of America, Abstract Programs,* **31,** 404.

Holland, H.D. (1972) Granites, solutions and base metal deposits. *Economic Geology,* **67,** 281-301.

Horita, J., and Matsuo, S. (1986) Extraction and isotopic analysis of fluid inclusions in halites. *Geochemical Journal*, **20**, 261-272.

Hosaka, M., and Taki, S. (1981) Growth patterns on the rhombohedral faces of quartz crystals grown hydrothermally in NaCl and KCl solutions. *Journal of Crystal Growth,* **55,** 363-368.

Hughes, J.M., Cameron, M., and Crowley, K.D. (1990) Crystal structures of natural ternary apatites: solid solution in the $(Ca_5(PO_4)_3X$ (X=F, OH, Cl) system. *American Mineralogist,* **75,** 295-304.

Humbach, O., Fabian, H., Grzesik, U., Haken, U., and Heitmann, W. (1996) Analysis of OH absorption bands in synthetic silica. *Journal of Non-Crystalline Solids*, **203**, 16-26.

Holick, P.A. (1998) Copper-mineralizing fluids of the Morenci porphyry copper deposit, Greenlee County, Arizona., p. 115. Unpublished Masters thesis, University of Idaho, Moscow.

Holick, P.A., and Wood, S.A. (1999) Fluid-inclusion study of the Morenci porphyry copper deposit, Arizona; metal content of the ore-forming brine. *Geological Society of America, Abstract Programs,* **31,** 404.

Huston, D.L., Kamprad, J., and Brauhart, C. (1999) Definition of high temperature alteration zones with PIMA: An example from the Panorama VHMS district, central Pilbara Craton. *AGSO Resources Newsletter,* **30,** 10-12.

Ihinger, P.H., and Zink, S.I. (2000) Determination of relative growth rates of natural quartz crystals. *Nature,* **404,** 865-869.

Ishayama, D., Shinoda, K., Shimizu, T., Matsubaya, O., and Aikawa, N. (1999) Structural states and isotopic compositions in Hydrothermal quartz, Koryu deposit, Japan. *Economic Geology*, **94**, 1347-1352.

Itoh, C., Suzuki, T., and Itoh, N. (1990) Luminescence and defect formation in undensified and densified amprphous SiO_2. *Physical Review Letters B,* **41,** 3794-3799.

Jacobs, D.C., and Parry, W.T. (1979a) A comparison of the geochemistry of biotite from some basin and range stocks. *Economic Geology,* **71,** 1029-1035.

-. (1979b) Geochemistry of biotite from the Santa Rita porphyry copper deposit, New Mexico. *Economic Geology,* **73,** 860-887.

Kats, A. (1962) Hydrogen in α-quartz, *Philips Research Reports,* **17,** p. 1-31, 133-195 and 201-279.

Kazahaya, K., and Matsuo, S. (1985) A new ball-milling method for the extraction of fluid inclusions from minerals. *Geochemical Journal*, **19**, 45-54.

Kelly, W.C., and Rye, R.O. (1979) Geologic fluid inclusion and stable isotope studies of the tin tungsten deposits of Panasqueira, Portugal. *Economic Geology*, **72**, 1721-1822.

Kerr, R.C. (1995) Convective crystal dissolution. *Contributions to Mineralogy and Petrology,* **121,** 237-246.

Kirkpatrick, R.J. (1981) Kinetics of crystallization in igneous rocks. Kinetics of Geochemical Processes, *Mineralogical Society of America, Washington D. C. Special Publication,* **8,** p. 321-398.

Kita, I. (1981) A new ball mill made of pyrex glass. *Geochemical Journal*, **15**, 289-291.

Kloprogge, J.T., and Frost, R.L. (1999) Infrared emission spectroscopy of Al-pillared beidellite. *Applied Clay Science*, **15,** 431-445.

Knauth, L.P., and Eipstein, S. (1975) Hydrogen and oxygen isotope ratios in silica from the joides deep sea drilling project. *Earth and Planetary Science Letters*, **25**, 1-10.

Kodama, H., and Oinuma, K. (1963) Indentification of kaolin minerals in the presence of chlorite by x-ray diffraction and infrared absorption spectroscopy. *Clays and Clay Minerals,* **11,** 236-249.

Korzhinskii, M.A. (1981) Apatite solid solutions as indicators of the fugacity of HCl and HF in hydrothermal fluids. *Geochemistry International,* **18,** 44-60.

Koyama, H. (1980) Cathodoluminescence study of SiO_2. *Journal of Applied Physics,* **51,** 2226-2235.

Kronenberg, A.K. (1994) Hydrogen Speciation and Chemical Weakening in Quartz. In P.J. Heaney, C.T. Prewitt, and G.V. Gibbs, Eds. Silica, Physical Behavior, Geochemistry, and Materials Applications, *Reviews in Mineralogy* **29**, p. 123-176. American Mineralogical Society.

Kronenberg, A.K., Kirkby, S.H., Aines, R.D., and Rossman, G.R. (1986) Solubility and diffusional uptake of hydrogen in quartz at high water pressures: implications for hydraulic weakening. *Journal of Geophysical Research*, **91**, 12,723-12,744.

Kruse, F.A., and Hauff, P.L. (1991) Identification of illite polytype zoning in disseminated gold deposits using reflectance spectroscopy and X-ray diffraction- potential for mapping with imaging spectrometers. *IEEE Transactions on Geoscience and Remote Sensing,* **29,** 1101-1104.

Langton, J.M. (1971) Ore genesis in the Morenci-Metcalf district. *Economic Geology,* **66,** 1268.

Lanier, G., Raab, W.J., Folsom, R.B., and Muir, I.D. (1978) Alteration of equigranular monzonite, Bingham mining district, Utah. *Economic Geology,* **73,** 1270-1286.

Laporte, D. (1994) Wetting behaviour of partial melts during crustal anatexis: The distribution of hydrous silicate melts in polycrystalline aggregates of quartz. *Contributions to Mineralogy and Petrology,* **116,** 486-499.

Ledoux, R.L., and White, J.L. (1974) Infrared study of selective deuteration of kaolinite and halloysite at room temperature. *Science,* **145,** 47-49.

L'Heureux, I., and Fowler, A.D. (1994) A nonlinear dynamical model for of oscillatory zoning in plagioclase. *American Mineralogist,* **79,** 885-891.

Lipman, P., Dungan, M., and Bachmann, O. (1997) Comagmatic granophyric granite in the FishCanyon Tuff, Colorado: Implications for magma-chamber processes during a large ash-flow eruption. *Geology,* **25,** 915-918.

Loferski, P.J., and Ayuso, R.A. (1995) Petrography and mineral chemistry of the composite Deboullie pluton, northern Maine, U.S.A.: Implications for the genesis of Cu-Mo mineralization. *Chemical Geology,* **123,** 89-105.

Lofgren, G. (1980) Experimental studies on the dynamic crystallization of silicate melts. In R.B. Hargraves, Ed. Physics of Magmatic Processes, p. 487-565. Springer, Heidelberg-New York.

Lowestern, J.B. (1993) Evidence for a copper-bearing fluid in magma erupted at the Valley of Ten Thousand Smokes, Alaska. *Contributions to Mineralogy and Petrology,* **114,** 409-421.

-. (1994a) Chlorine, fluid imiscibility and degassing in peralkaline magmas from Pantelleria, Italy. *American Mineralogist,* **79,** 353-369.

-. (1994b) Dissolved volatile concentrations in an ore forming magma. *Geology,* **22,** 893-896.

Luhr, J.F., Carmichael, I.S.E., and Varekamp, J.C. (1984) The 1982 eruptions of El Chichon volcano, Chiapas, Mexico: Mineralogy and petrology of the anhydrite-bearing pumices. *Journal of Volcanology and Geothermal Research,* **23,** 69-108.

Mackey, J.H. (1963) EPR study of impurity-related color centers in germanium-doped quartz. *Journal of Chemical Physics,* **39,** 74-83.

MacLellan, H.E., and Trembath, T.T. (1991) The role of quartz crystallization in the development and preservation of igneous textures in granitic rocks: Experimental evidence at 1kbar. *American Mineralogist,* **76,** 1291-1305.

Mahood, G.A. (1990) Second reply to comment of R. S. Sparks, H. E. Huppert, and C. J. D. Wilson on "Evidence for long residence times of rhyolite magma in the Long Valley magmatic system: Isotopic record in precaldera lavas of Glass Mountain". *Earth and Planetary Science Letters,* **99,** 395-399.

Mainprice, D., Taki, S., and Hosaka, M. (1993) Water in hydrothermally grown sapphire (α-Al_2O_3). In J.N. Boland, and J.D. Fitz Gerald, Eds. Defects and Processes in the Solid State: Geoscience Applications, The McLarren Volume, p. 347-358. Elsvier Science Pubilshers, Amsterdam.

Marel, H.W.v.d., and Beutelspacher, H. (1976) Atlas of Infrared Spectroscopy of Clay Minerals and their Admixtures. Elsevier Science, Amsterdam.

Marsh, B.D. (1988) Crystal capture, sorting and retention in convecting magma. *Bulletin of the Geological Society of America,* **100,** 1720-1737.

-. (1990) Reply to: Discussion of "Crystal capture, sorting, and retention in a convecting magma chamber." by R. S. J. Sparks. *Bulletin of the Geological Society of America,* **102,** 849-850.

-. (1991) Reply to Comments on: "On convective style and vigor in sheet-like magma chambers." by H. E. Huppert and J. S. Turner. *Journal of Petrology,* **32,** 855-860.

Marsh, B.D., and Maxey, M.R. (1985) On the distribution and separation of crystals in a convecting magma. *Journal of Volcanology and Geothermal Research,* **24,** 95-150.

Marshall, D. (1988) Cathodoluminescence of Geologic Materials. Unwin Hyman, Boston, USA.

Martin, R.F., and Donnay, G. (1972) Water in the mantle. *American Mineralogist*, **57**, 554-570.

Marvrogenes, J.A., and Bodnar, R.J. (1994) Hydrogen movement into and out of fluid inclusions in quartz: Experimental evidence and geological implications. *Geochimica etCosmochimica Acta*, **43**, 141-148.

McBirney, A.R. (1993) Igneous Petrology. 508 p. Jones and Bartlett, Boston.

McMillan, P.F., and Hofmeister, A.M. (1988) Infrared and Raman spectroscopy. In F.C. Hawthorne, Ed. Spectroscopic Methods in Mineralogy and Geology, **18**, p. 99-150. Mineralogical Society of America, Washington D.C.

Mendelovici, E., and Sagarzazu, A. (1985) The use of RbCl disks for the infrared spectroscopy detection of hydrated and dehydrated halloysite in mixtures with kaolinite. *Clay Minerals,* **20,** 493-498.

Mendelovici, E., Yariv, S., and Villalba, R. (1979) Iron-bearing kaolinite in Venezuelan laterites. *Clay Minerals,* **14,** 323-331.

Merino, E., Harvey, C., and Murray, H.H. (1989) Aqueous-chemical control on the tetrahedral-aluminum content of quartz, halloysite, and other low-temperature silicates. *Clays and Clay Minerals,* **37**, 135-142.

Millikinen, K.L. (1994) Cathodoluminescence textures and origin of quartz silt in Oligocene mudrocks, South Texas. *Journal of Sedimentary Research,* **A64,** 567-571.

Moolick, R.T., and Durek, J.J. (1966) The Morenci District. In S.R. Titley, and C.L. Hicks, Eds. Geology of the Porphyry Copper Deposits, Southwestern North America, p. 221-231.

Moore, W.J., and Czamanske, G.K. (1973) Compositions of biotites from unaltered and altered monzonitic rocks in the Bingham mining district, Utah. *Economic Geology,* **73,** 878-890.

Müller, A., Seltman, R., and Hans-Jugren, B. (2000) Applications of cathodoluminescence to magmatic quartz in a tin granite: Case study from the Schellerhau Granite Complex, Eastern Erzgebirge, Germany. *Mineralum Deposita* 1.

Mullis, A. (1996) A free boundary model for shape-preserving dendritic growth at high undercooling. *Journal of Applied Physics,* **80,** 4129-4136.

Moore, W.J., and Czamanske, G.K. (1973) Compositions of biotites from unaltered and altered monzonitic rocks in the Bingham mining district, Utah. *Economic Geology,* **73,** 878-890.

Müller, A., Seltman, R., and Hans-Jugren, B. (2000) Applications of cathodoluminescence to magmatic quartz in a tin granite: Case study from the Schellerhau Granite Complex, Eastern Erzgebirge, Germany. *Mineralum Deposita* 1.

Mullis, A. (1996) A free boundary model for shape-preserving dendritic growth at high undercooling. *Journal of Applied Physics,* **80,** 4129-4136.

Munoz, J.L. (1984) F-OH and Cl-OH exchange in micas with application to hydrothermal ore deposits. In S.W. Bailey, Ed. Reviews In Mineralogy: Micas, **13**, p. 469-493. American Mineralogical Society.

-. (1992) Calculation of HF and HCl fugacities from biotite compositions: Revised equations. *Geological Society of America, Abstract Programs*, **24,** A221.

Munoz, J.L., and Ludington, S. (1974) Fluoride-hydroxyl exchange in biotite. *American Journal of Science,* **274,** 396-413.

Munoz, J.L., and Swenson, A. (1981) Chloride-hydroxyl exchange in biotite and estimation of relative HCl/HF activities in hydrothermal fluids. *Economic Geology,* **76**, 2212-2221.

Munoz, M., Boyce, A.J., Courjault-Rade, P., Fallick, A.E., and Tollon, F. (1997) Le filon (Zn-F) de Payrebrune (SW Massif Central, France): caracterisation geochimique des fluides au cours du Mesozoique a la borboure orientale du bassin d'Aquitaine. *Royal Academy Sciences*, **324**(Serie IIa), 889-906.

Munoz, M., Boyce, A.J., Courjault-Rade, P., Fallick, A.E., and Tollon, F.M. (1994) Multi stage fluid incursion in the Palaeozoic basement-hosted Saint-Salvy ore deposit (NW Montagne Noire, Southern France). *Applied Geochemistry*, **9**, 609-629.

Nakada, S., Bacon, C.R., and Gartner, A.E. (1994) Origin of phenocrysts and compositional diversity in pre-Mazama rhyodacite lavas, Crateer Lake, Oregon. *Journal of Petrology,* **35,** 127-162.

Nakamoto, K., Margoshes, M., and Rundle, R.E. (1955) Stretching frequencies as a function of distances in hydrogen bonds. *Journal of the American Chemical Society*, **77**, 6480-6488.

Nakashima, S., Matayosha, H., Yuko, T., Michibayashi, K., Masuda, T., Kuroki, N., Yamagishi, H., Ito, Y., and Nakamura, A. (1995) Infrared microscopy analysis of

water distribution in deformed and metamorphosed rocks. *Tectonophysics,* **245,** 263-276.

Nash, W.P. (1976) Fluorine, chlorine and OH-bearing minerals in the Skaergaard intrusion. *American Journal of Science,* **276,** 546-557.

Niimi, N., Aikawa, N., and Shinoda, K. (1999) The infrared absorption band at 3596 cm^{-1} of recrystallised quartz from Mt. Takamiyama, Southwest Japan. *Mineralogical Magazine*, **63**, 693-701.

Norton, D.L. (1982) Fluid and heat transport phenomena typical of copper-bearing pluton environments. In S.R. Titley, Ed. Advances in Geology of the Porphyry Copper Deposits, p. 59-72. Arizona Press, Arizona.

Onasch, C.M., and Vennemann, T.W. (1995) Disequilibrium partitioning of oxygen isotopes associated with sector zoning in quartz. *Geology,* **23**, 1103-1106.

O'Neil, J.R. (1986) Theoretical and Experimental Aspects of Isotopic fractionation. In J.W. Valley, H.P. Taylor Jr., and J.R. O'Neil, Eds. Stable Isotopes In High Temperature Geological Processes, Reviews in Mineralogy **16**, p. 1-37. American Mineralogical Society.

O'Neil, J.R., and Taylor Jr., H.P. (1967) The oxygen isotope and cation exchange chemistry of feldspars. *American Mineralogist*, **52,** 1414-1437.

Ortoleva, P.J. (1990) Role of attachment kinetic feedback in the oscillatory zoning of crystals grown from melts. *Earth Science Reviews*, **29,** 3-8.

Owen, M.R., and Carozzi, A.V. (1986) Southern provenance of upper Jackford Sandstone, southern Ouachita Mountains: Cathodoluminescence petrography. *Geological Society of America Bulletin,* **97,** 110-115.

Parry, W.T., Ballantine, G.H., and Wilson, J.C. (1978) Chemistry of biotite and apatite from a visicular quartz latite porphyry plug at Bingham, Utah. *Economic Geology*, **73,** 1308-1314.

Parry, W.T., and Jacobs, D.C. (1975) Fluorine and chlorine in biotite from Basin and Range plutons. *Economic Geology*, **73,** 1308-1314.

Parsons, I., Mason, R.A., Becker, S.M., and Finch, A.A. (1991) Biotite equilibria and fluid circulation in the Klokken Intrusion. *Journal of Petrology,* **32,** 1299-1333.

Paterson, M.S. (1989) The interaction of water with quartz and its influence in dislocation flow - an overview,. In S.I. Karato, and A.H. Heuer, Eds. Rheology of Solids and of the Earth, p. 107-142. Oxford University. Press, Oxford.

Patrier, P., Traineau, H., Papanagiotou, P., Turgne, E., and Beaufort, D. (1998) I-S series in geothermal fields: comparison with diagenetic I-S series. In G.B. Arehart, and J.R. Hulston, Eds. Water-Rock Interaction. Balkema, Rotterdam.

Pearce, T.H., and Kolisnik, A.M. (1990) Observations of plagioclase zoning using interference imaging. In P.J. Ortoleva, Ed. Self-Organization in Geological Systems; Proceedings of a Workshop, *Earth-Science Reviews.* **29,** p. 9-26. Elsevier, Amsterdam.

Peng, G., Luhr, J.F., and McGhee, J.J. (1997) Factors controlling the sulfur concentrations in volcanic apatite. *American Mineralogist*, **82,** 1210-1224.

Pennison-Dorland, S.C. (2001) Illumination of vein quartz textures in a porphyry copper ore deposit using scanned cathodoluminescence: Grasberg Igneous Complex, Irian Jaya, Indonesia. *American Mineralogist*, **86**, 652-666.

Peppard, B.T., Steele, I.M., Davis, A.M., Wallace, P.J., and Anderson Jr, A.T. (2001) Zoned quartz phenocrysts from the Bishop Tuff. *American Mineralogist*, **86,** 1034-1052.

Perny, B., Eberhardt, P., Ramseyer, K., Mullis, J., and Pankrath, R. (1992) Microdistribution of aluminium, lithium and sodium in a quartz: possible causes and correlation with short lived cathodoluminescence. *American Mineralogist*, **77**, 534-544.

Petit, S., and Decarreau, A. (1990) Hydrothermal (200°C) synthesis and crystal chemistry of synthetic kaolinite. *Clay Minerals*, **25,** 181-196.

Piccoli, P., and Candela, P.A. (1994) Apatite in felsic rocks: A model for the estimation of initial halogen concentrations in the Bishop Tuff (Long Valley) and Tuolumne intrusive suite (Sierra Nevada Batholith) magmas. *American Journal of Science*, **294,** 94-135.

Piccoli, P., Candela, P.A., and Williams, T.J. (1999) Estimations of initial HCl and Cl concentrations in felsic systems. *Lithos,* **46,** 591-604.

Polya, D.A., Foxford, K.A., Stuart, F., Boyce, A., and Fallick, A.E. (2000) Evolution and paragenetic context of low δD hydrothermal fluids from the Panasqueira W-Sn deposit, Portugal: new evidence from microthermometric, stable isotope, noble gas and halogen analyses of primary fluid inclusions. *Geochimica et Cosmochimica Acta*, **64**, 3357-3371.

Post, A., and Tullis, J. (1998) The rate of water penetration in experimentally deformed quartzite; Implications for hydraulic weakening,. *Tectonophysics,*, **295**, 117-137.

Prost, R., Dameme, A., Huard, E., Driard, J., and Leydecker, J.P. (1989) Infrared study of structural OH in kaolinite, dickite, nakrite and poorly crystalline kaolinite at 5 to 600K. *Clays and Clay Minerals*, **37,** 464-468.

Qin, Z., Lu, F., and Anderson, A.T.J. (1992) Diffusive re-equilibration of melt and fluid inclusions. *American Mineralogist*, **77,** 565-576.

Ramberg, H. (1952) Chemical bonds and the distribution of cations in silicates. *Journal of Geology*, **60,** 331-355.

Ramseyer, K., Baumann, J., Matter, A., and Mullis, J. (1988) Cathodoluminescence colours of α-quartz. *Mineralogical Magazine*, **52,** 669-677.

Ramseyer, K., and Mullis, J. (1990) Factors influencing short-lived blue cathodoluminescence of α-quartz. *American Mineralogist*, **75,** 791-800.

Rendon, J.L., and Serna, C.J. (1981) IR spectra of powder hematite: Effects of particle size and shape. *Clay Minerals*, **16,** 375-382.

Rendon-Angeles, J.C., Yanagisawa, K., Ishzawa, N., and Oishi, S. (2000) Conversion of calcium fluorapatite into calcium hydroxylapatite under alkaline hydrothermal conditions. *Journal of Solid State Chemistry*, **151**, 65-72.

Reyes, A.G. (1990) Petrology of the Philipine geothermal systems and the application of alteration mineralogy to their assessment. *Journal of Volcanology and Geothermal Research,* **43,** 279-309.

Rintoul, L., Panayiotou, H., Kokot, S., George, G., Cash, G., Frost, R.L., Bui, T., and Fredericks, P. (1998) Fourier transform infrared spectroscopy: A versatile technique for real world samples. *The Analyst*, **123**, 571-577.

Roedder, E. (1958) Technique for the extraction of fluid-filled inclusions from minerals. *Economic Geology*, **53**, 235-269.

Roedder, E. (1984) Fluid Inclusions. 644 p. Mineralogical Society of America Monograph, Washington D. C.

Rossman, G.R. (1988) Vibrational spectroscopy of hydrous components,. In F.C. Hawthorne, Ed. Spectroscopic Methods in Mineralogy and Geology:, Reviews in Mineralogy 18, p. 193-206,. American Mineralogical Society.

Rouxhet, P.G., Samudaheata, N., Jacobs, H., and Anton, O. (1977) Attribution of the OH stretching bands of kaolinite. *Clay Minerals*, **12,** 171-179.

Rovetta, M.R., Blacic, J.D., Hervig, R.L., and Holloway, J.R. (1989) An experimental study of hydroxyl in quartz using infrared spectroscopy and ion microprobe techniques. *Journal of Geophysical Research*, **94**, 5840-5850.

Russell, J.D. (1974) Instrumentation and Techniques. In V.C. Farmer, Ed. The Infrared Spectra of Minerals, p. 11-27. Mineralogical Society, London.

Russell, J.D., and Fraser, A.R. (1994) Infrared Methods. In M.J. Wilson, Ed. Clay Mineralogy: Spectroscopic and Chemical Determinative Methods, p. 11-68. Chapman and Hall, London.

Rutherford, M.J., and Hill, P.M. (1993) Magma ascent rates from amphibole breakdown: An experimental study applied to the 1980-1986 Mount St Helens eruption. *Journal of Geophysical Research,* **98,** 19667-19685.

Schutz, A., Stone, W.E.E., Poncelet, G., and Fripiat, J.J. (1987) Preparation and characterization of bidimensional zeolitic structures obtained using synthetic beidellite and hydroxyl-aluminum solutions. *Clays and Clay Minerals*, **35,** 251-261.

Selby, D., and Nesbitt, B.E. (2000) Chemical composition of biotite from the Casino porphyry Cu-Au-Mo mineralization, Yukon, Canada: evaluation of magmatic and hydrothermal fluid chemistry. *Chemical Geology*, **171**, 77-93.

Seyedolali, A., Krinsley, D.H., Boggs, J.S., O'Hara, P.F., Dypvik, H., and Goles, G.G. (1997) Provenence interpretation of quartz by scanning electron microscope-cathodoluminescence fabric analysis. *Geology*, **25,** 787-790.

Sha, L.K., and Chappell, B.W. (1999) Apatite chemical composition, determined by electron microprobe and laser-ablation inductively coupled plasma mass spectrometry, as a probe into granite petrogenesis. *Geochimica et Cosmochimica Acta*, **63,** 3861-3881.

Shen, X.C., Dunlop, A.C., and Cohen, D.R. (1999) Characterization of residual and transported regolith profiles using the PIMA II. International Geochemical Exploration Symposium, p. 137-138. The Association of Exploration Geochemists, Vancouver.

Sheppard, S.M.S. (1986) Characterisation and isotopic variations of natural waters. Stable Isotopes in High Temperature Geological Processes, Reviews in Mineralogy, **16**, p. 165-183. American Mineralogical Society.

Sheppard, S.M.S., and Charef, A. (1986) Eau organique: characterisation isotopique et evidence de son role dans la gisement Pb-Zn de Fedj-el-Adoum, Tunisie. *C. R. Acad. Sci. Paris,*, **302**(séries. II), 1189-1192.

Sheppard, S.M.S., Neisen, R.L., and Taylor Jr., H.P. (1971) Hydrogen and oxygen isotope ratios in porphyry copper deposits. *Economic Geology* 515-542.

Shimizu, N. (1990) The oscillatory trace element zoning of augite phenocrysts. *Earth Science Reviews,* **29,** 27-37.

Shinohara, H., Ilyama, J.T., and Matsuo, S. (1989) The partitioning of chlorine between silicate melt and hydrothermal solutions: I Partitioning of NaCl-KCl. *Geochimica et Cosmochimica Acta,* **53,** 2617-2630.

Sibley, D.F., Vogel, T.A., Walker, B.M., and Byerly, G. (1976) The origin of oscillatory zoning in plagioclase: A diffusion controlled model. *American Journal of Science,* **276,** 275-284.

Simon, K. (1997) H-isotope composition of different 'water' reservoirs in hydrothermal quartz. *Terra Abstracts*, **E.U.G. IX**.

-. (2001) Does δD from fluid inclusion in quartz reflect the original hydrothermal fluid? *Chemical Geology*, **177**, 483-495.

Sillitoe, R.H. (1973) The tops and bottoms of porphyry copper deposits. *Economic Geology,* **68**, 512-542.

Singer, B.S., Dungan, M.A., and Layne, G.D. (1995) Textures and Sr, Ba, Mg, Fe, K and Ti compositional profiles in volcanic plagioclase: clues to the dynamics of calc-alkaline magma chambers. *American Mineralogist*, **80,** 776-798.

Sippel, R.F. (1968) Sandstone petrology, evidence from luminescence petrography. *Journal of Sedimentary Petrology*, **38,** 530-554.

Sisson, V.B. (1987) Halogen chemistry as an indicator of metamorphic fluid interaction with the Ponder pluton, Coast Plutonic Complex, British Columbia, Canada. *Contributions to Mineralogy and Petrology,* **95,** 123-131.

Sisson, V.B., Lovelace, R.W., Maze, W.B., and Bergman, S.C. (1993) Direct observation of fluid inclusion formation. *Geology*, **21,** 751-754.

Smyth, J.R., Bell, D.R., and Rossman, G.R. (1991) Incorporation of hydroxyl in upper mantle clinopyroxenes. *Nature*, **351**, 732-735.

Sparks, R.S.J. (1990) Discusion of: "Crystal capture, sorting and retention in convecting magma." by B. D. Marsh. Bulletin of the Geological Society of America, 102, 847-848.

Sparks, R.S.J., Huppert, H.E., Koyaguchi, T., and Hallworth, M.A. (1993) Origin of modal and rhythmic layering by sedimantation in a convecting magma chamber. *Nature*, **361**, 246-249.

Sparks, R.S.J., Huppert, H.E., and Turner, J.S. (1984) The fluid dynamics of evolving magma chambers. *Philosphical Transactions of the Royal Society of London,* **A310,** 511-534.

Sparks, R.S.J., and Marshall, L.A. (1986) Thermal and mechanical constraints on mixing between silicic and mafic magmas. *Journal of Volcanology and Geothermal Research,* **29,** 99-124.

Sprunt, E.S. (1978) Effect of impurities on quartz cathodoluminescence. Eos, 59, 1216.

-. (1981) Causes of quartz cathodoluminescence colors. *Scanning Electron Microscopy,* **1,** 525-535.

Stevens Kalkeff, M.A.S., and Phillips, M.R. (1995) Cathodoluminescence microcharacterisation of the defect structure of quartz. *Physical Review Letters,* **52/5(B),** 3122-3134.

Stevens Kalkeff, M.A.S., Phillips, M.R., Moon, A.R., and Smallwood, A. (1997) Cathodoluminescence microanalysis of natural hydrated amorphous SiO_2: Opal. *Physics and Chemistry of Minerals,* **24,** 131-138.

Stewart, A., and Kamprad, J. (1997) Piercing the regolith veil; identifying parent rocks from weathered equivalents, Eastern Goldfields, Western Australia. *Australian Geological Survey Organisation Newsletter,* **26,** 1-6.

Streck, M.J., and Dilles, J.H. (1998) Sulfur evolution of oxidized arc magmas as recorded in apatite from a porphyry copper batholith. *Geology,* **26,** 523-526.

Suzuki, S., and Nakashima, S. (1999) In-situ IR measurements of OH species in quartz at high temperatures. *Physics and Chemistry of Minerals*, **26**, 217-225.

Swanson, S.E., and Fenn, P.M. (1986) Quartz crystallization in igneous rocks. *American Mineralogist,* **71,** 331-342.

Tacker, R.C., and Stormer, J.C.J. (1989) A thermodynamic model for apatite solid solutions, applicable to high-temperature geologic problems. *American Mineralogist,* **74,** 877-888.

Taylor, R.P. (1983) Comparison between biotite geochemistry of Bakircay, Turkey, and Los Pelambres, Chille, porphyry copper systems. *Transactions of the Institute for Mining and Metallurg,* **B 92**, B16-B22.

Terziev, G. (1966) Kostivite, a gold copper telluride from Bulgaria. *American Mineralogist,* **51,** 29-36.

-. (1971) Hemusite; a complex copper-tin-molybdenum sulfide from the Chelopech ore deposit, Bulgaria. *American Mineralogist,* **56,** 1847-1854.

Thompson, A.J.B., Hauff, P.L., and Robitaille, A.J. (1999) Alteration mapping in exploration: application of short-wave infrared (SWIR) spectroscopy. *SEG newsletter,* **39,** 16-27.

Todorov, T. (1991) NAA analysis of gold in minerals from Upper Cretaceous massive copper deposits in Bulgaria. *Terra Nova,* **3,** 311.

Torgesen, J.L., and Jackson, R.W. (1965) Growth layers on ammonium dihydrogen phosphate. *Science,* **148,** 952-954.

Valley, J.W., and Graham, C.M. (1996) Ion microprobe analysis of oxygen isotope ratios from Skye granite; healed microfractures, fluid flow, and hydrothermal exchange. *Contributions to Mineralogy and Petrology,* **124,** 225-234.

Wada, K. (1967) A study of hydroxyl groups in kaolin minerals utilising selective deuteration and infrared spectroscopy. *Clays and Clay Minerals,* **7,** 51-61.

Watt, G.R., Wright, P., Galloway, S., and McLean, C. (1997) Cathodoluminescence and trace element zoning in quartz phenocrysts and xenocrysts. *Geochimica Cosmochimica et Acta,* **61,** 4337-4348.

Wettlaufer, J.S., Jackson, M., and Elbaum, M. (1994) A geometric model for anisotropic crystal growth. *Journal of Physics A: Mathematical and General,* **27,** 5957-5967.

Williams, S.A., and Cesbron, F.P. (1977) Rutile and apatite; useful prospecting guides for porphyry copper deposits. *Mineralogical Magazine,* **41,** 288-292.

Wilkinson, J.J., Jenkin, G.R.T., Fallick, A.E., and Foster, R.P. (1995) Oxygen and hydrogen isotopic evolution of Variscan crustal fluids, south Cornwall, U. K. *Chemical Geology,* **123,** 239-254.

Winograd, I.J., Szabo, B.J., Coplen, T.B., Riggs, A.C., and Kolesar, P.T. (1985) Two million year record of deuterium depletion in groundwaters. *Science,* **227,** 519-522

Yang, K., Browne, P.R.L., Huntington, J.F., and Walshe, J.L. (2001) Characterising the hydrothermal alteration of the Broadlands-Ohaaki geothermal system, New Zealand, using short-wave infrared spectroscopy. *Journal of Volcanology and Geothermal Research,* **106,** 53-65.

Yang, K., Huntington, J.F., and Scott, K.M. (1998) Spectral characteristics of the alteration at Hishakari, Japan. In G.B. Arehart, and J.R. Hulston, Eds. Water-Rock Interaction, p. 587-590. Balkema, Rotterdam.

Yardley, B.W.D. (1984) Apatite composition and fugacities of HF and HCl in metamorphic fluids. *Mineralogical Magazine,* **49,** 77-79.

Yariv, S., and Shoval, S. (1976) Interaction between alkali-halides and halloysite: I.R. study of the interaction between alkali-halides and hydrated halloysite. *Clays and Clay Minerals,* **24,** 253-261.

Zhang, G., Pan, Y., and Chen, N. (1998) Short wave infrared (SWIR) reflectance spectroscopic study of kaolinite group minerals at the Athabasca basin. Geological Association of Canada and Mineralogical Association of Canada Abstract Volume, A-203.

Zhu, C., and Sverjensky, D.A. (1992) F-Cl-OH partitioning between biotite and apatite. *Geochimica Cosmochimica et Acta,* **56,** 3435-3468.

Zinkernagel, U. (1978) Cathodoluminescence of quartz and its application to sandstone petrology. *Contributions to Sedimentology*, **8,** 1-69.